



Chair of Polymer Processing

Master's Thesis

Experimental and numerical investigation of  
special flow phenomena in powder injection  
molding

Markus Schwaiger, BSc

September 2019

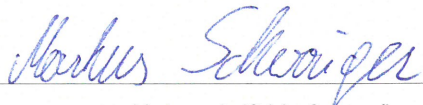
## EIDESSTATTLICHE ERKLÄRUNG

Ich erkläre an Eides statt, dass ich diese Arbeit selbständig verfasst, andere als die angegebenen Quellen und Hilfsmittel nicht benutzt, und mich auch sonst keiner unerlaubten Hilfsmittel bedient habe.

Ich erkläre, dass ich die Richtlinien des Senats der Montanuniversität Leoben zu "Gute wissenschaftliche Praxis" gelesen, verstanden und befolgt habe.

Weiters erkläre ich, dass die elektronische und gedruckte Version der eingereichten wissenschaftlichen Abschlussarbeit formal und inhaltlich identisch sind.

Datum 30.09.2019



Unterschrift Verfasser/in  
Markus, Schwaiger  
Matrikelnummer: 01435038

## **Acknowledgement**

First, I would like to thank Dipl.-Ing. Timo Gebauer (SIGMA Engineering GmbH, Germany) for the possibility to participate in a course of instructions for the Sigmasoft simulation software and the provided license for the simulations.

Especially I would like to express my gratitude to my advisor Assoc.Prof. Dipl.-Ing. Dr. mont. Thomas Lucyshyn. Whether I had questions regarding my research or needed help with my experiments, his office was always open and he supported me in every single stage. I am very thankful for his willingness to give his time so generously and for his friendly guidance.

I am also grateful to Dipl.-Ing. Dr. mont. Ivica Duretek, for his expert advice concerning the characterization of the materials and further organizational operations. Without his expertise with feedstocks, this work would not have been possible.

Special thanks also to his team, to Julia Gössmann and Sabrina Winkler, who characterized two of the three feedstocks for me.

Last but not least I want to thank my parents for their great support during my whole studies, who made this possible at all.

## **Abstract**

In this master's thesis special flow phenomena of the powder injection molding process were experimentally and numerically investigated since the physical backgrounds behind the flow behavior of the used materials (feedstocks – highly filled plastics) cannot be fully described yet. Consequently, nowadays there are still major discrepancies between the simulation of the injection molding process with feedstocks and the practical experiment.

Feedstocks exhibit a higher thermal conductivity, a higher heat transfer and a lower specific heat compared to unfilled plastics and it was hypothesized, that a certain threshold temperature exists, where the material suddenly changes from fluid to a solid behavior. Whereas the material is expected to flow in a channel at high temperatures like unfilled thermoplastics, below this threshold temperature the material will only be pushed through the channels like a solid. The material close to the wall will reach this threshold temperature very quickly and form a solid case, which will slip at the wall. With experimental filling studies with two different cavities and three different materials, the flow behavior was visualized at different mold temperatures and injection rates and the accordance with the hypothesis was analyzed.

This hypothesis was rebutted by the experiments. Although at low mold temperatures the material was pushed through the cavity as solid, no threshold temperature could be determined since there was a continuous transition of the flow behavior at higher mold temperatures. A typical fountain flow of the material could not be achieved below the melting temperature and special flow phenomena appeared. There was always a preceding material area at the melt front and the material tended to keep its shape even at changes of the cross section of the flow channel. The measured injection pressures showed a linear correlation with the mold temperature and no sudden changes due to an existing threshold temperature could be observed. The simulation of the experiments predicted much lower pressures (average deviation of 69 % to the real pressure) and showed a completely different flow behavior comparable to unfilled plastics (like polypropylene) with standard settings in the software. In fact, none of the observed flow phenomena was reproduced by the simulation, which highlights the importance of understanding the physical processes.

# Table of Contents

<b>1</b>	<b>INTRODUCTION</b> .....	<b>1</b>
<b>2</b>	<b>THEORETICAL BACKGROUND</b> .....	<b>2</b>
2.1	Powder injection molding .....	2
2.2	Feedstocks .....	3
2.3	Rheology .....	5
2.3.1	Viscosity model .....	8
2.3.2	Wall slip .....	9
2.3.3	Jetting .....	12
2.3.4	Powder-binder segregation .....	13
<b>3</b>	<b>EXPERIMENTAL</b> .....	<b>15</b>
3.1	Feedstock characterization .....	15
3.2	Experimental setup .....	17
3.2.1	Machine and measurement equipment .....	17
3.2.2	Experimental plan .....	18
3.3	Simulation .....	20
3.3.1	Modell setup .....	20
3.3.2	Material properties .....	23
<b>4</b>	<b>RESULTS</b> .....	<b>28</b>
4.1	Filling pattern .....	28
4.2	Pressure .....	35
<b>5</b>	<b>SUMMARY AND OUTLOOK</b> .....	<b>46</b>
<b>6</b>	<b>REFERENCES</b> .....	<b>48</b>
<b>7</b>	<b>LIST OF TABLES AND FIGURES</b> .....	<b>52</b>
7.1	Tables .....	52
7.2	Figures .....	52
<b>8</b>	<b>ABBREVIATIONS</b> .....	<b>58</b>
<b>9</b>	<b>APPENDIX</b> .....	<b>59</b>

# 1 Introduction

Powder injection molding is a net-shape manufacturing process for the production of complex metal or ceramic parts on a large scale. In contrast to the conventional injection molding process, highly filled plastics with ceramic or metal powder are used. Consequently, the material exhibits different rheological and thermal properties compared to unfilled plastics, which further lead to special flow phenomena. The physical background behind this cannot be fully described yet, hence the simulation of the injection molding process with such materials cannot adequately reproduce or predict the reality. Nowadays the simulation of processes is very important since there are many positive factors regarding costs and time. Therefore, an understanding of the physical process is of particular importance. Due to the high thermal conductivity, high heat transfer and the low specific heat compared to unfilled plastics, the material will cool down very fast at the colder mold wall and the following was hypothesized:

At a certain threshold temperature, the material suddenly will exhibit solid-like behavior. This will not only result in solid-phase jetting, but also in another flow behavior. Whereas the material is expected to flow in a channel at high temperatures like unfilled thermoplastics, below a certain threshold temperature the material will only be pushed through the channels like a solid. Therefore, the pressure resistance in the injection molding process will be mainly due to solid friction at the wall and not due to shearing of the material. Especially the material close to the wall will reach this threshold temperature very quickly and form a solid case which will slip at the wall. Consequently, the mold temperature will have a high influence on the flow behavior and the resulting pressure.

One goal of this master's thesis is to investigate this hypothesis. For this purpose, filling studies with two different part geometries and three different materials should be performed at different mold temperatures and injection rates to visualize occurring flow phenomena. If the hypothesis is confirmed, the threshold temperatures should be determined and approaches for an implementation in the simulation should be provided. Furthermore, additional findings about the special flow behavior should be obtained. The practical experiments should also be compared to numerical investigations with Sigmasoft, a commercial simulation software for the injection molding process. Therefore, the materials need to be characterized regarding the rheological and thermodynamical behavior. Especially the injection pressure and the filling behavior should be investigated as they generally lead to discrepancies between simulation and experiment.

## 2 Theoretical background

### 2.1 Powder injection molding

Powder Injection Molding (PIM) is a net-shape manufacturing process which combines powder metallurgy with plastic injection molding. In contrast to the conventional injection molding process, the used materials are feedstocks instead of plastics, which exhibit different material properties. These feedstocks consist of a polymer binder and a fine metal or ceramic powder (particle size usually between  $0.1 \mu\text{m}$  and  $20 \mu\text{m}$ ). Depending on which kind of powder is used, the process is also known as metal injection molding (MIM) or ceramic injection molding (CIM). The technique consists of four main steps to receive the final product (Figure 1). These are the fabrication of the feedstock, the injection molding process where the "green part" is formed, the removal of the binder and at the end, the sintering of the debinded part [16].

This master's thesis focuses mainly on the injection molding phase, which is a critical step for forming the desired shape [3]. Defects in this phase, which might be invisible in the green part, cannot be corrected in further steps and are even amplified in the following phases. For example, such defects can be voids, jetting, phase segregation, weld lines or dead zones [23]. There are three different types of the debinding process: thermal, catalytic and solvent, which depends on the used binder system. The debinding process results in a so-called "brown part" for MIM or "white part" for CIM. Sintering, which creates a bond between the particles to get the desired mechanical properties, takes place at high temperatures. This temperature depends on the used powder and is in the range of  $1200 \text{ }^\circ\text{C}$  –  $2000 \text{ }^\circ\text{C}$ . Due to the sintering process, a high volumetric shrinkage of 12 % to 18 % occurs [16]. The final product exhibits low porosity and the achieved densities lie between 97 % and 99 % of the theoretical value [33]. The advantages of PIM are low production costs, the possibility of complex shapes, tight tolerances, applicability to several materials and high final part quality [16].

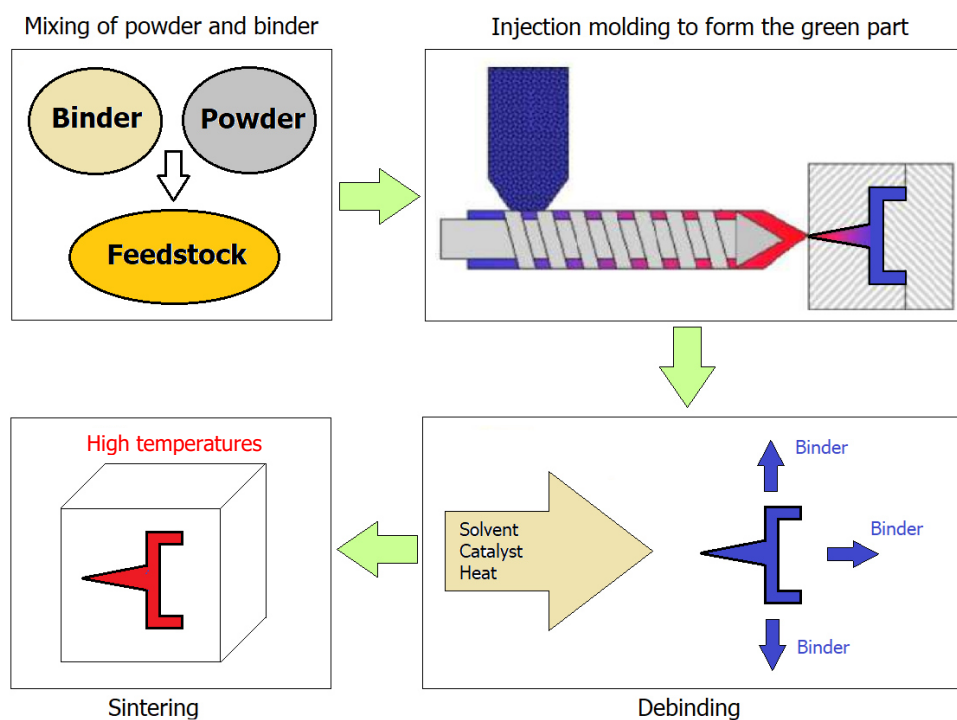


Figure 1: Schematic principle of the PIM process (according to [17]).

The main sectors for the usage of the MIM technology are user electronics (smartphones) in China, defense and automotive industry in Europe and the medical and firearms industry in America. In 2017 the global MIM sales were estimated to be around \$2.4 billion. The annual growth rates are approximately 18 % since 2010 [48].

## 2.2 Feedstocks

The feedstocks which come in a granulated form are highly filled materials. Due to the high amount of powder, feedstocks exhibit different material properties. The thermal conductivity increases by about one order of magnitude and the heat capacity decreases by a factor of three [45]. Consequently, the feedstock cools and solidifies quickly after the injection step [39, 45]. As a result, the process is very temperature sensitive and the control of the wall and injection temperature is more important than in conventional injection molding [5].

Five factors sum up to the characteristics of feedstocks: powder properties, binder composition, powder-binder ratio, mixing method and the pelletizing method. Especially the balance between powder and binder determines if the process can be performed properly. In order to ensure an appropriate viscosity and to avoid air traps, sufficient binder is needed. On the other hand, there must be enough powder to preserve the sintering ability [16]. However, a homogeneous distribution of the powder is also very important. An inhomogeneous feedstock will lead to an anisotropic shrinkage and increase the appearance of phase segregation [17]. The solids loading  $\Phi$  is specified as the volumetric ratio of solid powder to the total volume of powder and binder as shown in Eq. ( 1 ) [16]:

$$\Phi = \frac{\frac{W_P}{\rho_P}}{\frac{W_P}{\rho_P} + \frac{W_B}{\rho_B}} = \frac{\frac{W_P}{\rho_P}}{\frac{W_M}{\rho_M}} \quad ( 1 )$$

$\Phi$  .....Solids loading (-)

$W_P, W_B, W_M$ ....Weight fractions of powder, binder and mixture (feedstock) (g)

$\rho_P, \rho_B, \rho_M$ .....Density of powder, binder and mixture (feedstock) (g/cm<sup>3</sup>)

With the calculated solids loading the mixture density of the feedstock can be calculated through Eq. ( 2 ):

$$\rho_M = \Phi \cdot \rho_P + (1 - \Phi) \cdot \rho_B \quad ( 2 )$$

The powder content can vary from 45 vol.% to almost 75 vol.%. Common values are 58 vol.% to 62 vol.% for iron and steel powders and 50 vol.% to 55 vol.% for ceramic powders. At a certain point which depends on the powder and the binder, a critical solids loading  $\Phi_c$  is reached. There the powder particles are tightly packed, and all voids are filled with binder. This leads to an enormous increase of the viscosity to theoretical infinity and can be illustrated by measuring the mixing torque using a torque rheometer to receive a curve as shown in Figure 2. Consequently, the optimal solids loading is below that value to allow the processing. The curve is described through Eq. ( 3 ). The coefficient A depends on the particle size and is often around one. The exponent n is generally close to two [16].



## 2 Theoretical background

Some papers ([24, 31]) refer to Krieger, who assumes  $A=1$  and  $n=1.82$ . Philips et al. [31], who proposed a constitutive equation for concentrated suspensions that accounts for shear-induced particle migration, assumed that the critical solids loading is 68 % in all computations. This value is also used in Figure 2. It is important, that there is never a uniform powder size, but always a distribution. Furthermore, the powder can also exhibit a bimodal or polymodal distribution. Consequently, the theoretical maximum powder arrangement and thus the critical solids loading shift to higher values [38].

Since this master's thesis is focused on flow phenomena, there will be a particular look on the rheological properties in the next chapter (2.3 "Rheology"). Nevertheless, a successful injection molding process depends not only on the viscosity of the feedstock, but also on the used process conditions and the design of the mold [2].

$$\frac{\eta_M}{\eta_B} = \frac{A}{\left(1 - \frac{\Phi}{\Phi_C}\right)^n} \quad (3)$$

$\eta_M, \eta_B$ .....Viscosity of mixture (feedstock) and binder ( $\text{Pa} \cdot \text{s}$ )

$A, n$ .... ..Coefficients (-)

$\Phi_C$ .....Critical solids loading (-)

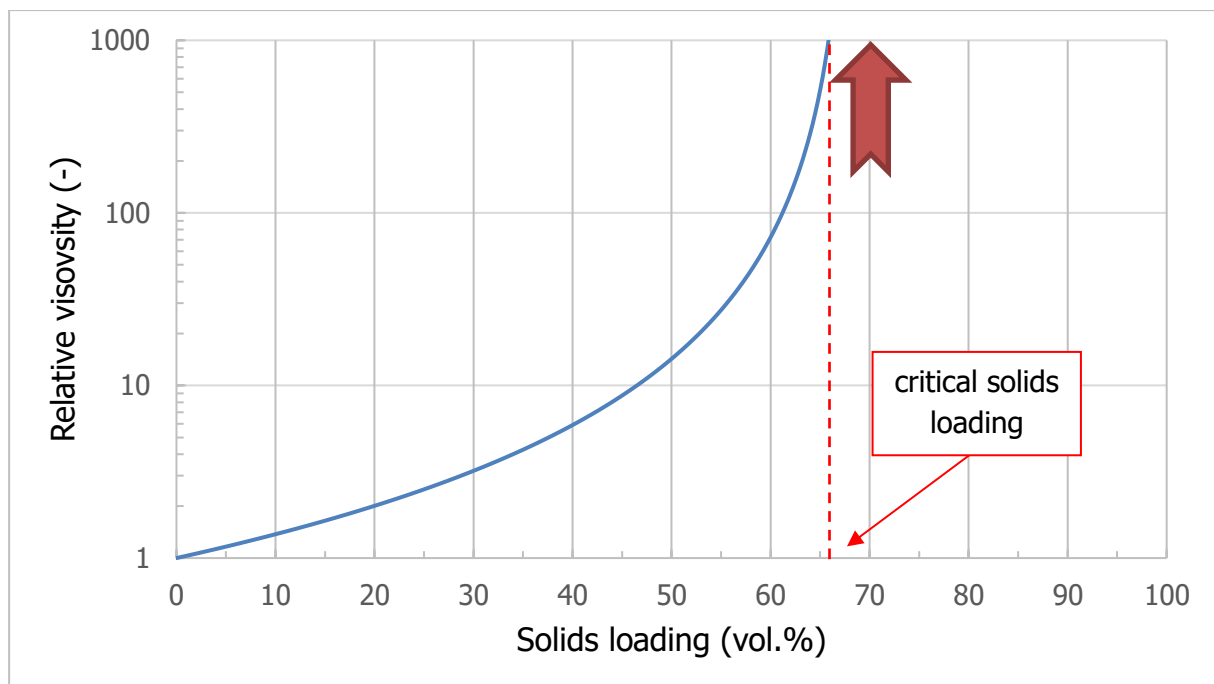


Figure 2: Relative viscosity  $\eta_M/\eta_B$  in dependence of the solids loading (according to [16]).

As already mentioned, also the powder and binder characteristics affect the feedstock properties. The powder particle shape, size and size distribution can have a strong effect on the rheological behavior and different processes (mixing, binder wetting, molding, debinding, sintering). Often the necessary characteristics stand in conflict with some desired properties. As an example, on the one hand irregular particles reduce the distortion in debinding and increase the green part strength. On the other hand, spherical particles are desired because

they have a higher packing density which leads to less dimensional change in sintering and better component strength. Easier molding due to a lower viscosity is also favored by spheres. Generally, to reduce defects during processing, an agglomeration free spherical powder ( $D < 20 \mu\text{m}$ ) is suggested. An increasing particle size would improve the sintering but also increase the interparticle friction and the appearance of flow and packing difficulties [16].

The purpose of the binder is to wet the powder and provide low viscosity for the realization of injection molding. After the powder is packed into its shape, the binder facilitates to keep this shape. Besides mainly used thermoplastic binders, also thermosetting, water-based, gelation or inorganic systems can be used. Usually the binder consists of three components. The first component is the backbone polymer which provides strength and supports the shape until the beginning of sintering. This can be polyethylene (PE), polypropylene (PP), polystyrene (PS), ethylene vinyl acetate (EVA), polyethylene glycol (PEG), polymethyl methacrylate (PMMA) or polyoxymethylene (POM). The second component is a filler phase (commonly a wax), which can be easily removed in early debinding stages. The third component is a surfactant, which acts as a bridge between powder and binder [16, 17].

Clark showed for feedstocks with spherical metal particles and different polybutene binders, that the relative viscosity of the suspensions is indirect proportional to the powder radius. Furthermore, he showed that a higher binder viscosity results in a lower powder concentration effect on the relative viscosity and that particles of higher density increased the relative viscosity faster [1].

### 2.3 Rheology

The viscosity of Newtonian fluids (e.g. water) is independent of the shear rate. Unfilled polymers show a Newtonian plateau at low shear rates, where the viscosity remains constant. This constant viscosity is also known as zero viscosity  $\eta_0$ . At a certain point shear thinning occurs, which means that the viscosity decreases with increasing shear rate. The physical process behind shear thinning is, that the corresponding increasing shear stress is high enough to disentangle the macromolecule chains. Thus, this disentangling allows an easier slide of the macromolecules past each other and therefore facilitates the flowability [37].

Figure 3 compares the viscosity curves of unfilled and highly filled thermoplastics. As already seen in the previous chapter, the viscosity increases with higher powder concentration. Highly filled feedstocks exhibit a limiting shear stress (yield stress) at low shear rates, thus there is no Newtonian plateau anymore and shear thinning even occurs at very low shear rates. This means that the viscosity increases enormously at low shear rates. The effect of the limiting shear stress is further shown in the comparison of the flow curves in Figure 4. There must be enough shear stress, that the material can flow. Complex interactions of the feedstock ingredients lead to such a flow behavior. At higher shear rates the effect of the powder decreases and therefore the matrix impact dominates [15, 27, 38].

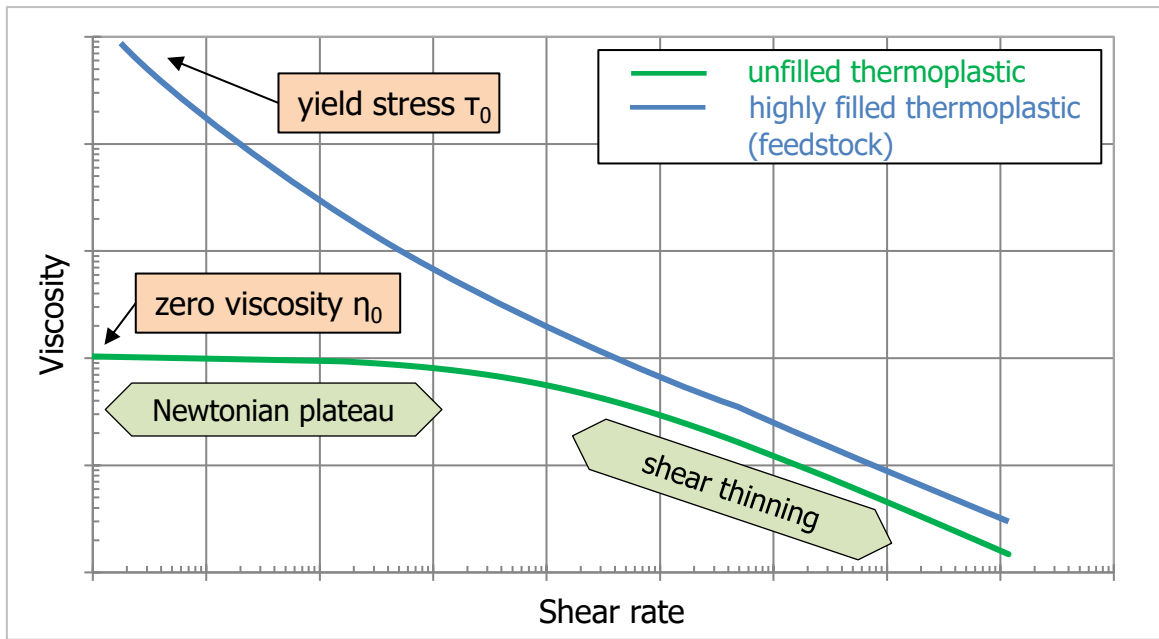


Figure 3: Schematic correlation of shear rate and viscosity of unfilled thermoplastics (green) and feedstocks (blue) (according to [12]).

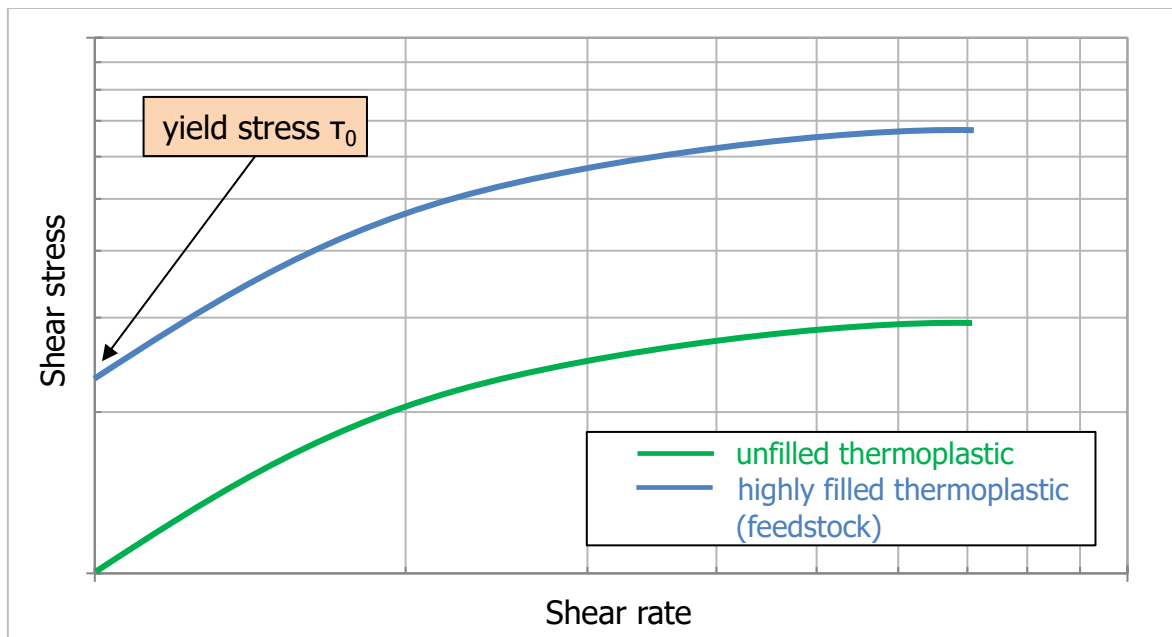


Figure 4: Schematic correlation of shear rate and shear stress of unfilled thermoplastics (green) and feedstocks (blue) (according to [37]).

It must be pointed out, that a frozen layer is formed when the melt touches the colder mold wall. Therefore, the melt has to flow through a partially frozen channel as shown in Figure 5. This phenomenon is well known as fountain flow. Heat will be further conducted through the walls, which will increase the thickness of this frozen layer till the channel is completely closed. This effect is also related to the moldability [16].

The viscosity difference of unfilled thermoplastics and feedstocks lead also to a different flow profile (Figure 6). In Figure 6 the velocity and shear profiles are sketched with consideration

of the formation of a frozen layer at the wall. Due to this consideration, directly at the wall, where the feedstock is already solidified, the shear rate is zero. In the middle of the flow channel are low shear rates which further lead to a significant increase of the viscosity for feedstocks due to the limiting shear stress. The polymer melt in this low sheared area behaves more like a solid material than a macromolecular thermoplastic. Thus, the velocity profile of feedstocks is flatter compared to unfilled thermoplastics. This characteristic profile is well known as plug flow. Adjacent to the wall of the mold the whole shear load is concentrated on a very small layer and jetting phenomena appear (see chapter 2.3.3 "Jetting"), which are typical for feedstocks [45].

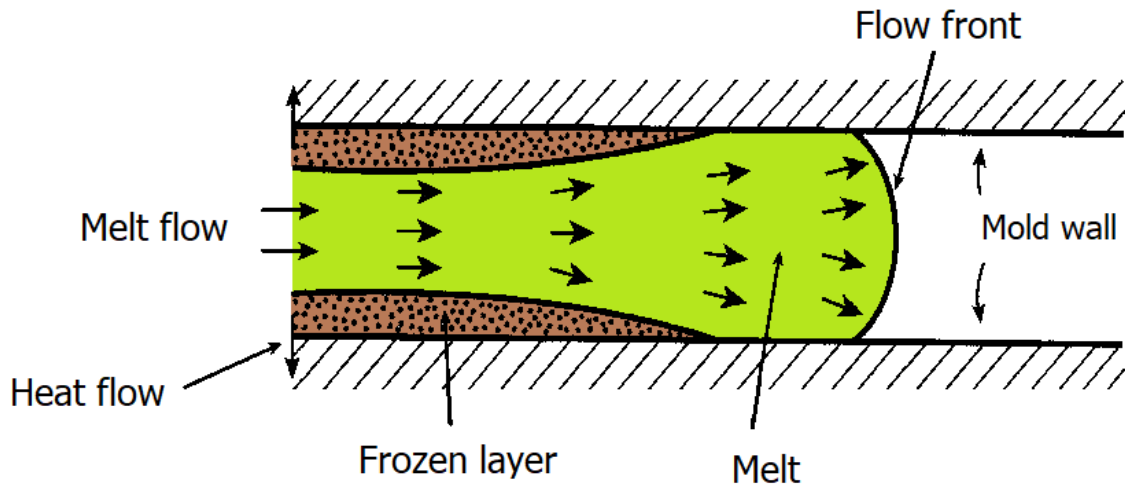


Figure 5: Flow along the cavity with the formation of a frozen layer along the wall (according to [16]).

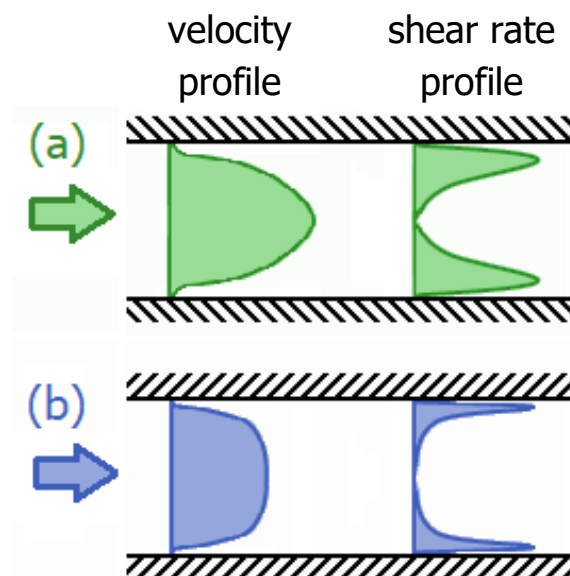


Figure 6: Comparison of the different flow profiles of (a) unfilled thermoplastics and (b) feedstocks (according to [45]).

### 2.3.1 Viscosity model

#### Cross-WLF (Cross Williams-Landel-Ferry)

In injection molding simulation software, the Cross-WLF (Cross Williams-Landel-Ferry) model is the most used model for describing the viscosity behavior. This model offers the best fit for many viscosity measurements. It considers effects of shear rate and temperature, can account for the pressure dependence and can describe the Newtonian and the shear thinning behavior [37]. Sigma Engineering GmbH (Germany) recommend this model for a detailed packing simulation. In the Sigmasoft simulation software the model is implemented as following (Eq. ( 4 ) and Eq. ( 5 )) [42]:

$$\eta(T, \dot{\gamma}, p) = \frac{\eta_0}{1 + \left(\frac{\eta_0 \dot{\gamma}}{D_4}\right)^{1-n}} \quad (4)$$

$$\eta_0(T, p) = D_1 \cdot \exp\left(\frac{-A_1 \cdot (T - D_2 - D_3 \cdot p)}{A_2 + T - D_2}\right) \quad (5)$$

$\eta, \eta_0$ ... Viscosity, zero viscosity (MPa)

$\dot{\gamma}$ ..... Shear rate ( $s^{-1}$ )

$n$ ..... Flow exponent (-)

$A_1$  ..... Factor describing the temperature dependency (-)

$A_2$  ..... Factor describing the temperature dependency (K)

$D_1$ ..... Viscosity at a reference temperature (Pa · s)

$D_2$ ..... Reference temperature ( $^{\circ}C$ )

$D_3$ ..... Factor describing the pressure dependency (K/bar)

$D_4$ ..... Transition shear stress (Pa)

#### Cross-WLF with Herschel-Bulkley extension

Nevertheless, the Cross-WLF model cannot describe the increasing viscosity at low shear rates, which occur for feedstocks. The model can only describe a shear thinning region with a Newtonian plateau (green curves in Figure 3 and Figure 4 on page 6) and is not able to reproduce a viscosity curve of a feedstock (blue curves in Figure 3 and Figure 4 on page 6). Generally, the rheological behavior of materials, that exhibit a limiting shear stress can be represented by the Herschel-Bulkley equation ( 6 ) or the Bingham equation with  $n=1$ . In contrast to the Herschel-Bulkley equation, the Bingham equation describes a Newtonian flow above this critical yield stress, thus there is no shear thinning behavior [37].

$$\tau = \tau_0 + m \cdot \dot{\gamma}^n \quad (6)$$

$\tau, \tau_0$  ... Shear stress, yield stress (MPa)

$m$ ..... Consistency index (Pa·s<sup>n</sup>)

Therefore, by adding the Herschel-Bulkley extension to the Cross-WLF model, the limiting shear stress can also be considered. According to M. Thornagel [45] the Cross-WLF with Herschel-Bulkley extension is the most promising model to describe metal feedstocks in simulation software. Sigmasoft implemented the extended model as following (Eq. ( 7 )) [42]:

$$\eta(T, \dot{\gamma}, p) = \frac{\eta_0}{1 + \left(\frac{\eta_0 \cdot \dot{\gamma}}{D_4}\right)^{1-n}} + \tau_y \cdot \frac{(1 - e^{(-\alpha \dot{\gamma})})}{\dot{\gamma}} \quad (7)$$

$\tau_y$  ..... specifies the slope point of the viscosity increase at low shear rates (100 Pa)

$\alpha$  ..... specifies the gradient of the viscosity increase at low shear rates (s)

### 2.3.2 Wall slip

#### “True slip” in general polymer melts

It must be pointed out, that the slip mechanism of unfilled polymer melts differs from the slipping phenomenon in suspensions. In unfilled polymers the wall shear stress gets higher than a critical value and a velocity discontinuity between polymer and wall occurs. This is further mentioned as “true slip” [18, 28].

There are two physical mechanisms for this “true slip”: First, the desorption of a few anchored macromolecules at the solid surface due to an adhesive failure, the flow-induced chain desorption. Second, the disentanglement of macromolecules in the bulk from macromolecules adsorbed to the wall, namely chain disentanglement [8, 11, 18]. These two mechanisms are schematically shown in Figure 7.

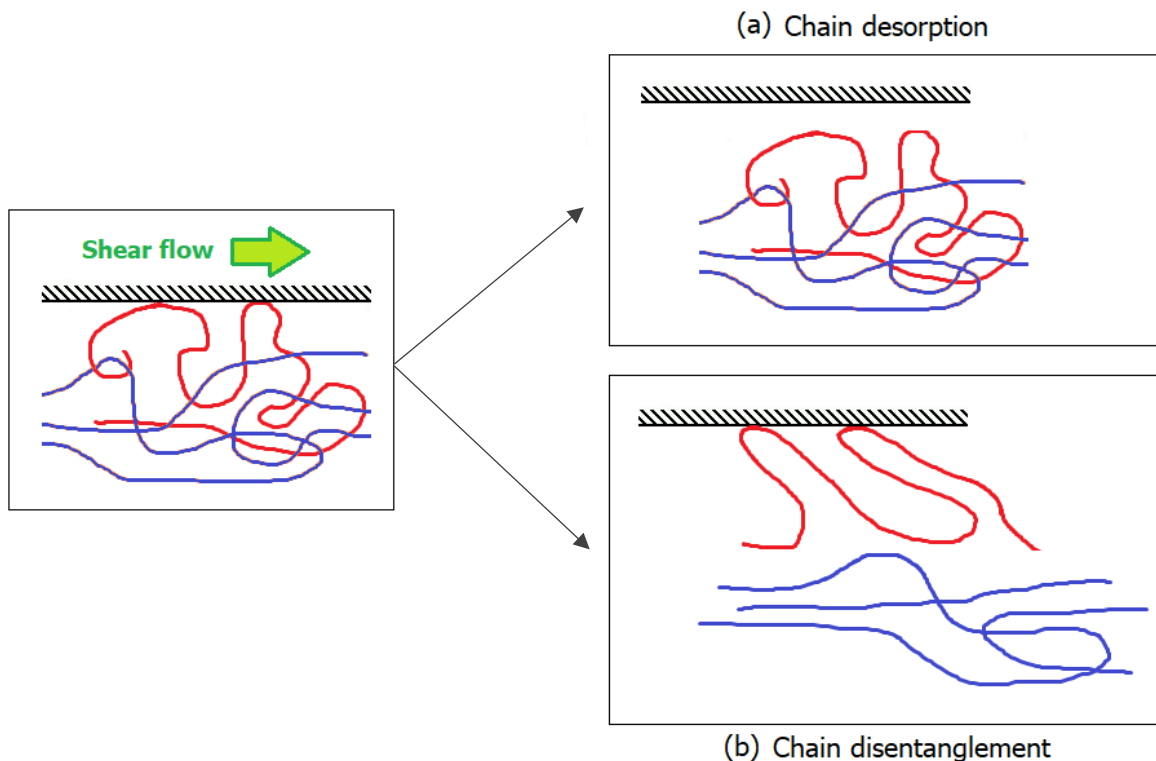


Figure 7: Schematic of the two principal mechanisms for slip, where the macromolecule (red line) in (a) desorbs from the wall or in (b) disentangles from the macromolecule in the bulk (according to [8]).

### Apparent slip in suspensions

According to Kaylon [21] and Rueda et al. [38], Bingham [7] determined lack of adhesion between the suspension and the shearing surface as the reason for occurring slip, which results in a layer of liquid between the main body of the suspension and the shearing surface. They and He et al. [19] further mentioned the formation of a relatively thin, but always present, layer of fluid adjacent to the wall described by Vand [46]. It is more efficient for the particles to shift away from a wall than physically occupy the space adjacent to the wall. This resulting layer is known as “apparent slip layer” or “Vand layer”, which consists solely of the binder and is free of powder [19, 22]. Thus, the viscosity of the apparent slip layer is much lower compared to the main body of the suspension. The thickness  $\delta$  of this layer is significantly smaller than the channel gap. Therefore and due to the lower viscosity, there is a much higher velocity gradient within this thin slip layer, which gives the appearance of wall slip between suspension and the wall [21, 22, 28]. As reported by Kaylon for Newtonian binders the slip layer thickness correlates with the particle diameter of low aspect ratio particles (Eq. ( 8 ) according to [21]). Soltani et al. [43] determined values of the ratio  $\delta/D_p$  from 0.04 (for glass) to 0.07 (for aluminum). As a summary of different publications, the thin layer was measured to be in the magnitude order of a few micrometers (between 0.7  $\mu\text{m}$  and 30  $\mu\text{m}$ ) [21, 43, 52].

$$\frac{\delta}{D_p} = 1 - \frac{\Phi}{\Phi_c} \quad ( 8 )$$

$\delta$ ..... Thickness of the apparent slip layer ( $\mu\text{m}$ )

$D_p$ ..... Harmonic mean particle diameter ( $\mu\text{m}$ )

In Figure 8 the schematic representation of the apparent slip flow in capillary dies is shown. Kaylon [21] further claimed that the apparent slip layer mechanism can be used to calculate the slip velocity  $U_s$  and provided some equations (Eq. ( 9 ) for pressure driven capillary flow under the assumption of fully developed and isothermal flow conditions in the apparent slip layer). The existence of apparent wall slip has some important consequences. Not only for the rheological characterization of highly filled feedstocks but also in the manufacturing process and the process control. Wall slipping reduces the pressure drop in die flows or reduces the capability for a good distributive and dispersive mixing in extruders due to a reduced pressurization rate [21].

$$U_s = \beta \cdot \tau_w^{\frac{1}{n_b}} \quad ( 9 )$$

$U_s$ ..... Slip velocity (mm/s)

$\beta$ ..... Navier slip coefficient ( $\text{mm} \cdot \text{Pa}^{-(1/n)} \cdot \text{s}^{-1}$ )

$\tau_w$ ..... Wall shear stress (MPa)

$n_b$  ..... Power law index of the binder (-)

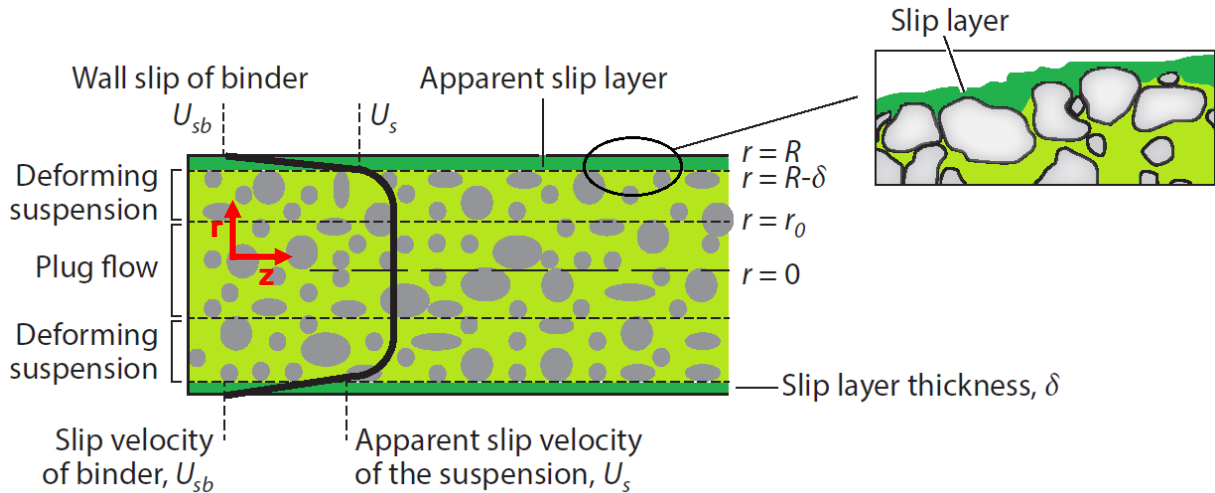


Figure 8: Schematic representation of the apparent slip flow in capillary (or rectangular) dies (according to [22]).

Kaylon assumed a no-slip condition for the pure binder zone, but for non-Newtonian binders that small layer can also exhibit “true slip” and therefore must be considered (see  $U_{sb}$  in Figure 8) [21]. For  $U_{sb}$  a hyperbolic tangent-type dependence of the wall shear stress has been found for capillary and slit flow data. This obtained correlation includes a polymer slip coefficient  $\beta_B$ , which varies inversely with the pressure [22]. For a better visualization of the different slip phenomena, the schematic velocity profiles of Newtonian fluids for simple shearing are shown in Figure 9.

Further, the effect of the shear thinning behavior on the wall slip was underlined by Kraus et al. [25] which will be further discussed in the next chapter 2.3.3 “Jetting”.

A plug flow without being deformed was observed in a steady torsional flow of a highly filled suspension of spherical particles in a Newtonian binder. In the experiment wall slip occurred on both sides and there was no deformation of the suspension, due to the experiment conditions ( $\tau_{zy} < \tau_0$ ). Therefore, wall slip and plug flow occurred at the same time. Hence, wall slip and plug flow formation behavior of the suspension need to be characterized to fully understand the flow and deformation behavior [22].

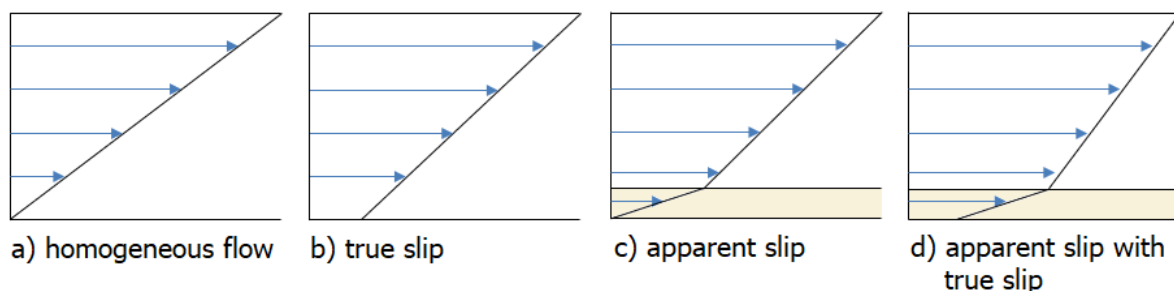


Figure 9: Schematic velocity profile of Newtonian fluids for simple shearing, where the bottom plane is fixed and the upper plane is moving.



### 2.3.3 Jetting

The mold filling process normally forms a uniform flow front. The phenomenon of forming a stream that is maintaining the geometry of the gate or the previous channel when it enters a changed (larger) geometry is known as jetting. This changed geometry is mainly the bigger cavity in comparison to the gate but can also be a sharp angle in the channel or cavity. Thus, jetting means that the melt loses its contact to the wall and therefore does not adhere to the wall anymore. Regarding the mold filling process in PIM, two types of jetting were identified, conventional (liquid-phase) jetting and solid-phase jetting (Figure 10). Conventional jetting is assigned to the loss of contact between melt and wall, especially after leaving the gate due to a too high injection rate. The stream moves to the front (cavity) wall and results in a backward filling. This leads to an inverse filling sequence because the cavity close to the mold gate is filled last. At solid-phase jetting the melt temperature is so low, that the melt partially solidifies before it enters the cavity or the changed geometry. Instead of backward filling the stiffened stream piles up upon itself. Jetting is a completely unwanted phenomenon because it creates defects like weld lines and voids [32].

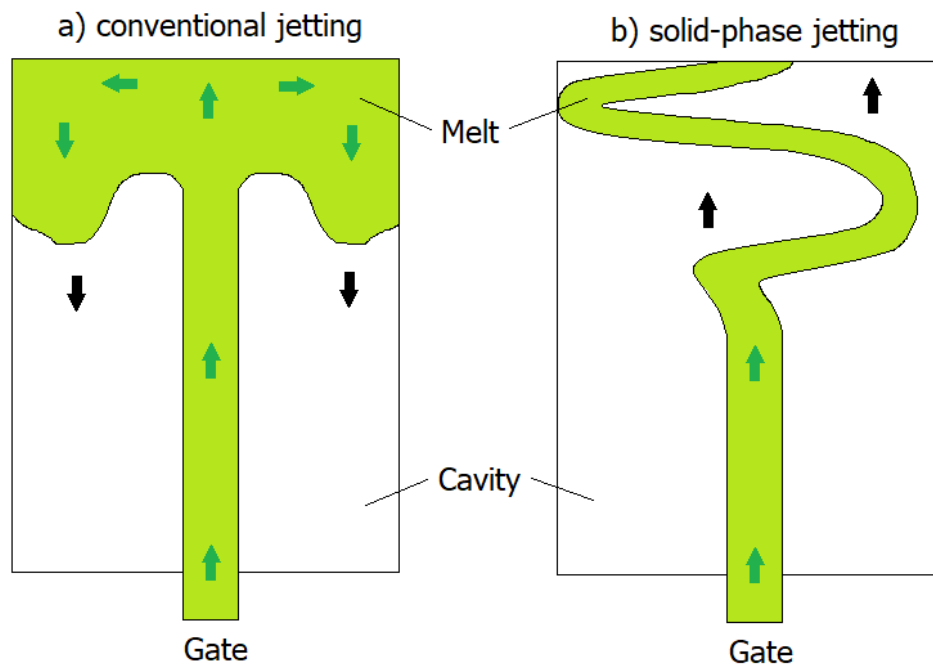


Figure 10: Schematic sketch of the two types of jetting: a) conventional jetting and b) solid-phase jetting.

Piccirillo and Lee [32] studied this phenomenon by visualization of the flow. They investigated the influence of the melt temperature, die temperature, injection rate and a cavity to gate thickness. They concluded, that there is a higher probability of conventional jetting when the cavity is thicker than the gate and at higher injection rates. Solid-phase jetting was only dependent of a threshold melt temperature, which could be approximated with an empirical equation in dependence of the shear thinning exponent  $n$  (see Eq. (4)). When this exponent  $n$  equals zero ( $n=0$ ), the no-slip condition at the wall is invalid and the material flows as a solid. Therefore solid-phase jetting results from wall slip. Krauss et al. [25] indicated that the exponent  $n$  decreases at higher solid loading.

Similar investigations and investigations focusing on runner length were performed by Dvorak et al. [13, 14] and confirmed these findings. In addition to the injection rate, Krug et al. [26] referred occurring jetting to the low die swell, which is shown by highly filled polymers. They examined jetting in a cavity with variable thickness. For the lowest thickness jetting could be avoided by adjusting the nozzle and sprue diameter and by changing the angle of impingement of the melt on the opposite face of the cavity. Sardarian et al. [40] did some numerical simulations and experimental investigations in low pressure injection molding (LPIM). Again, conventional jetting was noticed at higher injection rates and pressures. The simulation results indicated that increasing injection temperature and pressure induce an increase of the jetting length.

Hubmann [20] also observed a phenomenon related to jetting in his study as schematically drawn in Figure 11. However, he was not able to reproduce this phenomenon with the used simulation software (Autodesk Moldflow Insight 2018 (AMI) by Autodesk Inc., USA) with consideration of wall slipping.

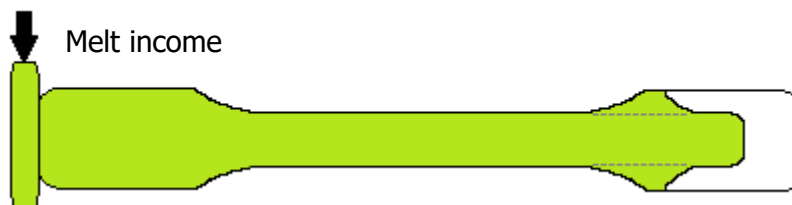


Figure 11: Schematically drawn jetting phenomenon observed by Hubmann [20].

### 2.3.4 Powder-binder segregation

Many publications summarized [30, 41, 44, 49] that powder-binder segregation or particle/powder migration, which lead to an inhomogeneously distributed powder in the green part after injection molding, result in various defects. These defects include inhomogeneous extracting of the binder, collapsing of the green body during debinding, cracks and deformation during sintering and irregular densification. As a consequence, these defects result in final products with geometrical errors as well as poor and anisotropic mechanical and physical properties.

It is commonly assumed that shearing or in particular the shearing gradient leads to the powder-binder segregation phenomenon [22, 30, 38, 44]. Visible "black lines" on the surface of the green part are a strong evidence for powder-binder segregation [44]. As Dbouk et al. [9] summarized, many investigations have been performed on suspensions to describe the shear-induced particle migration in different testing settings (concentric couette cell, cone-plate, two parallel-disks, channels, etc.). Further, the powder-binder segregation will be reduced by wall slip [4].

Thornagel [44] explained and visualized the physical effect of powder segregation due to shear rate gradients (Figure 12). There is a uniform force on the powder particles in the center, due to no or a low shear rate gradient. Therefore, these particles are not changing their flow direction. However, as already outlined previously (in 2.3 "Rheology"), there is a maximum shear gradient close to the wall. Particles in an area with higher shear rate gradients experience an uneven stress field, thus they start to rotate. This rotation increases with a bigger shear rate gradient and leads to a change in the flow direction. In other words, powder-separation

occurs because particles try to leave areas with high shear gradients. Consequently, these areas exhibit high binder contents. However, as shown in Figure 12 on the right side, the melt flow is able to transport the separation pattern and the location of cause and the location of effect can be different [44].

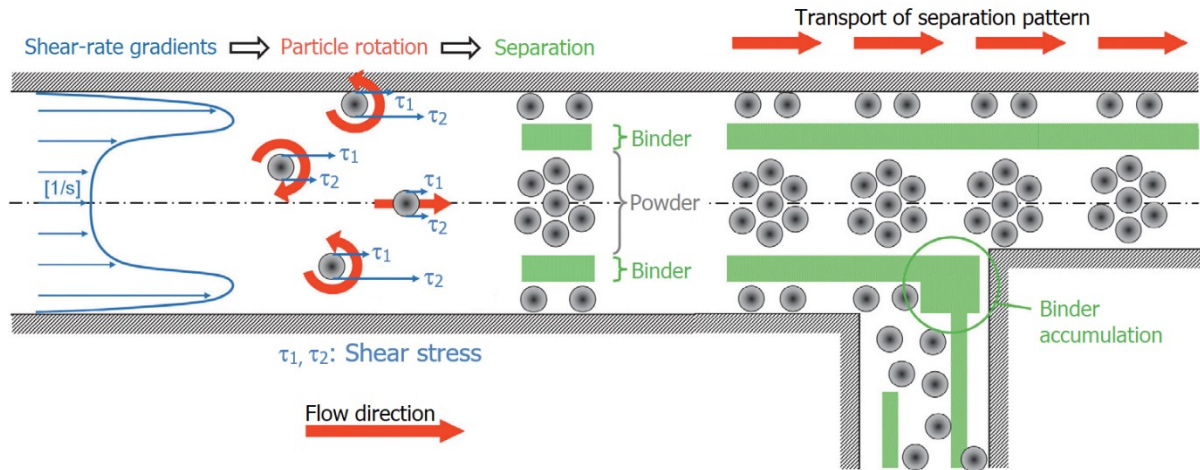


Figure 12: Powder-binder separation due to shear rate gradients and transport of the occurring separation pattern [44].

Segregation of powder and binder can be measured by various methods. Demers et al. [10] showed, that the effects can be measured by thermogravimetric analysis (TGA), pycnometer density (PD) and differential scanning calorimetry (DSC). The TGA and PD technique exhibit a measure sensitivity of at least  $\pm 0.5$  vol.%. Additionally, the results of them are independent of the feedstock formulation. Yang et al. [49] further listed optical microscopy and scanning electron microscope (SEM) with the limitation, that they only provide surface information, as well as hardness tests. Last they noted, that X-ray computed tomography (CT) has been used to analyze the separation by some researchers. Weber et al. [47] showed, that synchrotron-based microtomography (S- $\mu$ CT) combined with 3D image analysis can be used to successfully analyze powder-binder separation effects. Yang et al. [49], who based their work on previous studies ([50, 51]), generally concluded multiscale CT as a successful analysis method. Further, they assumed for analyzation of the powder-binder separation, that statistical analysis of the gray value distribution is a more general method, compared to image segmentation.

Under the assumptions of a continuous medium and a laminar, incompressible flow with no external forces, a conservation equation for the particle volume fraction with a term for the particle migration flux (often noted as  $j$ ) has been constructed [9]. Many different assumptions and considerations for this particle migration flux are provided by literature as Dbouk et al. [9] hinted in their publication. One of these is, for example, the model of Philips et al. [31], which was already mentioned earlier in chapter 2.2. This model includes a flux caused by gradients in the volume fraction and another caused by gradients in the viscosity. However, it was also remarked, that always assuming migration down a gradient in the shear rate might be incorrect. Another model is the suspension balance model (SBM), which is also used by commercially available injection molding simulation software like Moldex3D (by CoreTech System Co., Ltd) and Autodesk Moldflow Insight (by Autodesk Inc.) [6, 29]. The particle migration flux in SBM is caused by variations of the shear rate and the concentration of particles [6, 9].

### 3 Experimental

Piccirillo and Lee [32] already described the phenomenon of solid-phase jetting which is mainly a function of the melt temperature (see 2.3.3 "Jetting"). Based on similar thoughts the described assumptions in chapter 1 "Introduction" were hypothesized and analyzed within this master thesis. Therefore, occurring flow phenomena of PIM feedstocks in an injection molding process were visualized with practical experiments. Three different commercially available feedstocks were used to perform filling studies with two different part geometries at different mold temperatures and different injection rates. Furthermore, numerical investigations about these flow phenomena were performed with a simulation of the injection molding process. This was done by the simulation software Sigmasoft. For that purpose, the feedstocks had to be characterized.

#### 3.1 Feedstock characterization

Three different commercially available feedstocks from PolyMIM GmbH (Germany) were used. Two of them have the same POM based binder system but consist of a different powder. The third feedstock consists of a water-soluble binder system and another powder. The typical composition of the powder (as sintered in wt.%) is given by the material data sheet [34 - 36] and summed up in Table 1. For the simulation some physical and thermodynamic properties of the feedstocks had to be characterized. These methods are listed and described below. Necessary results for the simulation are shown in chapter 3.3.2 "Material properties" and some further information is added in the appendix (page 59 - 90). The exact names of the used feedstocks are:

- PolyPOM FN0805 B 342
- PolyPOM 316L D 170
- PolyMIM 17-4PH D 120E

Table 1: Typical composition of the powders as sintered in wt.% [34 - 36].

PolyPOM FN0805	Fe	C	Ni	other					
	Balanced	0.4 - 0.7	6.5 - 8.5	< 1					
PolyPOM 316L	Fe	C	Cr	Ni	Mo	Mn	Si	P	S
	Balanced	< 0.03	16 - 18	10 - 14	< 2	< 2	< 1	< 0.045	< 0.03
PolyMIM 17-4PH	Fe	C	Cr	Ni	Mn	Si	Cu	other	
	Balanced	< 0.07	15 - 17.5	3 - 5	< 1	< 1	3 - 5	< 0.45	

### Specific heat

The specific heat  $c_p$  was measured on a differential scanning calorimetry (DSC)-measuring device (Type DSC1 by Mettler Toledo GmbH, USA) according to ISO 11357-4. The measuring was performed under inert gas atmosphere ( $N_2$ ) with a linear heating rate of 10 K/min and a linear cooling rate of 20 K/min. Due to the high weight percentage of powder in the feedstock, more mass than the usual 10 mg has been used. The measurements were performed two times for the PolyPOM FN0805 and for the other two materials three times. The used masses for the analysis were:

- PolyPOM FN0805: 50.733 mg / 49.760 mg
- PolyPOM 316L: 57.963 mg / 59.432 mg / 55.157 mg
- PolyMIM 17-4PH: 42.953 mg / 42.637 mg / 44.748 mg

### Thermal conductivity

The thermal conductivity  $\lambda$  was measured with a TCi "Thermal Conductivity Analyzer" (C-Therm Technologies Ltd., Canada) according to ASTM D7984-16. This was used in the solid area as well as in the melt area. The method is based on the "Modified Transient Plane Source" (MTPS) technique. For the measurement cylindrical specimens ( $\varnothing 60$  mm x 10 mm) are necessary which were produced by using a vacuum press type Plattenpresse P 200 PV (COLLIN Lab & Pilot Solutions GmbH, Germany). The used settings for the compression process are listed in Table 2 and the material was already heated up together with the hot cabinet. Furthermore, Table 3 lists the used temperatures for the thermal conductivity measurements. These temperatures were chosen to have thermal conductivity values below and above the peaks in the DSC curves because there the crystalline regions of the binder become amorphous and the thermal conductivity is expected to decrease. Every measurement was repeated at least 10 times for a specimen and every setting was tested with three different samples. As a contact agent, a silicone oil-based thermal joint compound type 120 (from Wakefield Thermal Solutions Inc., USA) was used to improve the heat flow between the specimen and the sensor.

Table 2: Setting for manufacturing specimens for thermal conductivity measurements.

Step	1	2	3	4	5
T (°C)	200	200	200	200	30
t (min)	15	5	5	5	10
p (bar)	1	50	100	150	150

Table 3: Used temperatures for the thermal conductivity measurements.

	T <sub>1</sub> (°C)	T <sub>2</sub> (°C)	T <sub>3</sub> (°C)	T <sub>4</sub> (°C)	T <sub>5</sub> (°C)
PolyPOM FN0805	25	60	170	190	-
PolyPOM 316L	60	160	180	200	-
PolyMIM 17-4PH	25	60	120	170	200

### **pVT-Measurement**

The specific volume, which is dependent on the pressure and the temperature was measured on a "PVT100" measurement device (SWO Polymertechnik GmbH, Germany) according to ISO 17744. The measurements were performed between 40 °C and 200 °C at 200/400/600/1000/1400/1600 bar. The linear cooling rate was 0.1 K/s.

### **Viscosity**

The viscosity was measured at three different temperatures on a "Rheograph RG50" high-pressure capillary rheometer (Göttfert Werkstoff-Prüfmaschinen GmbH, Austria) according to ISO 11443. The measurements were performed with a round die with a constant diameter of 1 mm and with four different die lengths (0.2 mm, 10 mm, 20 mm and 30 mm). For the rheological evaluation the correction methods according to Bagley and Weißenberg/Rabinowitsch were used. For every temperature the measurement was performed three times and the viscosity is the average of these. The measured shear rate range was between 10 s<sup>-1</sup> and 6000 s<sup>-1</sup> (before Weißenberg/Rabinowitsch - correction). The viscosity was only measured at high shear rates because previous experiments by Hubmann [20] as well as pretests with the same settings in Sigmasoft showed, that the high viscosity at low shear rates has a negligible effect and the extension of the Cross-WLF with the Herschel-Bulkley had almost no effect on the prediction of the injection pressure. Therefore, the Herschel-Bulkley extension was not used.

### **Thermogravimetric analysis**

The thermogravimetric analysis (TGA) was performed on a "TGA 1" (Mettler-Toledo, USA) under N<sub>2</sub> atmosphere (50 mL/min). After 5 minutes at 25 °C, the samples were heated to 650 °C with 20 K/min, where the temperature stayed constant for 10 min. The difference of the weight of the samples after the measurement was used to calculate the mass fraction of polymer or rather of the powder. The measurements were performed two times for the PolyPOM 316L and three times for the other two materials.

## **3.2 Experimental setup**

### **3.2.1 Machine and measurement equipment**

The experiments were performed on an "Arburg 320 C Allrounder 500-100" injection molding machine (Arburg GmbH + Co KG, Germany), which has a screw diameter of 20 mm. An additional pressure sensor "Kistler type 6125A" (Kistler Instrumente AG, Switzerland) with a measuring range of 0 bar – 2000 bar was used to measure the pressure in the machine nozzle. This sensor was connected to an "HBM Spider 8" data acquisition system (Hottinger Baldwin Messtechnik GmbH, Germany) which sent the measuring data to the software "catman AP 4.2" on a computer. Furthermore, the pressure sensor was calibrated with a piston manometer type CPB5000HP (WIKA Alexander Wiegand SE & Co. KG, Germany) prior to the injection molding experiments. The received measuring points were approximated by a quadratic function, which was used in catman to convert the voltage into pressure (Figure 13).

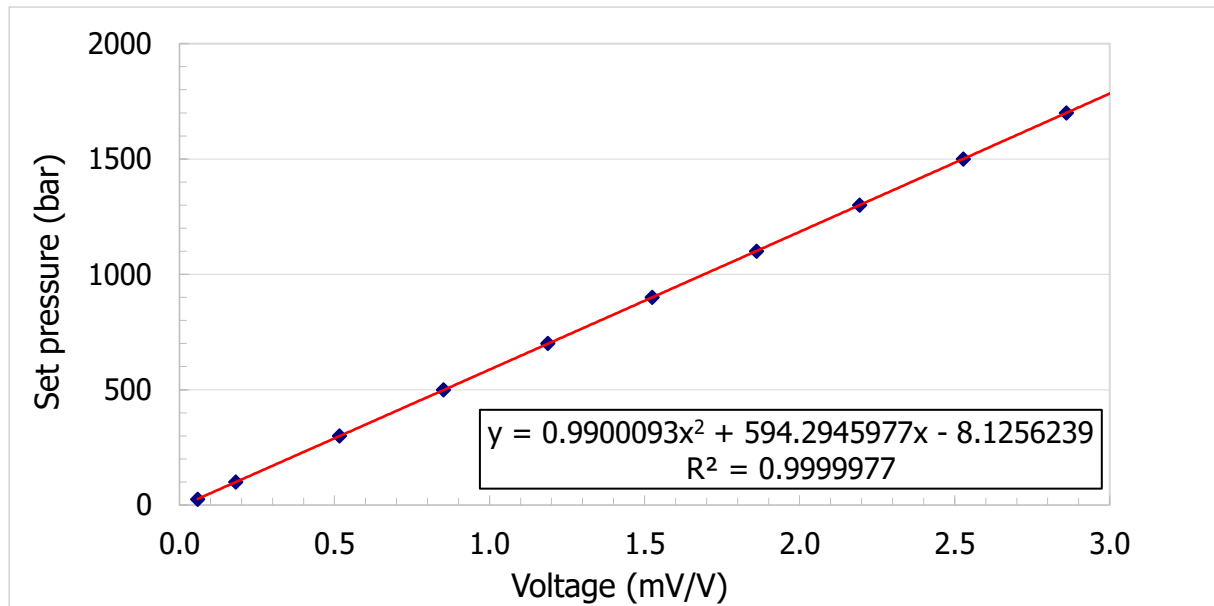


Figure 13: Measuring points for the pressure sensor calibration approximated by a quadratic function.

The core and cavity plates of the used mold can be changed and two variants were available. One variant offers the possibility to produce multipurpose test specimens according to DIN EN ISO 3167 in a two-cavity configuration. Due to a too low shot volume of the injection molding machine, one of the two cavities was sealed with a cut off polypropylen (PP) specimen. The other used core and cavity plates are designed for producing round dog bone specimens according to DIN EN ISO 2740, which are used for tensile tests with sintered MIM materials. This variant also comes along with two cavities. Compared to the multipurpose test specimens, the dog bone specimens have a smaller volume and therefore both cavities can be filled within one shot. For temperature controlling a "Wittmann Temprom plus C 160" temperature control unit (Wittmann Battenfeld GmbH, Austria) was used. The tempering channels of the two plates were connected and the used tempering fluid (water) entered the circulation through the moveable plate (clamping unit) on the bottom side (Figure 14 on page 21). The geometries of the used mold and the produced parts are shown in Figure 36 - Figure 38 in the appendix (page 59-60).

### 3.2.2 Experimental plan

As already mentioned, the filling studies with all three feedstocks and two different cavities were performed at different mold temperatures and different injection rates. There are some settings that were kept constant for all filling studies, which are shown in Table 4. The recommended nozzle temperature (190 °C for all materials) was increased by 10 K because of the inefficient heating situation due to a too short heater band. The recommended mold temperatures for the injection molding process according to the data sheets are:

- PolyPOM FN0805: 115 °C – 135 °C
- PolyPOM 316L: 115 °C – 135 °C
- PolyMIM 17-4PH: 40 °C – 60 °C

Table 4: Constant injection molding machine settings.

Maximum injection pressure		2300 bar
Packing pressure		no packing pressure (0 cm <sup>3</sup> /s) for 8 s
Back pressure		10 bar
Circumferential screw speed		10 m/min
Barrel temperatures	PolyPOM FN0805	200 °C - 188 °C - 185 °C - 178 °C - 175 °C
	PolyPOM 316L	200 °C - 188 °C - 185 °C - 182 °C - 175 °C
	PolyMIM 17-4PH	200 °C - 185 °C - 180 °C - 175 °C - 170 °C
Feeding volume	Tensile specimens	25 cm <sup>3</sup>
	Dog bone specimens	20 cm <sup>3</sup>
Rest cooling time	Tensile specimens	30 s
	Dog bone specimens	15 s

For the fillings studies the feeding volumes were kept constant and only the switch over points were varied. Since there was no packing pressure (volume flow of 0 cm<sup>3</sup>/s), the injected volume was only depending on the set switch over point. For every setting the material was injected three times and the occurring pressure at the pressure transducer in the machine nozzle was measured. The chosen switch over points had to be adjusted for the different materials to get a comparable filling degree, due to a different material behavior. However, at different injection rates, which also led to a slightly different filling degree, the switch over points were kept the same to receive comparable results. The full experimental plan with all variants is shown in Table 5, which can be read from left to right for every material. The used mold temperatures were outside of the recommended range and were increased to a critical value, where the melt almost stayed in a liquid state (according to the cooling curves of the DSC measurements in Figure 15 on page 26). While for the two POM based materials some mold temperature settings were far below the recommended settings, the lowest chosen mold temperature for PolyMIM 17-4PH (40 °C) was already in the recommended range. The other two mold temperatures (80 °C and 120 °C) of the PolyMIM material were chosen above the first and the second crystallization peak in the DSC curve. In addition, also two filling studies at different injection speeds but at only one mold temperature were performed with a polypropylene. This material was chosen as a comparison of the flow behavior between feedstocks and unfilled thermoplastics.



Table 5: Experimental plan for filling studies on injection molding machine.

Material	Mold temperature (°C)	Injection rate (cm <sup>3</sup> /s)	Cavity	Injected volume (cm <sup>3</sup> )
Polypropylene	30	5, 20	Tensile	7, 9, 17, 15.5
			Dog bone	5.1, 6.6, 9.7, 10.5
PolyPOM FN0805	80, 100, 120 140, 150	5, 20	Tensile	3.5, 8, 10, 16, 17, 18
			Dog bone	5.3, 5.7, 7, 10.7, 11.1
PolyPOM 316L	80, 100, 120 140, 150	5, 20	Tensile	4, 8.3, 10.3, 16.5, 17.5, 18.5
			Dog bone	5.2, 5.6, 6.8, 10.5, 10.9
PolyMIM 17-4PH	40, 80, 120	5, 20	Tensile	4.3, 8.6, 10.6, 16.8, 17.8, 18.8
			Dog bone	5.3, 5.7, 7, 10.6, 11

### 3.3 Simulation

#### 3.3.1 Modell setup

The simulation of the injection molding process was performed with Sigmasoft v5.2. The project was set up with the material type "MIM/CIM Feedstock". The CAD geometry of the mold, the cavity and the cooling channels were imported. While for the tensile specimens the cavity is only in the moveable mold, the parting line of the dog bone specimens is exactly in the middle of the specimens. For a better comparison of the simulated pressure and the measured pressure with the sensor, the nozzle (up to the pressure sensor) was also added and considered in the simulation (see Figure 39 in the appendix on page 60). This was realized as a hot runner with the property "TC Runner", which is surrounded by a cylinder with a diameter of 10 mm as "TC Mold". The hot runner was split into two different geometry sets, to enable a different property assignment. All geometry components, which are used in the simulation are shown in Figure 14. Additionally, Table 6 defines the property of every component as well as the used mesh parameter for this property. For the dog bone part, two additional equivalent cuboids of 6 mm x 4 mm x 3 mm were positioned to the two gates as dummy elements (between end of runner and part itself). This enables a local increase of the mesh resolution because the gates are quite small compared to the other geometries. The order of the components is also very important because geometries at the end of the list will be cut away from geometries above. Therefore, Table 6 also defines the order of the elements in Sigmasoft. The last difference between the simulations of the different cavities (tensile or dog bone specimen) is the part itself. The tensile specimen part has a total volume of 16.38 cm<sup>3</sup>, whereas the dog bone specimen part has a volume of 8.71 cm<sup>3</sup> (according to the CAD file). The standard settings for the mesh were only partly edited and are completely described in Table 7.

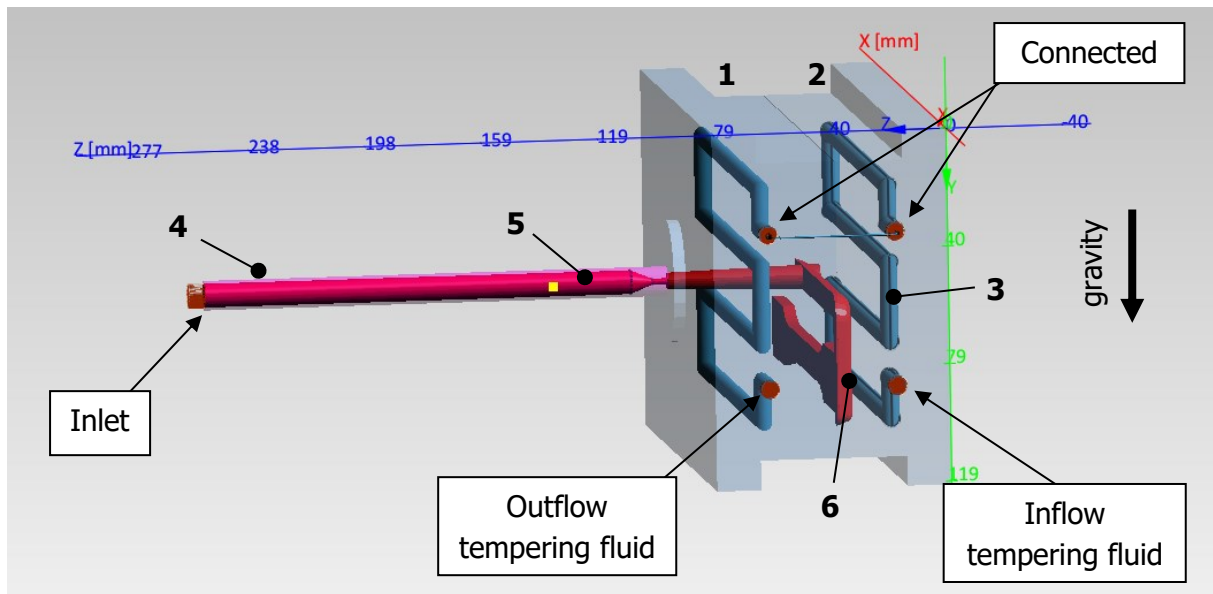


Figure 14: Numbered geometry components with boundaries for the simulation.

Table 6: List of the geometry components with the used properties and the mesh parameters.

Nr.	Name	Property	Mesh parameter
-	Dummy element	Permanent mold	Dummy
1	Fixed mold	Fixed mold	Rough
2	Moveable mold	Moveable mold	Rough
3	Tempering channel	Tempering channel	Rough
4	Cylinder	TC mold	Rough
5	Hot runner - big cylinder with cone	TC runner 1	Fine
	Hot runner - small cylinder	TC runner 2	Very fine
6	Tensile / dog bone specimen	Part	Fine

Table 7: Mesh parameters for the different mesh settings.

		Rough	Fine	Very fine	Dummy
Geometry filter (mm)	x	5.0	1.0	0.4	0.75
	y	5.0	1.0	0.4	0.6
	z	5.0	1.0	1.0	0.5
Subdivision filter (-)	x	3	3	3	3
	y	3	3	3	3
	z	3	3	3	3
Minimal element size (mm)	x	5.0	0.5	0.16	0.25
	y	5.0	0.5	0.16	0.2
	z	5.0	0.5	0.5	0.16
Max. length ratio of neighboring elements		2	2	3	3
Max. aspect ratio of an element		5	3	3	3
Number of coarsening loops		3	1	1	1
Coarsening threshold		3	5	5	5

The used settings for the simulation are listed in Table 8. The used mold material was 40CrMnMo7, which is approximately equal to P20 steel (American Iron and Steel Institute, AISI). The initial melt temperature was set 10 K lower than the actual nozzle temperature, due to experimental experience. For the heat transfer coefficients, the automatic standard values had been chosen. As an approximation, the cylinder (TC mold) was isolated to the part and the mold ( $0.001 \text{ W/m}^2\cdot\text{K}$ ). Only for merged geometries, there is a heat flow while the mold is open. The simulation will be performed without a heating up phase, which means the mold is already perfectly tempered at the start. Nevertheless, five heating cycles are simulated, to obtain the temperature distribution after some cycles. Therefore, a preparation time of 7 s was considered between cycles, where the mold is open. This consists of the time for opening and closing the mold, the ejecting time and the time for manually removing of the part. The injection time was calculated with the CAD volume and the corresponding flow rate, to obtain a 100 % filled part. There is no packing phase in the simulation because the results will only be compared with the experimental filling study. The "open mold step after"-time consists of the injection time, the packing time (8 s with  $v = 0 \text{ cm}^3/\text{s}$  in the experiments) and the rest cooling time. Even though the injection time changed in the experimental filling study and further the cycle time changed, the "open mold step after" values were only calculated with the longest injection time for the used flow rate. For other general simulation parameters, the standard values were used. The steps (percent filled) of the filling results were set to 1 % intervals.

Table 8: General settings for the simulation in Sigmasoft v5.2.

<b>Temperatures</b>			
	PolyPOM FN0805	PolyPOM 316L	PolyMIM 17-4PH
Melt temperature, TC mold	190 °C		
<b>Heat transfer coefficients</b>			
Fixed and movable mold / part	4000 W/m <sup>2</sup> ·K		
TC mold / part	0.001 W/m <sup>2</sup> ·K		
TC mold / TC runner	4000 W/m <sup>2</sup> ·K		
TC mold / fixed mold	0.001 W/m <sup>2</sup> ·K (merged)		
Fixed mold / movable mold / tempering channel	10000 W/m <sup>2</sup> ·K		
<b>Cycle control</b>			
Number of heating cycles	5		
Production cycles	1		
<b>Molding process</b>			
	Tensile specimen	Dog bone specimen	
Preparation time	7 s		
Flow rate	5 cm <sup>3</sup> /s for 3.276 s 20 cm <sup>3</sup> /s for 0.819 s	5 cm <sup>3</sup> /s for 1.742 s 20 cm <sup>3</sup> /s for 0.435 s	
Packing	deactivated		
Open mold step after	41.276 s (v = 5 cm <sup>3</sup> /s) 38.819 s (v = 20 cm <sup>3</sup> /s)	24.742 s (v = 5 cm <sup>3</sup> /s) 23.435 s (v = 20 cm <sup>3</sup> /s)	

### 3.3.2 Material properties

The measured pvT data and viscosity data were fitted with Sigmasoft. For the pvT the Tait model and for the viscosity data the Cross-WLF model was used to fit the data. As already mentioned before, the Cross-WLF model was used without an extension for low shear rates. In the pvT diagram the PolyMIM 17-4PH material exhibits a second transition area at 50°C for 200 bar and 65°C for 1600 bar, but the Tait model can only describe one transition area. Therefore, the measuring points below this second transition region were neglected for an improvement of the fitting. As the focus is only on the filling phase of the simulation the second transition area will be hardly reached anyway. The pvT material type was set to semi-crystalline for all three feedstocks and the resulting coefficients for the viscosity and the pvT model are listed in Table 9 and Table 10. Additionally, the approximated Cross-WLF curves with the measuring points are shown in the appendix in Figure 40 - Figure 42 (page 61-62). Since the no-flow temperature was based on the pvT diagram, the D<sub>3</sub> value of the Cross-WLF model is

### 3 Experimental

automatically set to the same value as  $b_6$  in the Tait model. No crystallization, viscosity relaxation or extensional rheological model was used.

Table 9: Coefficients for the Cross-WLF viscosity model.

	PolyPOM FN0805	PolyPOM 316L	PolyMIM 17-4PH
$A_1$ (-)	2.1218	1.2920	1.4511
$A_2$ (K)	60.9845	46.8591	79.4370
$n$ (-)	0.5678	0.5986	0.3960
$D_1$ (Pa·s)	4.2790e+007	7406.3320	2838.0229
$D_2$ (°C)	190	190	190
$D_3$ (K/bar)	0.0166	0.0148	0.0250
$D_4$ (Pa)	0.0647	2214.9331	59293.9531

Table 10: Coefficients for the Tait pvT model.

	PolyPOM FN0805	PolyPOM 316L	PolyMIM 17-4PH
High temperature region			
$b_{1m}$ (cm <sup>3</sup> /g)	0.2127	0.1874	0.1961
$b_{2m}$ (cm <sup>3</sup> /(g·K))	5.8508e-005	4.0039e-005	4.6413e-005
$b_{3m}$ (bar)	2393.1650	3793.6956	3039.3608
$b_{4m}$ (1/K)	-7.1432e-003	2.5575e-003	-1.2925e-004
Low temperature region			
$b_{1s}$ (cm <sup>3</sup> /g)	0.2033	0.1800	0.1934
$b_{2s}$ (cm <sup>3</sup> /(g·K))	8.8974e-006	7.6853e-007	4.3946e-005
$b_{3s}$ (bar)	6526.3833	8822.5400	3954.5078
$b_{4s}$ (1/K)	-3.6268e-003	-5.5876e-003	1.9770e-003
Limit temperature			
$b_5$ (°C)	154.9995	155.0451	128.7988
$b_6$ (K/bar)	0.0166	0.0148	0.0250
Transition region			
$b_7$ (cm <sup>3</sup> /g)	8.8953e-003	7.5445e-003	2.4717e-003
$b_8$ (1/K)	0.0938	0.0932	0.1081
$b_9$ (1/bar)	1.8198e-003	1.6979e-003	2.9712e-003

### 3 Experimental

Furthermore, particle segregation parameters with activated "Backcoupling" were used. There are also two parameters ("interface particle concentration" and "core viscosity correction factor") to manipulate the viscosity, which are changing the flow front to a plug flow. Mainly the standard values are used, but also some further settings were tried to improve the results:

1.) Standard values:

interface particle concentration = 2; core viscosity correction factor = 0.3

Pretests with extreme values (other material was used):

2.) These values were used individually and together:

interface particle concentration = 10; core viscosity correction factor = 0.03

3.) Standard values without "Backcoupling"

Actual simulation with measured material data:

4.) interface particle concentration = 4; core viscosity correction factor = 0.3

5.) interface particle concentration = 4; core viscosity correction factor = 0.4

6.) interface particle concentration = 6; core viscosity correction factor = 0.4

For the simulation also the initial particle concentration (solids loading in 2.2, Eq. ( 1 )) is needed. From the datasheets of the materials only the densities of the sintered materials are given. The weight fractions of particles and binders were obtained from the TGA measurements. To calculate the volume fraction at least two densities (feedstock, binder and/or powder) have to be known. As the sintered part exhibits low porosity, the density of the powder might be a little bit higher. This is an unknown factor and to minimize the error, it was assumed that the sintered part exhibits a density of 99 % of the theoretical value. The density of the feedstock was obtained from the pVT diagram. Sigmasoft automatically extrapolates the pVT data to 1 bar and outputs density values in dependence of the temperature. All these values are given in Table 11 with the standard deviations based on a sample. The used data for the specific heat is shown in Table 13 in the appendix (page 63) and the resulting (cooling) curves are shown in Figure 15. Additionally, the mean particle radiuses of the materials are necessary, which are estimated with the help of a scanning electron microscope (SEM) (see Figure 43 - Figure 45 in the appendix on page 64 - 65). Between the materials clear differences are identifiable and the estimated particle radiuses are:

- PolyPOM FN0805: 2.5  $\mu\text{m}$
- PolyPOM 316L: 8  $\mu\text{m}$
- PolyMIM 17-4PH: 5  $\mu\text{m}$

Table 11: Results of the TGA analysis with values for Sigmasoft.

	Density particle (g/cm <sup>3</sup> )	Density feedstock (pvT) (g/cm <sup>3</sup> )	Particle concentration (wt.%)	Particle concentration (vol.%)	Density difference particle/matrix (g/cm <sup>3</sup> )
PolyPOM FN0805	7.727	4.949	87.06 ± 0.08	55.75 ± 0.05	6.203 ± 0.007
PolyPOM 316L	8.030	5.559	91.73 ± 0.14	63.5 ± 0.10	6.690 ± 0.018
PolyMIM 17-4PH	7.768	5.319	93.17 ± 0.08	63.8 ± 0.05	6.687 ± 0.010

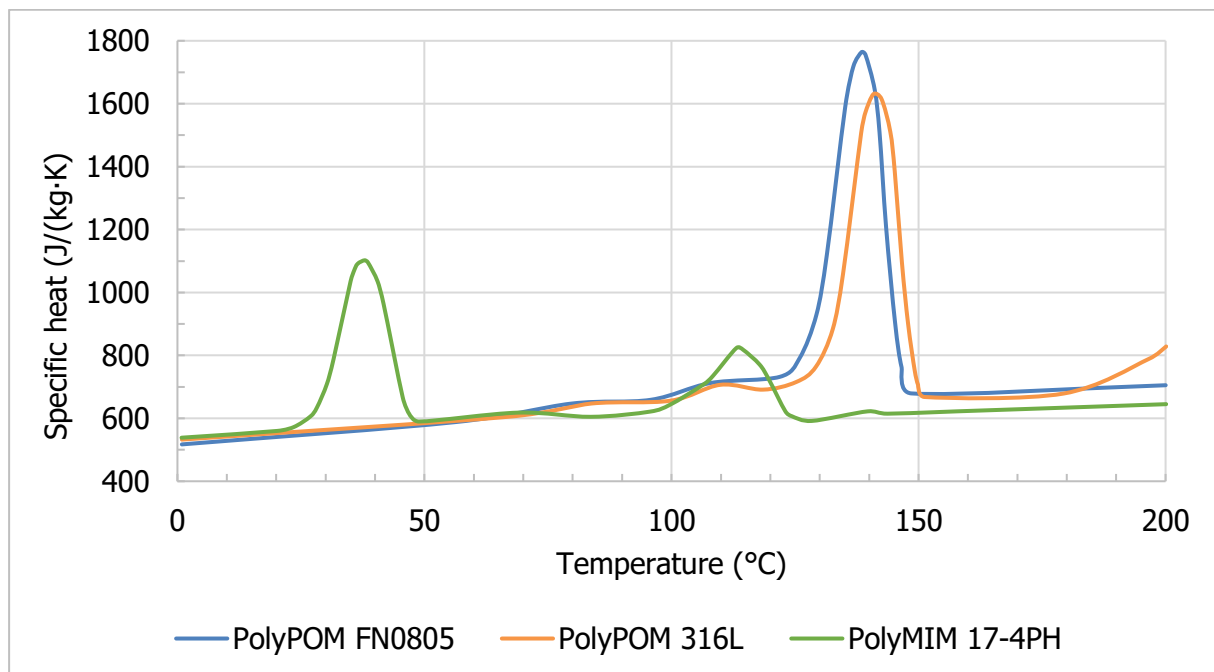


Figure 15: Specific heat of the three feedstocks with a cooling rate of 20 K/min.

The used thermal conductivities  $\lambda$  are given in Table 12, which is also diagrammed in Figure 46 in the appendix (page 65) with the standard deviations. The thermal conductivity drops due to the change of the thermal conductivity of the semi-crystalline binder. For PolyPOM FN0805 only the value at room temperature was used in the simulations because of a lack of experience with the measuring method at high temperatures and the strongly decreasing thermal conductivity with higher temperatures. With a higher thermal conductivity, the material will cool down faster, hence the calculated pressure in the simulation is expected to rise. Generally, the pressure in the simulation is underestimated and therefore this might correct the pressure into the right correction. Nevertheless, additional simulations were performed with the full thermal conductivity profile of PolyPOM FN0805 to visualize the effects. In the manufactured cylinders for the measurement with PolyMIM 17-4PH, still grain boundaries between the granulates were visible, which were not avoidable with different

### 3 Experimental

manufacturing settings and might lead to a lower thermal conductivity. Although the interesting temperature range is covered with these values it is noticeable, that the Sigmasoft simulation software assumes a constant thermal conductivity above and below the defined temperature range.

Table 12: Thermal conductivity values for the simulation with Sigmasoft.

Nr.	PolyPOM FN0805		PolyPOM 316L		PolyMIM 17-4PH	
	T (°C)	$\lambda$ (W/m·K)	T (°C)	$\lambda$ (W/m·K)	T (°C)	$\lambda$ (W/m·K)
1	24.9	4.09	61.6	3.82	26.5	4.05
2	(61.8)	(4.20)	160.4	3.34	61.0	3.98
3	(170.3)	(1.81)	179.9	2.84	121.0	3.33
4	(189.1)	(1.63)	199.3	2.55	170.3	2.51
5					200.0	2.60



## 4 Results

### 4.1 Filling pattern

The chosen steps (1-6) in the filling studies for the tensile specimens are visualized in Figure 16 and the figure should further serve as a simple overview about the different filling situations in the mold. The two sections (a) and (b) show the experimental results for PolyPOM FN0805, where (a) was performed with the lowest mold temperature of 80 °C and (b) with the highest mold temperature of 150 °C. The recommended mold temperature is between 115 °C and 135 °C and therefore (a) and (b) are extreme examples. The influence of the mold temperature on the filling behavior will be discussed later and (b) should only serve as an additional comparison to the other two sections. The section (c) shows the simulation results of (a) and the different flow front is clearly visible in the steps 2-5. While there is a fountain flow in the simulation (c), the material in (a) is already frozen at the surface and only pushed through the cavity without a fountain flow (4 - 6). Every step in (a) and the results of the simulation (c) will be discussed in detail later. The last section (d) shows the experimental filling study of PP at a mold temperature of 30 °C. Here the flow front exhibits the same geometry as the simulation of the PolyPOM FN 0805 (c) and the fountain flow is fully developed. Although the flow front in (b) is more like (c) and (d) than (a), there is still a difference (see step 4).

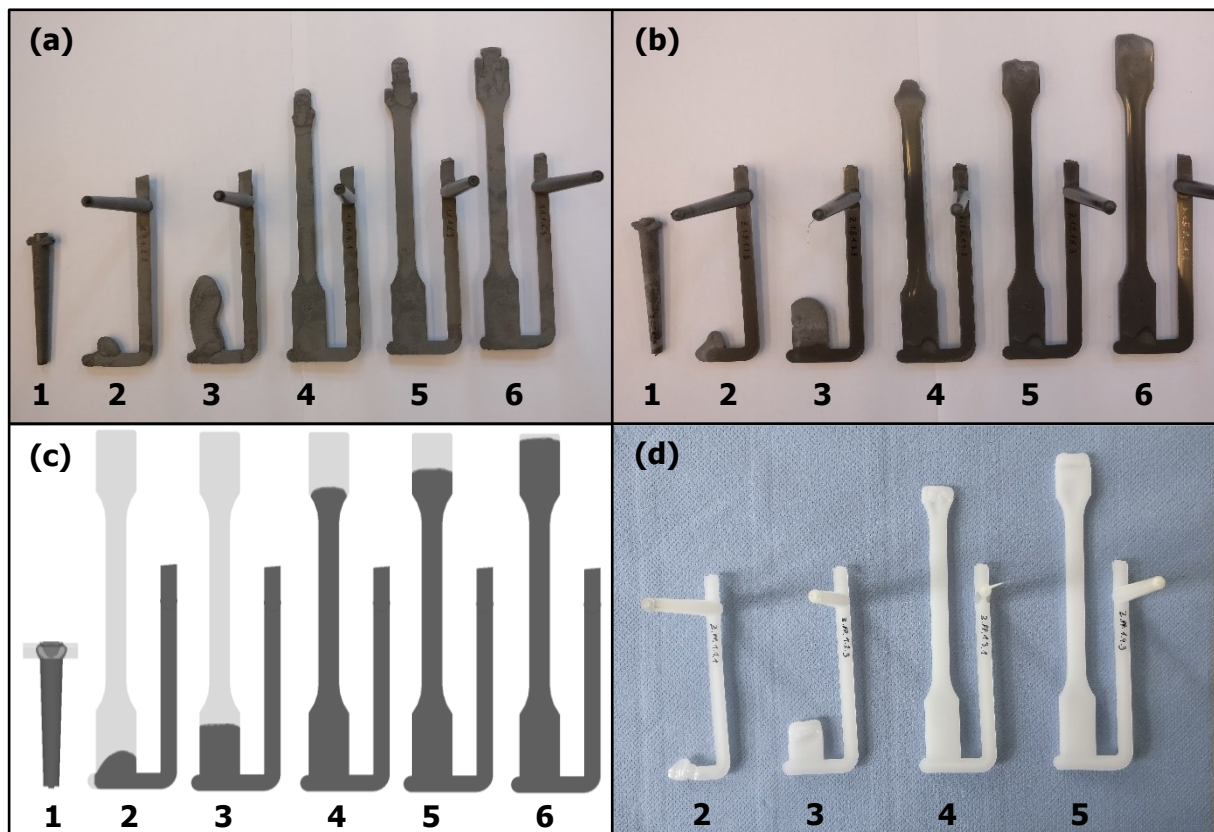


Figure 16: Filling studies of tensile specimens of PolyPOM FN0805 (a-c) and PP (d) for an injection rate of 5 cm<sup>3</sup>/s in six steps where (a): experimental for  $T_{\text{Mold}} = 80$  °C; (b) experimental for  $T_{\text{Mold}} = 150$  °C; (c) simulation for  $T_{\text{Mold}} = 80$  °C; (d) experimental for  $T_{\text{Mold}} = 30$  °C.

The same overview is shown for the dog bone specimens in Figure 17. Again, the sections (a) and (b) show the experimental filling studies for PolyPOM FN0805 at the lowest chosen mold temperature (80 °C in (a)) and the highest chosen mold temperature (150 °C in (b)). Generally, the visible effects are the same as previously for the tensile specimens. Whereas (a) exhibits clearly jetting in 1 and an unregular filling in step 2/3, the simulation (c) shows a fully developed fountain flow. This jetting could not be avoided for any material by the used mold temperatures or injection rates in the experiments. Also, step 4 and 5 exhibit a different flow front. The simulation just looks like the experimental results with PP (d), where also no jetting occurs. Again, this stands in contrast to the actual material behavior.

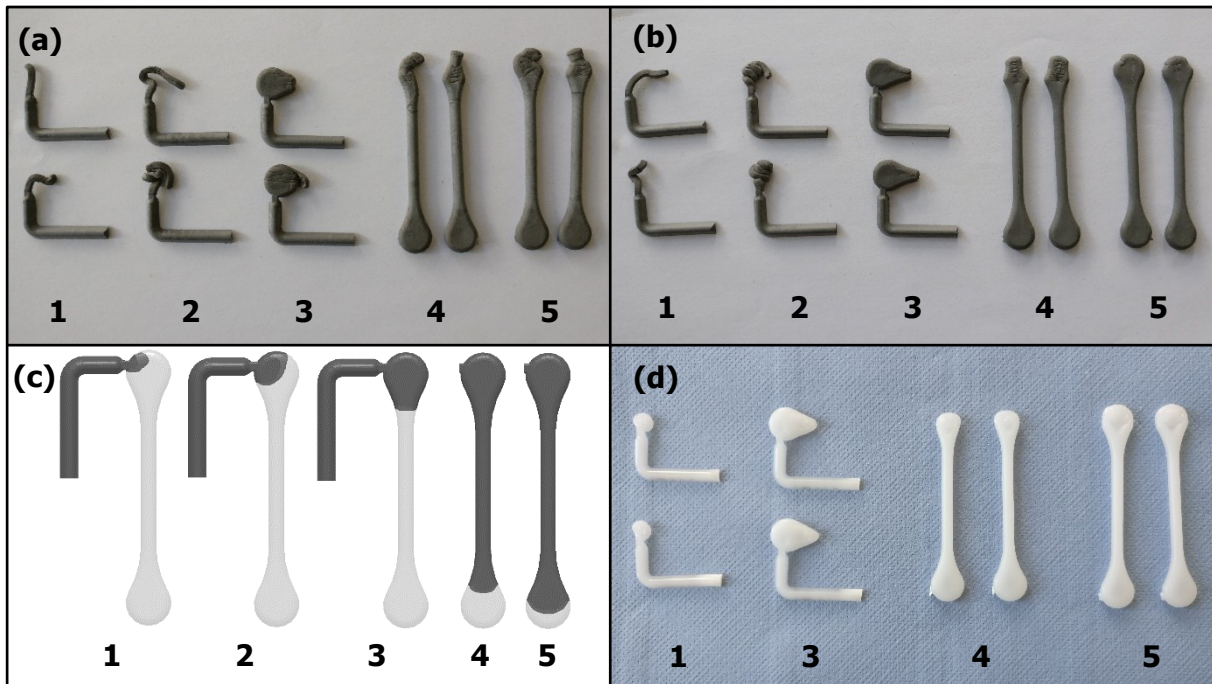


Figure 17: Filling studies of dog bone specimens of PolyPOM FN0805 (a-c) and PP (d) for an injection rate of  $5 \text{ cm}^3/\text{s}$  in five steps where (a): experimental for  $T_{\text{Mold}} = 80 \text{ °C}$ ; (b) experimental for  $T_{\text{Mold}} = 150 \text{ °C}$ ; (c) simulation for  $T_{\text{Mold}} = 80 \text{ °C}$ ; (d) experimental for  $T_{\text{Mold}} = 30 \text{ °C}$ .

The following figures (Figure 18 - Figure 23) show a series of filling study pictures of PolyPOM FN0805 tensile specimens at all chosen mold temperatures with an injection rate of  $5 \text{ cm}^3/\text{s}$  at different filling steps. With this representation, the influence of the mold temperature on the flow behavior of the feedstock is highlighted and the hypothesis can be visually analyzed. Since the other materials and the dog bone specimens show similar effects for a variation of the mold temperature, these figures are representative for all results. Nevertheless, the other figures of all performed filling studies are shown in the appendix in Figure 49 - Figure 102 (page 68 - 90). At a mold temperature of 150 °C, where the feedstock is hardly solidified and the specimens were very soft after ejection, the surface of the specimens got smooth and shiny (only PolyPOM feedstocks). This can be explained by the binder/plastic which migrates to the surface. In contrast, the specimens at low temperatures exhibit a very rough and dim surface which further exhibits lots of flow marks. The first step of the filling study is not shown because the sprue looks very similar for all settings.

## 4 Results

In step 2 of the filling study (Figure 18), there is also a change of the thickness in the channel at the flow front because beside the thicker runner the thinner film gate appears, which leads the material into the actual cavity (Figure 37). Here the material tends to stay in the runner in flow direction until the runner ends. Only at the highest temperature (150 °C), there is a change in the flow behavior and the material flows evenly in all directions.

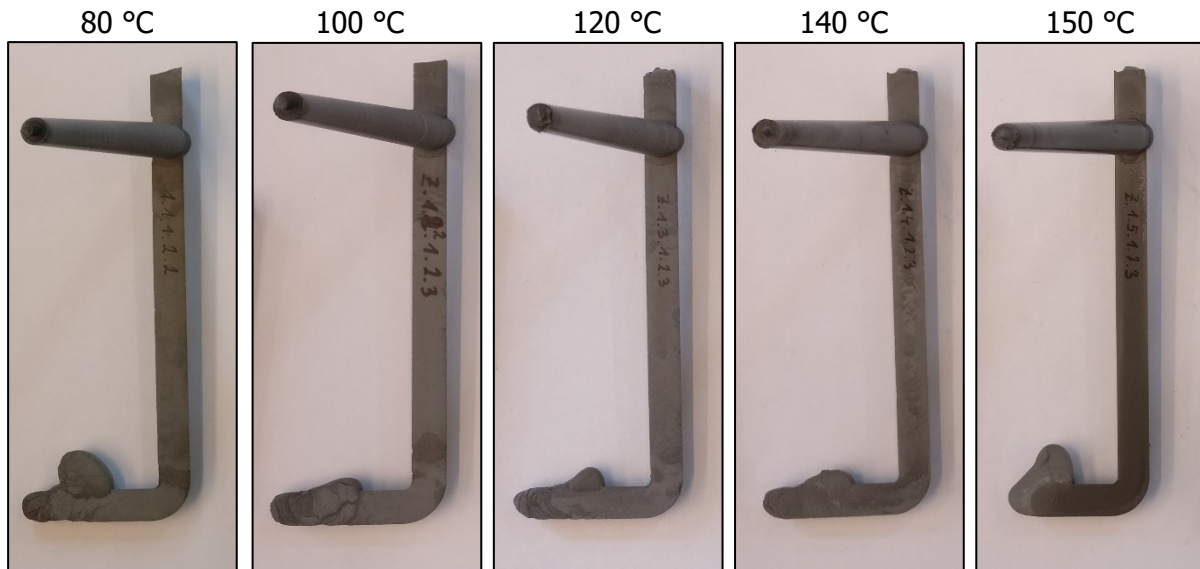


Figure 18: Step 2 of the filling study of PolyPOM FN0805 tensile specimens at an injection rate of 5 cm<sup>3</sup>/s at different mold temperatures.

Figure 19 shows the next step, where the material is already filling the specimen cavity. With increasing temperature, there is a continuous improvement of the filling. Whereas the material at the lowest temperature is not evenly spread over the whole width, there is an almost regular filling at the highest temperature (apart from a small weld line). Especially at 80 °C the material is not really flowing, but only pushed into one direction until there is a resistance. At this point, there is also another change of the cavity thickness because the material flows from the thin gate into the thicker specimen cavity. This also results in a different filling behavior, which further explains the different lengths of the flow paths. Therefore, Figure 20 shows the specimens for a mold temperature of 100 °C and 150 °C from another perspective. The material at low mold temperatures does not really spread out over the thickness and just moves straight forward. In contrast at the highest mold temperature, the material is fully distributed over the thickness. Furthermore, an unexpected resulting weld line is visible at the higher temperature.

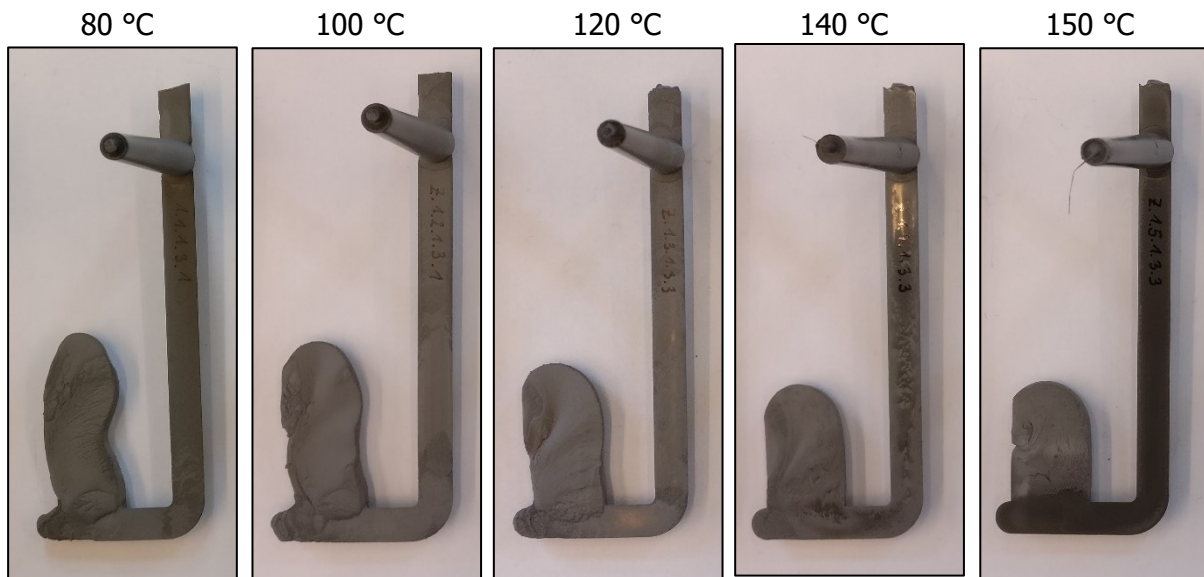


Figure 19: Step 3 of the filling study of PolyPOM FN0805 tensile specimens at an injection rate of  $5 \text{ cm}^3/\text{s}$  at different mold temperatures.



Figure 20: Tensile specimens of step 3 of the filling study at  $100 \text{ }^\circ\text{C}$  and  $150 \text{ }^\circ\text{C}$  mold temperature of PolyPOM FN0805 at an injection rate of  $5 \text{ cm}^3/\text{s}$ .

The other three chosen steps of the filling study (Figure 21 - Figure 23) are already at the end of the filling process and will be discussed together. Here the material at the flow front had already a lot of time to cool down ( $\sim 3 \text{ s}$  for an injection rate of  $5 \text{ cm}^3/\text{s}$ ). Although the width of the cavity increases, the material keeps its shape and moves unchanged forward at the lower mold temperatures. When this partly frozen material reaches the end of the cavity the pressure in the melt rises and the incoming material is pushed past the sides of the unchanged material and clearly visible weld lines are formed. For the temperatures of  $80 \text{ }^\circ\text{C}$  –  $120 \text{ }^\circ\text{C}$  this effect is hardly reduced by increasing temperatures. At  $140 \text{ }^\circ\text{C}$  there is still material in the middle in every step, which is further ahead, but there is less material which is pushed along the sides. This is a transition to the effect at  $150 \text{ }^\circ\text{C}$ , where only in step 4 some material is further ahead. But in the next two steps, this is not visible anymore and there is a regular filling of the mold as it would be expected for a fully developed fountain flow.

#### 4 Results

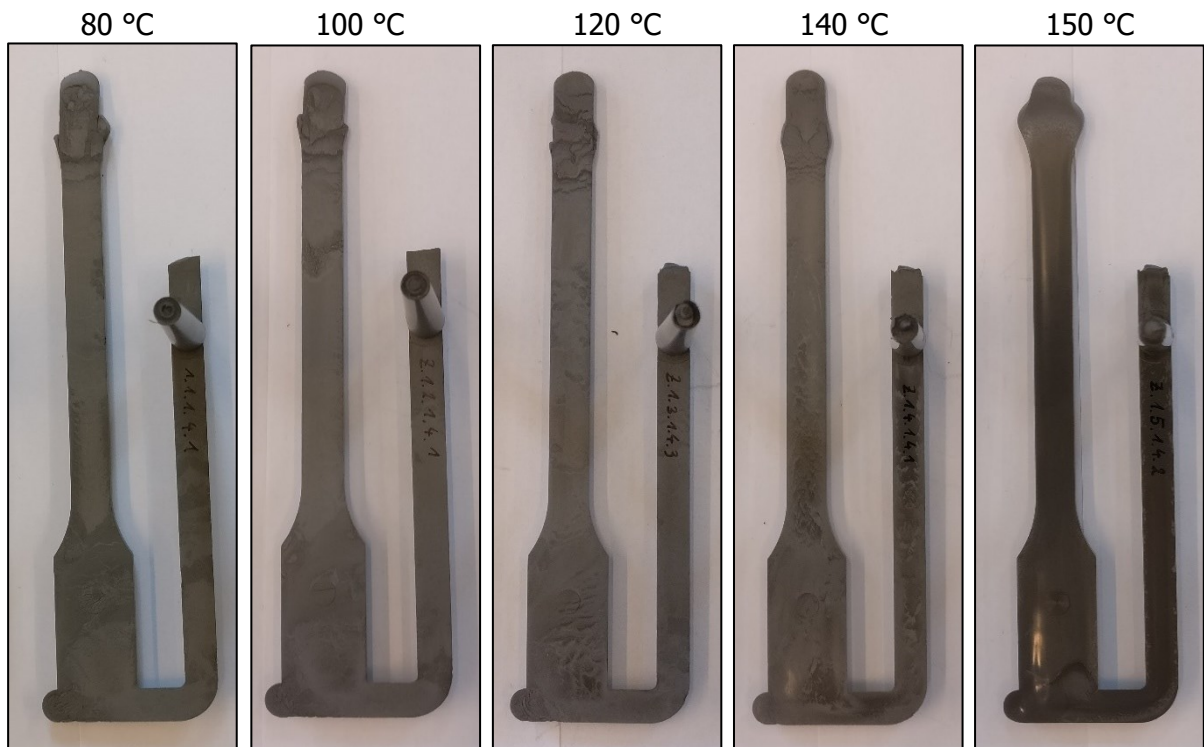


Figure 21: Step 4 of the filling study of PolyPOM FN0805 tensile specimens at an injection rate of 5 cm<sup>3</sup>/s at different mold temperatures.

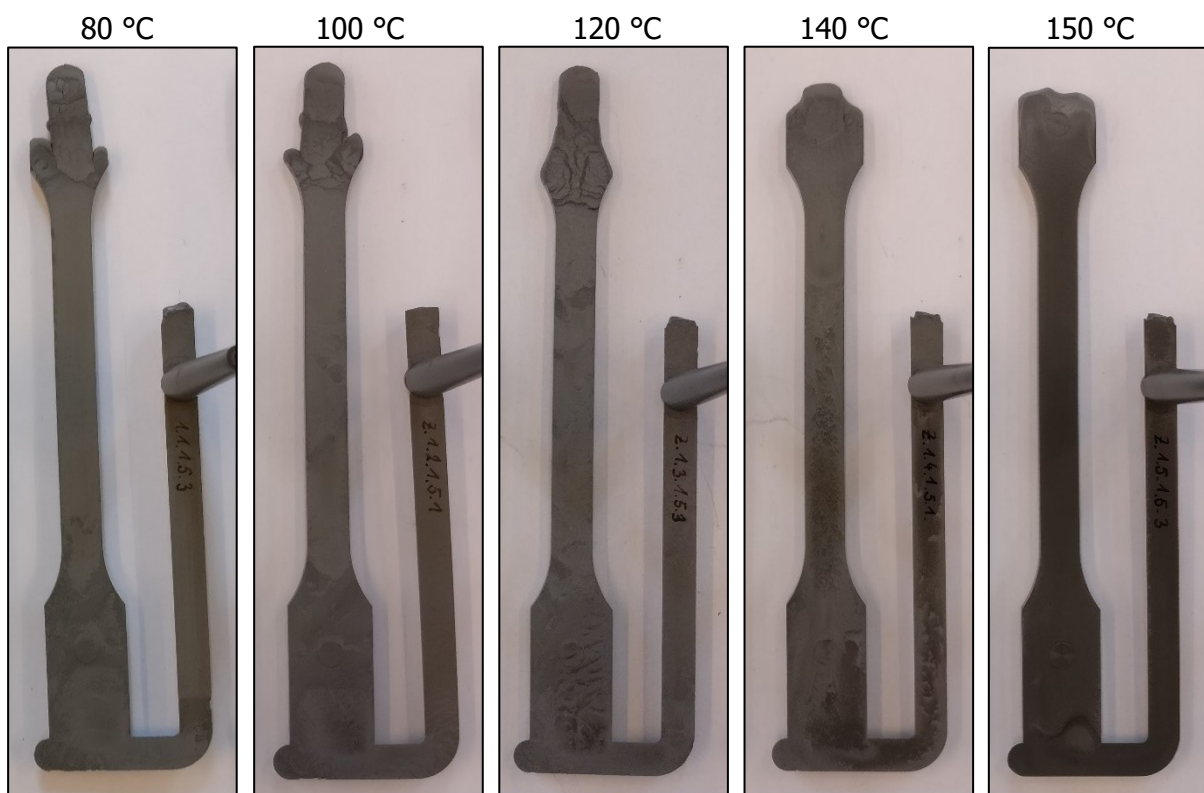


Figure 22: Step 5 of the filling study of PolyPOM FN0805 tensile specimens at an injection rate of 5 cm<sup>3</sup>/s at different mold temperatures.

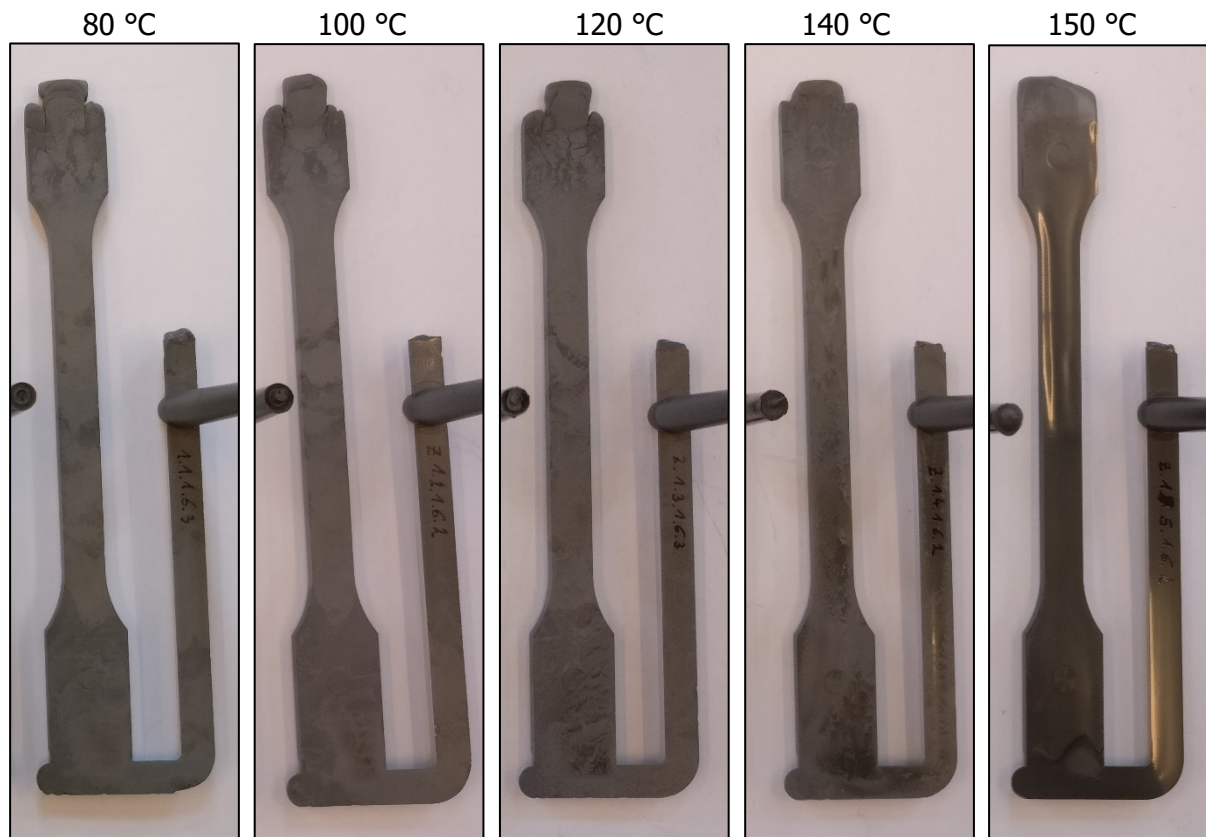


Figure 23: Step 6 of the filling study of PolyPOM FN0805 tensile specimens at an injection rate of  $5 \text{ cm}^3/\text{s}$  at different mold temperatures.

The influence of the injection rate is similar to the influence of the mold temperature. With a higher injection rate, the material does not keep its shape as much as at lower injection rates. However, this stands in contrast to the fact that generally a higher injection rate tends more to a jetting behavior. There is less time for cooling, hence the melt is warmer and the viscosity lower. Therefore, also the appearance of the shiny surface (PolyPOM feedstocks) was shifted to a lower mold temperature. Another effect at higher injection rate was a higher degree of filling, which might also be due to the machine control. Hence, at some points the steps in the filling study looked different for the same injection volumes and sometimes the specimen was already fully filled in step 6. Apart from that, generally the flow behavior has not changed with a higher injection rate. There were still the same effects which were reduced at higher mold temperatures. The difference between the injection rates is visualized as an example in Figure 24 for PolyPOM FN0805 tensile specimens at  $T_{\text{mold}} = 80 \text{ °C}$ .

Another phenomenon appeared in the filling process of PolyPOM 316L dog bone specimens at higher mold temperatures ( $> 140 \text{ °C}$ ), which is shown in Figure 25. With both injection rates a separating of a surface layer occurred in step 4 and 5. This layer exhibits a darker and smoother surface than the material body within. This cannot be due to fast cooling, as it only appears at high mold temperatures and therefore it might be a result of powder-binder segregation. Further, it has not appeared at tensile specimens, therefore it might also be a result of the special geometry.

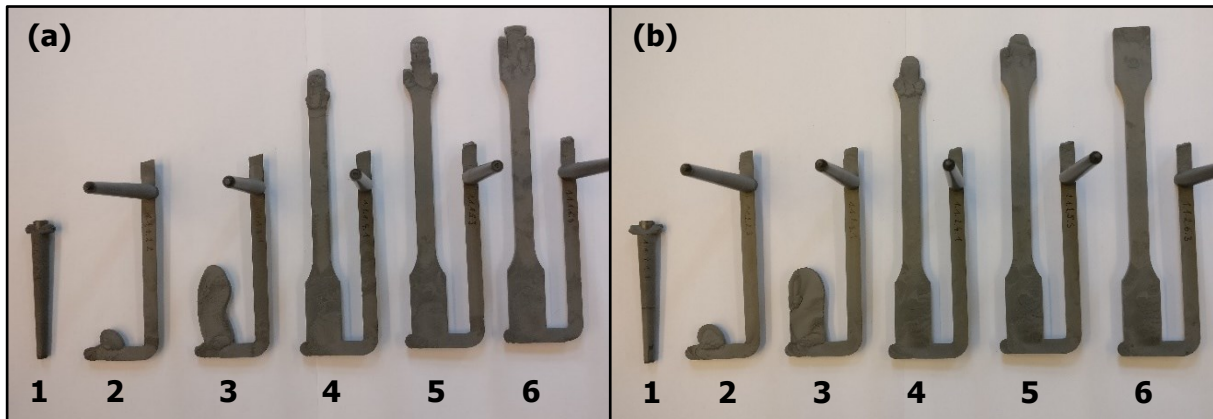


Figure 24: Filling study of tensile specimens of PolyPOM FN0805 at  $T_{\text{mold}} = 80 \text{ }^{\circ}\text{C}$  for an injection rate of (a)  $5 \text{ cm}^3/\text{s}$  and (b)  $20 \text{ cm}^3/\text{s}$ .

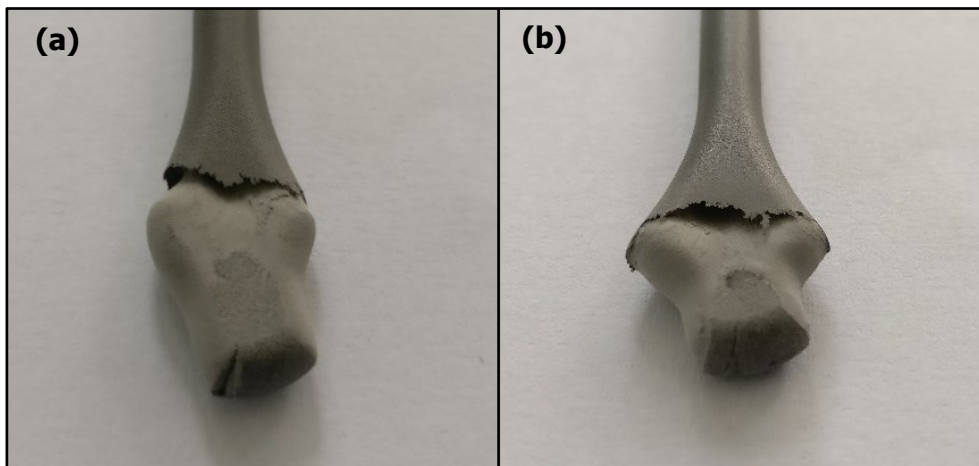


Figure 25: Separating of a surface layer in the filling process of PolyPOM 316L dog bone specimens at higher mold temperatures ( $150 \text{ }^{\circ}\text{C}$ ), where (a) is step 4 and (b) is step 5 of the filling study for an injection rate of  $20 \text{ cm}^3/\text{s}$ .

All performed experimental filling studies point out the same conclusions. There is no sudden change in the flow behavior and the variation of the mold temperature changes the flow behavior continuously step by step. Thus, no threshold temperature, where the flow behavior changes from a fountain flow to an almost solidified material, which is pushed through the cavity, could be found visually. Nevertheless, all materials with all settings (except one) showed the same flow behavior and the melt tended to keep its form and direction, which stands in a clear contrast to the flow behavior of unfilled thermoplastics (for example PP). Only for the tensile specimens of PolyPOM FN0805 with the highest mold temperature ( $150 \text{ }^{\circ}\text{C}$ ) and an injection rate of  $20 \text{ cm}^3/\text{s}$  this phenomenon could be fully avoided and the flow front was comparable to PP.

As already shown in the overviews in Figure 16 and Figure 17 (page 28 and 29), the simulation of the filling process predicted a completely different filling behavior, which was equal to the experimental filling with PP. Independent of the used mold temperature and injection rate settings, in general for every material the same filling behavior with a fountain flow was predicted, although inertia was always considered in the simulation model, which should

account for jetting phenomena. No simulation predicted results, which are similar to reality. Even though there are the two parameters "interface particle concentration" and "core viscosity correction factor", which manipulate the viscosity in a way to account for some kind of wall slip effects, the general filling behavior was unaffected.

## 4.2 Pressure

The influence of the mold temperature on the injection pressure is shown in Figure 26 (injection rate  $\dot{V} = 5 \text{ cm}^3/\text{s}$ ) and Figure 27 ( $v = 20 \text{ cm}^3/\text{s}$ ) for the tensile specimens for all used injection volumes. Every value is the average of three measurements. The data points in the diagrams also contain error bars with the minimum and maximum values, which are hardly visible due to the low variation. The pressure curves of the dog bone specimens are shown in the appendix in Figure 47 and Figure 48 (page 66 - 67). They exhibit the same trends and therefore they will not be discussed separately. For the tensile specimens with the material PolyPOM 316L, the pressures at the lowest mold temperature for injection volumes of  $17.5 \text{ cm}^3$  and  $18.5 \text{ cm}^3$  could not be measured because the pressure sensor was limited at around 1800 bar. Moreover, the PolyPOM 316L tensile specimens with an injection rate of  $20 \text{ cm}^3$  were not produced with an injection volume of  $18.5 \text{ cm}^3$  to avoid damaging the sensor because the specimens were already fully filled.

With increasing mold temperature, the injection pressure decreases due to a higher melt temperature and consequently a lower viscosity of the material. At high injection volumes which require higher pressures due to a longer flow path, there is a high influence of the mold temperature. This effect decreases with a lower injection volume (smaller slope of the linear approximation). A lower injection volume is equal to a shorter injection time which means that there is less time where the mold can affect the melt temperature and therefore the flow behavior. At the lowest injection volume, where only the sprue without the runner was filled, the influence is even reversed, and the pressure slightly rises with a higher mold temperature. This might be due to a different wall contact and a special filling situation in this initial area. At low mold temperatures, there might be no wall contact and a strongly distinct jetting, which would result in a low flow resistance. In contrast, at higher mold temperatures there might be a conventional fountain flow and due to the higher resistance, a higher injection pressure is needed. Since the dog bone cavity used the same sprue, this setting was not performed for the dog bone specimens, hence the lowest investigated volume is already at a higher degree of filling.

It is very interesting and noticeable, that the injection pressure changes with an almost perfectly linear function with the variation of the mold temperature, which can be shown in every single curve. When comparing the materials even the slope of the linear approximation for every filling degree is very similar, although the PolyMIM 17-4PH consists of a completely different binder material. Since there is no sudden change of the pressure when the mold temperature is around the transition temperature region of the materials (according to the measured DSC curves, see Figure 15 on page 26), the same conclusions as from the filling pattern can be assumed: There is no sudden change in the flow behavior.



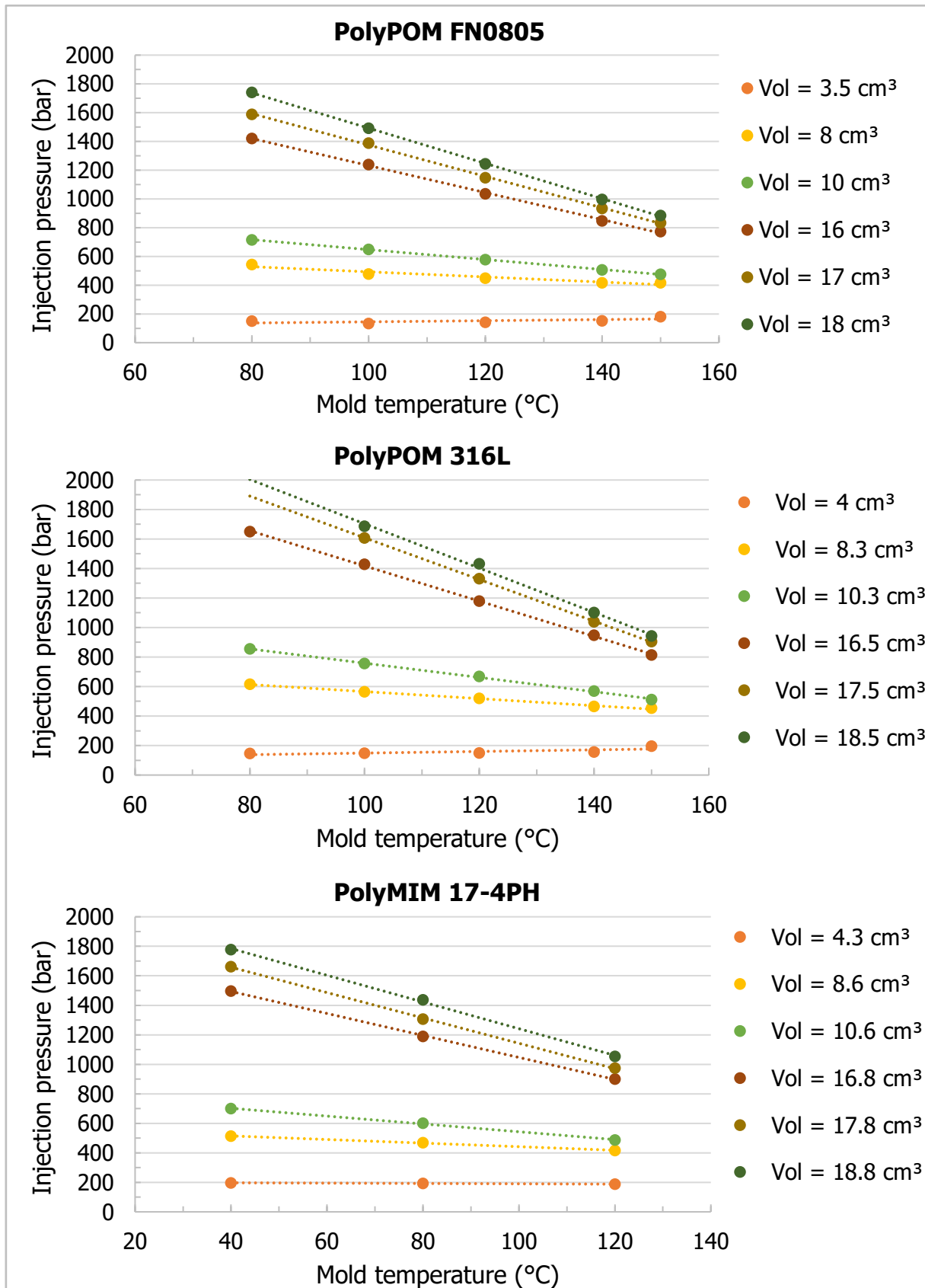


Figure 26: Injection pressures of the tensile specimens for all three materials in dependence of the mold temperature with linear approximations for all used injection volumes (Vol) and for an injection rate of 5 cm<sup>3</sup>/s.

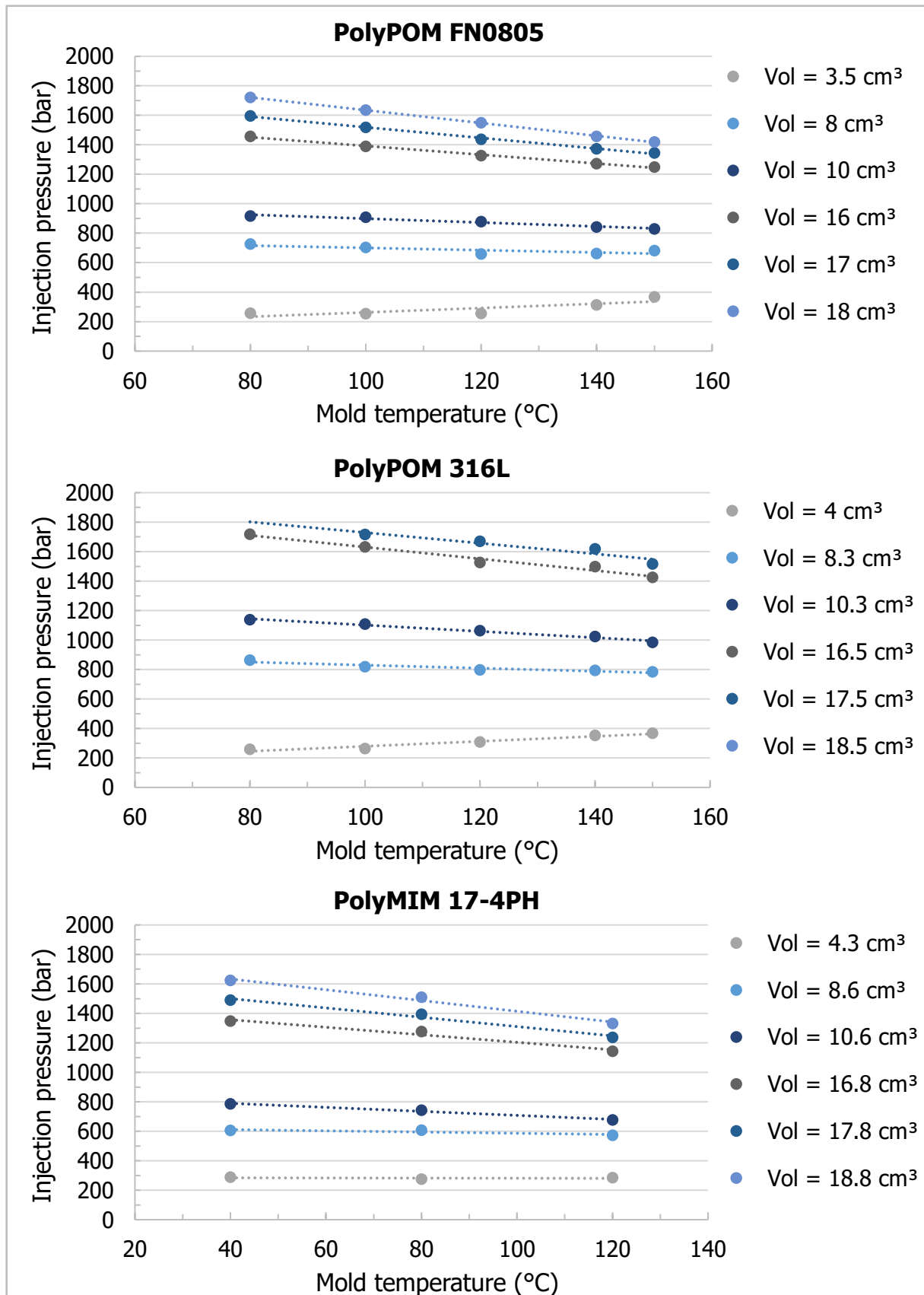


Figure 27: Injection pressures of the tensile specimens for all three materials in dependence of the mold temperature with linear approximations for all used injection volumes (Vol) and for an injection rate of 20 cm³/s.

When comparing the different injection rates with each other (Figure 26 with Figure 27) at the same injection volumes, the different influence of the mold temperature (different slopes of the linear approximation) is visualized. This is additionally shown in Figure 28 for PolyPOM FN0805, where especially the different slopes at the higher injection volumes are standing out (red framed area). For a better visualization of the influence of the injection rate, Figure 29 and Figure 30 show the injection pressure of the tensile specimens in dependence of the injection rate for all mold temperatures at the lowest and highest injection volume (second highest volume for PolyPOM 316L, due to the limitation of the pressure sensor). Generally, the findings of Figure 30 represent the red-framed area in Figure 28, which is similar for all three feedstocks.

At low injection volumes, there is a clear increase of the pressure with a higher injection rate for all mold temperatures (Figure 29). This can also be found for high injection volumes with high mold temperatures (Figure 30). In contrast, at a high injection volume and the lowest used mold temperature, the injection pressure is almost independent of the injection rate or sometimes even higher at lower injection rates. This can be explained by the theoretically four times longer injection time for the same volume. At high injection volumes and additionally low mold temperatures, the melt can cool down a lot at low injection rates. Thus, the viscosity is clearly increased and the injection pressure increases. Also, for high injection volumes the differences between the pressures at different mold temperatures are getting lower at a high injection rate.

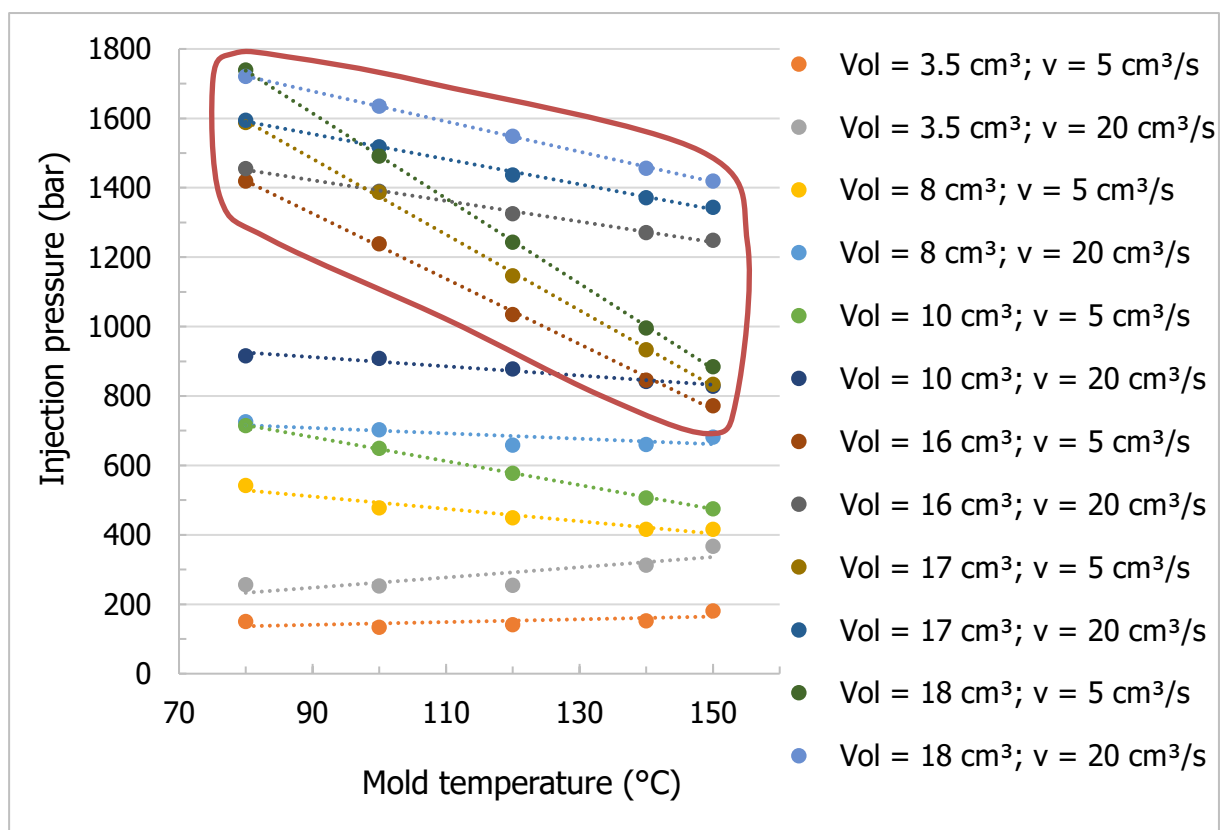


Figure 28: Injection pressures of the PolyPOM FN0805 tensile specimens in dependence of the mold temperature with linear approximations for all used injection volumes (Vol) and both injection rates.

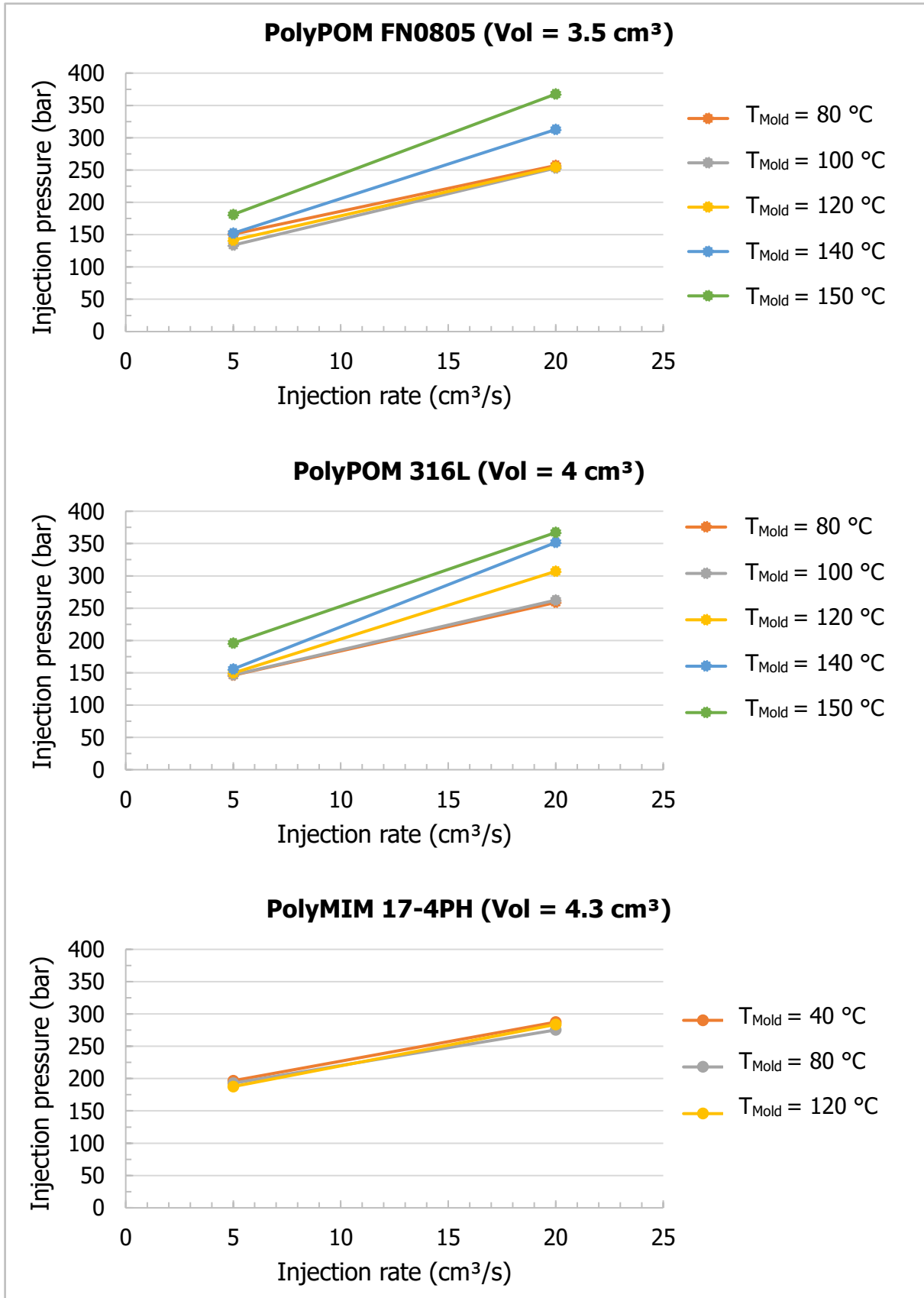


Figure 29: Injection pressures of the tensile specimens for all three materials in dependence of the injection rate at filling step 1.

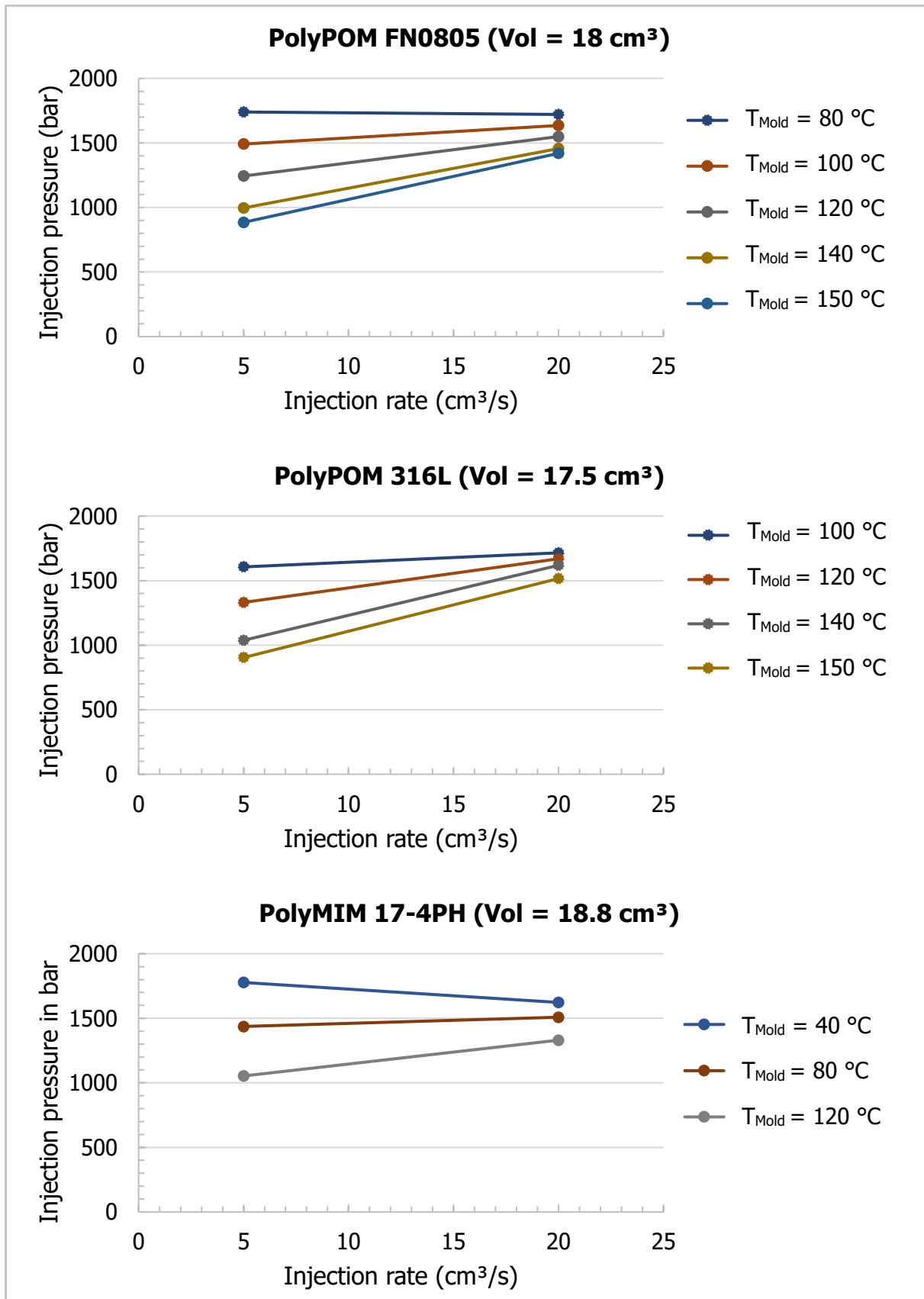


Figure 30: Injection pressures of the tensile specimens for all three materials in dependence of the injection rate at filling step 5 (PolyPOM 316L) and filling step 6 (PolyPOM FN0805 and PolyMIM 17-4PH).

By comparison of the pressure curves over the time of the experiment and the simulation, an unexpected pressure peak appears at the beginning of the filling (Figure 31 and Figure 32), which has different reasons. In the experiment, this mainly occurs at lower mold temperatures. Due to the cold mold, the die of the injection unit cools down significantly and the material solidifies at the nozzle tip. Therefore, the pressure increases until the melt starts to flow, which causes the pressure to fall again and results in this peak in the measured curve. Afterwards, the pressure is rising again with the covered flow path. This could be avoided or reduced by a longer waiting time between the cycles (more time for the die for heating up again) and by a higher mold temperature. In contrast, for some other reason, this peak also appears in the simulation because at the beginning of the filling the material has always the set melt temperature in the hot runner and there cannot be freezing effects. The explanation might be, that Sigmasoft automatically included a ramp in the flow rate. Therefore, in the first steps of the simulation, there are very low flow rates and shear rates which further leads to a high viscosity. Respectively more pressure will be needed at the beginning. After the flow rate reached the actual value the shear rates increase and the viscosity and the pressure fall again. The phenomenon in the simulation was not reduced by the different settings. If the pressure maximum of an experiment was caused by the discussed phenomenon, which mainly happened at low injection volumes, the used value for the analysis was corrected to the actual injection pressure at the end of the curve. From Figure 31, which shows the pressure profiles PolyPOM FN0805 tensile specimens with a mold temperature of 80 °C and a flow rate of 5 cm<sup>3</sup>/s, it might be concluded, that the predicted profile from the simulation is comparable to the reality. But this is the only simulation, which predicted the pressure quite well. Generally, the pressure was underestimated and the generated pressure curves looked like the representative curve in Figure 32.

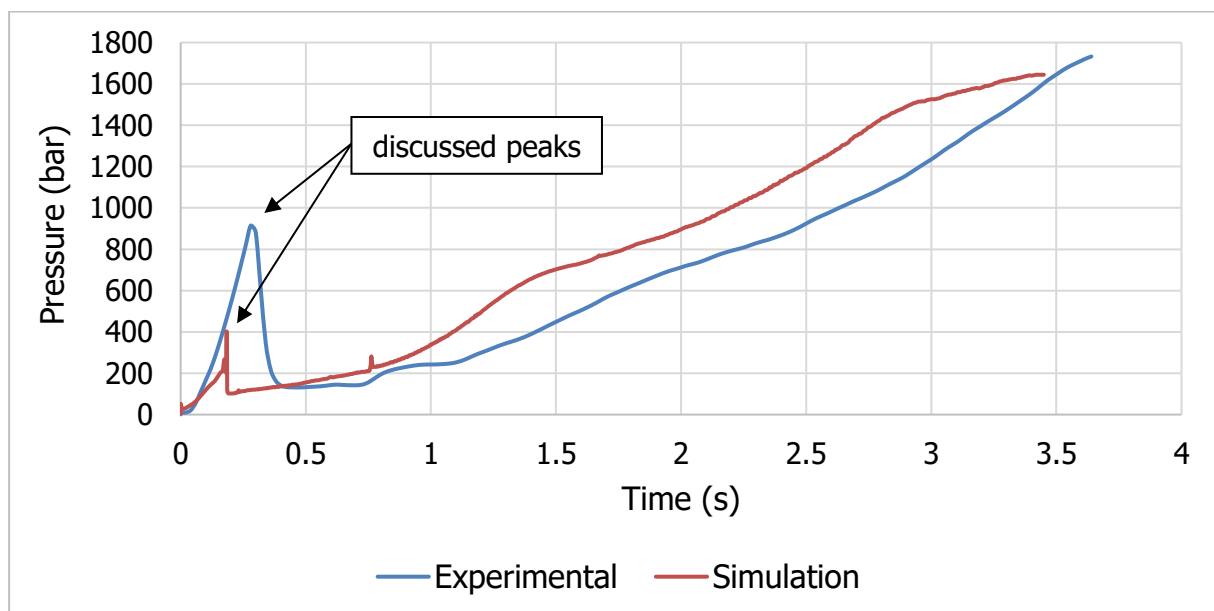


Figure 31: Experimental and simulation results of the injection pressure over time for PolyPOM FN0805 with  $\dot{V} = 5 \text{ cm}^3/\text{s}$  and  $T_{\text{Mold}} = 80 \text{ }^\circ\text{C}$ .

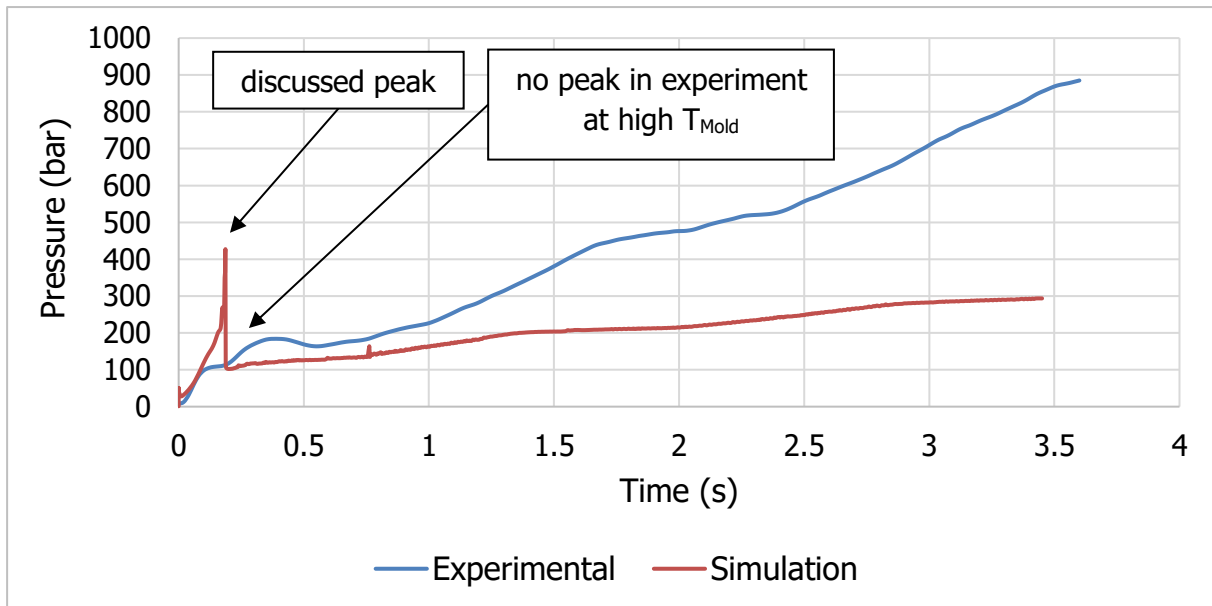


Figure 32: Experimental and simulation results of the injection pressure over time for PolyPOM FN0805 with  $\dot{V} = 5 \text{ cm}^3/\text{s}$  and  $T_{\text{Mold}} = 150 \text{ }^\circ\text{C}$ .

The magnitude of the deviation between the measured pressure in the experiment and the predicted pressure in the simulation is shown in Figure 33. For this purpose, for every material four simulations have been performed and the pressure differences in percent referred to the measured pressures from the last step of the filling studies were calculated. The degree of filling at the last step of the filling studies was estimated to get the corresponding pressure in the simulation. The error bars in Figure 33 show the results with the maximum and minimum pressures of the three repetitions in the experiment. Every time the predicted pressure in the simulation was significantly lower. Thus, not only the flow behavior but also the pressure was completely wrongly predicted. With the lowest mold temperature and the lower injection rate, the dog bone cavity was not even fully fillable with two materials in the simulation, while they could be molded in the experiment. Apart from that, these settings produced the best results (difference 5.6 % - 40.6 %), due to the low temperatures and therefore the higher viscosity. For the other three settings, the pressure differences of PolyPOM FN0805 (52.4 % - 66.7 %) are smaller than the pressure differences of the other two (80.3 % - 90.9 %), which were almost the same. The fact that the PolyPOM 316L and the PolyMIM 17-4PH, which have a different binder system, exhibit similar values might be by pure chance. The pressures for the dog bone specimens were slightly better predicted, which can be explained by the different geometry (other flow paths and lengths, two cavities).

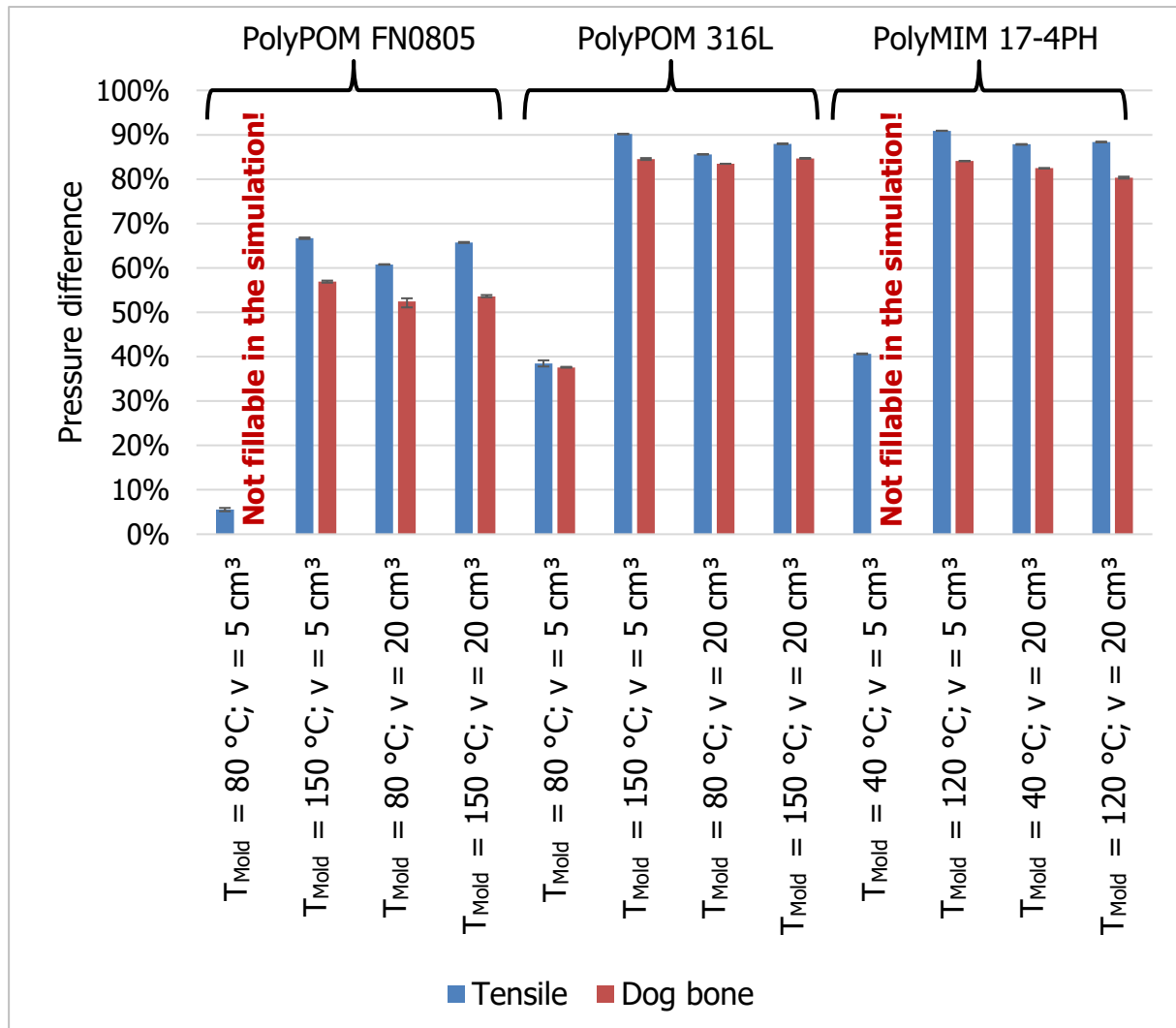


Figure 33: Pressure difference between the values of the experiment and the simulation in % referred to the measured pressure from the experiment.

As described earlier in 3.3.1 "Modell setup", the initial melt temperature in the simulation (190 °C) was set lower than the actual nozzle temperature (200 °C) because of the bad heating situation at the nozzle. By an increase of the initial melt temperature to 195 °C, only the calculated pressure in the simulation decreases, but no changes in the simulated flow behavior appears. The two parameters "interface particle concentration" and "core viscosity correction factor" in Sigmasoft, manipulate the viscosity and therefore can increase and improve the calculated pressure. This is only reverse engineering by trial and also the appearing flow front is affected significantly, which can lead to reversed flow fronts (material at the wall is slipping forward) which neither are corresponding to the experiments nor are physically explainable. Pre-tests with these parameters also showed, that instabilities (unexplainable pressure jumps in the curve) can occur if the "core viscosity correction factor" is too big. For PolyPOM FN0805 the simulations were performed with only one value (at room temperature) for the thermal conductivity. An additional simulation with the temperature dependent thermal conductivity showed the complex correlations (contrary to the expectations), which will be noted here, even though the simulation results generally do not represent the reality. By using the full profile, the thermal conductivity is reduced by a factor of  $\sim 2.5$  at temperatures higher than



190 °C. While, with an injection rate of 5 cm<sup>3</sup>/s and a mold temperature of 80 °C, for the tensile specimen the pressure with the full profile is always higher or equal, the dog bone specimen exhibits a different behavior (Figure 34). Until approximately 80 % degree of filling the pressure is lower (max. 16 %) in the simulation with the high single point value (area below 0.2 s neglected), which can be explained by Figure 35. This figure shows the temperature of the material at 80 % degree of filling, where two different effects occur. In the sprue the material has its first contact with the cooler mold and the skin of the hot material cools down very fast, due to the high heat transfer between the material and the mold. With the high single point value, the heat of the hot material in the center of the flow channel is transported outwards faster than with the low thermal conductivity value, which results from the full profile. Consequently, the material close to the mold wall stays warmer. The new incoming material tends to flow in the middle since here the resistance is lower and therefore there is always hot material. Thus, there is a stronger cooling effect in the channel with the full profile, which further results in a higher pressure. Above 80 % degree of filling the pressure in the simulation with the single point conductivity gets higher (up to ~ 15 %), due to the cooler material farther away from the inlet. Here the inner material had already enough time to transport the heat outwards. These effects depend also on the geometry since concerning the pressure for the tensile specimen the first discussed effect (more hot material in the sprue) is predominating the other.

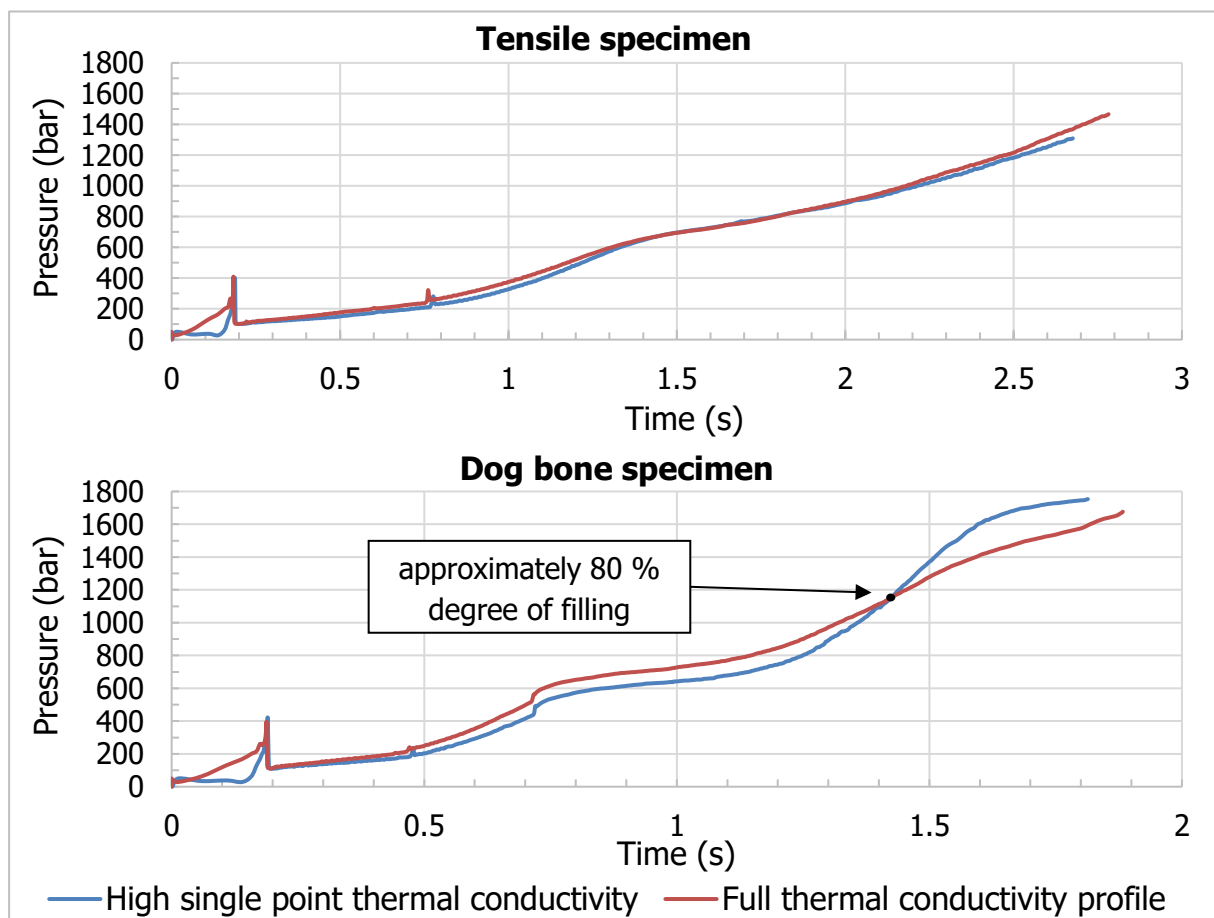


Figure 34: Injection pressure of the simulation of both cavities with PolyPOM FN0805 with the high single point value for the thermal conductivity (blue) and the full thermal conductivity profile (red) ( $T_{\text{Mold}} = 80 \text{ °C}$ ,  $\dot{V} = 5 \text{ cm}^3/\text{s}$ ).

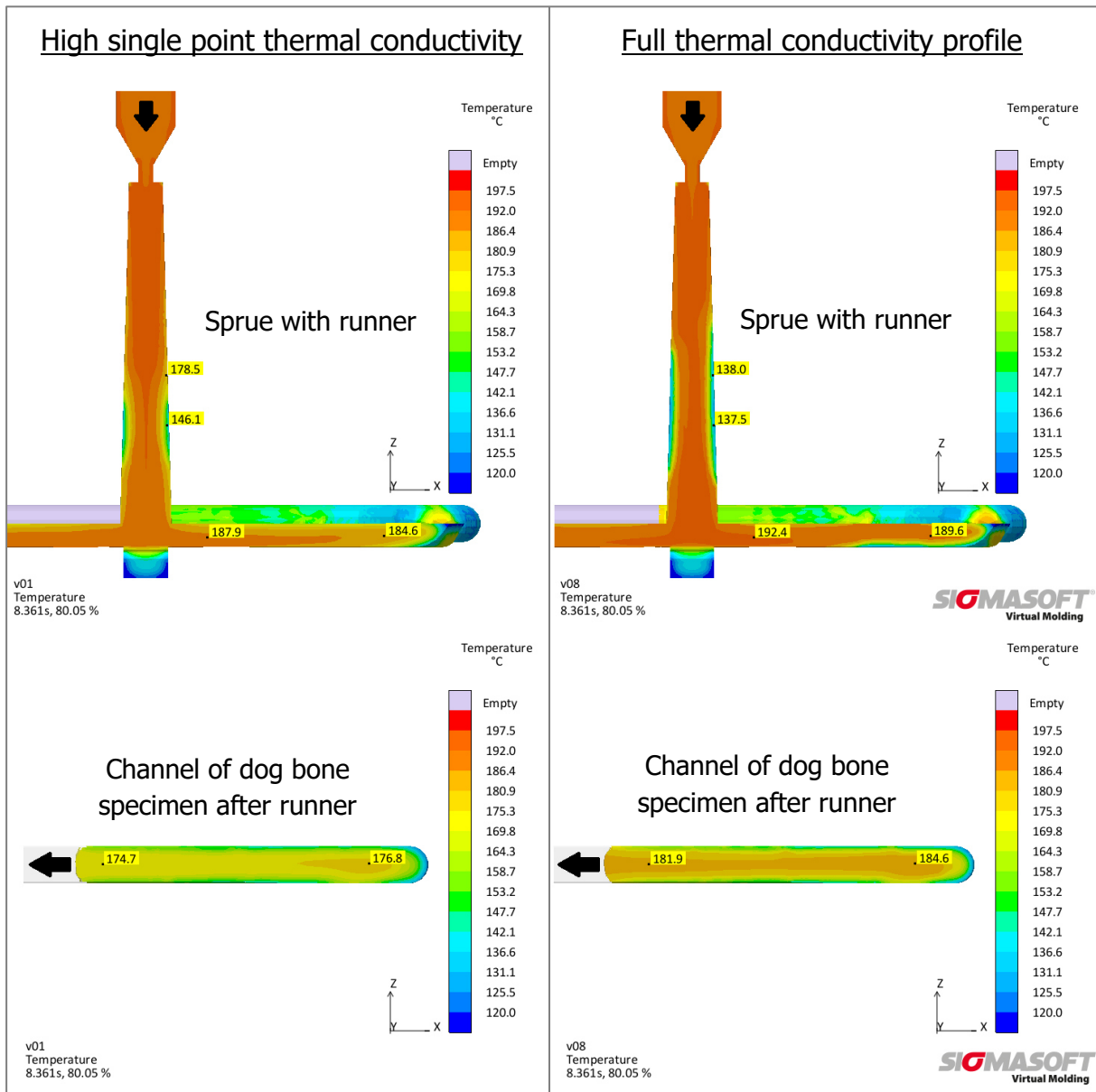


Figure 35: Temperature of the PolyPOM FN0805 feedstock in the dog bone simulation with the high single point value for the thermal conductivity (left) and the full thermal conductivity profile (right) at 80 % degree of filling ( $T_{\text{Mold}} = 80\text{ °C}$ ,  $\dot{V} = 5\text{ cm}^3/\text{s}$ ).

## 5 Summary and outlook

Powder injection molding is a net-shape manufacturing process which combines powder metallurgy with plastic injection molding for the production of metal or ceramic parts. In contrast to the conventional injection molding process highly filled plastics are used. These so-called feedstocks consequently exhibit different material properties compared to unfilled plastics. Hence, special flow phenomena occur in powder injection molding which have been investigated. Due to the high thermal conductivity, high heat transfer and the low specific heat compared to unfilled plastics, the material will cool down very fast at the colder mold wall. Therefore, the hypothesis, that a certain threshold temperature exists in the injection molding process, where the material suddenly exhibits solid-like behavior, was set up and analyzed within this master thesis. This would result in the solid-phase jetting, described by Piccirillo and Lee [32] and furthermore in a different flow behavior in the mold. It was assumed, that above this threshold temperature the material would exhibit a conventional flow behavior like thermoplastics and below it would only be pushed through the channels like a solid. A further consequence would be a different pressure resistance during the flow. Whereas in a normal flow the resistance is due to shearing, below the threshold temperature the resistance would be due to solid friction at the wall. Especially the material close to the wall would reach this threshold temperature very fast and form a solid case which would slip at the wall.

In order to test this hypothesis, filling studies with two different part geometries and three different commercially available feedstocks were performed at different mold temperatures and two injection rates to visualize occurring flow phenomena. Additionally, the injection pressure in the machine nozzle was measured by a pressure sensor. No expected threshold temperature could be found with the filling studies at different mold temperatures. Although at low temperatures the material was clearly pushed through the channels/cavity as a solid, the change of the flow behavior with higher mold temperatures was more continuous. The occurring flow phenomenon that the material tends to keep its shape and at some point, there is a preceding material area, could not be avoided by higher mold temperatures and a higher injection rate (one material with the highest settings for the temperature and injection rate excluded). In other words, at an extension of the cross section of the cavity/channel, the material did not spread regularly over the full thickness or rather the full width. This phenomenon stands in high contrast to unfilled thermoplastics, which form a fountain flow and could be visualized with a standard polypropylene. Especially for the recommended mold temperatures, the phenomenon occurs which might lead to significant problems in complex components. However, the three tested feedstocks all exhibited the same flow behavior and the findings are applicable to every material. Furthermore, a higher injection rate shifted the continuous transition to lower mold temperatures.

The pressure decreased linearly with increasing mold temperature and no sudden changes due to an existing threshold temperature could be observed. This result is in accordance with the filling pattern and the same conclusions can be assumed. There is no sudden change in the flow behavior. Furthermore, the same influences of the mold temperature and the injection rate could be observed for the three different feedstocks and the two cavities. The mold temperature only significantly affected the pressure at high injections volumes. A higher

injection rate increased the pressure only at high mold temperatures, whereas at low mold temperatures the pressures between different injection rates were very similar.

The tested feedstocks were also characterized regarding the rheological and thermodynamical behavior to perform simulations with Sigmasoft for a comparison with the practical experiments. Based on the work of Hubmann [20] and pretests with Sigmasoft, the well-known Herschel-Bulkley extension in the Cross-WLF model for low shear rates was not used, as the effect was negligible. The flow behavior did not change in the simulation by different mold temperatures or injection rates and always the same filling behavior, comparable to the behavior of polypropylene, was predicted. Since this is completely different from reality, the simulation cannot be used to visualize the filling behavior or predict critical regions like weld lines. Furthermore, no simple model, which would reproduce the hypothesis by a provided threshold temperature, could be the solution, as the hypothesis was rebutted.

Every time the filling pressure in the simulation was underestimated and for the coldest mold temperature, the dog bone cavity could not even be fully filled with two materials, contrary to the experiments. The average deviation to the measured pressure was approximately 69 % with a maximum deviation of 91 %. This could be corrected to some degree by additional numerical parameters in Sigmasoft to manipulate the viscosity, which is only reverse engineering by trial.

Another way to correct the pressure might be the  $D_3$  value in K/bar from the Cross-WLF model for the viscosity curves. Since the no-flow temperature was based on the pVT diagram, the  $D_3$  value of the Cross-WLF model was automatically set to the same value as  $b_6$  in the Tait model. Although this is better than zero, which means the assumption of a pressure independent viscosity, this value might be too small. Additional measurements of the pressure dependence of the materials might be necessary for an evaluation.

Summarized the simulation of the injection molding process of feedstocks cannot predict the real filling behavior yet (with standard settings in the simulation software), as special flow phenomena occur due to the special material behavior. In consequence, also the pressure calculation of the simulation does not correspond well to reality. Another practical workaround could be a mold temperature higher than the melting temperature for the filling phase in a variotherm process, as one material showed a filling behavior like thermoplastics at the highest mold temperature and the fastest injection rate. After the filling phase, the mold needs to be rapidly cooled down to allow solidification of the feedstock. However, the calculated pressure will be far too low then, and the above discussed options (viscosity manipulation, higher  $D_3$  value) are needed to improve the results.

## 6 References

- [1] Agarwala M.K., Patterson B.R., Clark P.E.: Rheological behavior of powder injection molding model slurries, *Journal of Rheology* 36 (2), 1992, pp. 319–334
- [2] Ahn S., et al.: Integrated filling, packing and cooling CAE analysis of powder injection moulding parts, *Powder Metallurgy* 51 (4), 2008, pp. 318–326
- [3] Ahn S., et al.: Effect of powders and binders on material properties and molding parameters in iron and stainless steel powder injection molding process, *Powder Technology* 193 (2), 2009, pp. 162–169
- [4] Allende M., Kalyon D.M.: Assessment of particle-migration effects in pressure-driven viscometric flows, *Journal of Rheology* 44 (1), 2000, pp. 79–90
- [5] Atre S.V., et al.: Process simulation of powder injection moulding: identification of significant parameters during mould filling phase, *Powder Metallurgy* 50 (1), 2007, pp. 76–85
- [6] Autodesk® Moldflow: Suspension balance model, <http://help.autodesk.com/view/MFIA/2018/ENU/?guid=GUID-BB1D3AA2-5D2E-4C97-8174-33F9F11990AF> (Retrieved on: 31.03.2019)
- [7] Bingham E.C.: Fluidity and plasticity, by Eugene C. Bingham, International chemical series, McGraw-Hill Book Company, Inc, New York, 1922
- [8] Black W.B.: Wall slip and boundary effects in polymer shear flow, Dissertation at the University of Wisconsin-Madison, Madison, 2000
- [9] Dbouk T., et al.: Shear-induced particle migration: Predictions from experimental evaluation of the particle stress tensor, *Journal of Non-Newtonian Fluid Mechanics* 198, 2013, pp. 78–95
- [10] Demers V., Turenne S., Scalzo O.: Segregation measurement of powder injection molding feedstock using thermogravimetric analysis, pycnometer density and differential scanning calorimetry techniques, *Advanced Powder Technology* 26 (3), 2015, pp. 997–1004
- [11] Denn M.M.: Extrusion Instabilities and Wall Slip, *Annual Review of Fluid Mechanics* 33 (1), 2001, pp. 265–287
- [12] Duretek I., Holzer C.: Material Flow Data for Numerical Simulation of Powder Injection Molding, *Universal Journal of Materials Science* 5 (1), 2017, pp. 7–14
- [13] Dvorak P., Barriere T., Gelin J.C.: Jetting in metal injection moulding of 316L stainless steel, *Powder Metallurgy* 48 (3), 2005, pp. 254–260
- [14] Dvorak P., Barriere T., Gelin J.C.: Direct observation of mould cavity filling in ceramic injection moulding, *Journal of the European Ceramic Society* 28 (10), 2008, pp. 1923–1929

- [15] Franck A.: Understanding Rheology of Thermoplastic Polymers, AAN013, 2013, [http://www.tainstruments.com/pdf/literature/AAN013\\_V\\_1\\_U\\_Thermoplast.pdf](http://www.tainstruments.com/pdf/literature/AAN013_V_1_U_Thermoplast.pdf) (Retrieved on: 21.03.2019)
- [16] German R.M.: Injection molding of metals and ceramics, MPIF, Princeton, 1997
- [17] Gonzalez-Gutierrez J., Beulke G., Emri I.: Powder Injection Molding of Metal and Ceramic Parts, In: Wang J. (Ed.): Some Critical Issues for Injection Molding, InTech, 2012
- [18] Hatzikiriakos S.G.: Wall slip of molten polymers, *Progress in Polymer Science* 37 (4), 2012, pp. 624–643
- [19] He J., Lee S.S., Kalyon D.M.: Shear viscosity and wall slip behavior of dense suspensions of polydisperse particles, *Journal of Rheology* 63 (1), 2019, pp. 19–32
- [20] Hubmann M.: Experimental validation of powder injection molding simulation with Autodesk Moldflow Insight 2018, Bachelor thesis at the Montanuniversität Leoben, Leoben, 2018
- [21] Kalyon D.M.: Apparent slip and viscoplasticity of concentrated suspensions, *Journal of Rheology* 49 (3), 2005, pp. 621–640
- [22] Kalyon D.M., Aktaş S.: Factors affecting the rheology and processability of highly filled suspensions, *Annual review of chemical and biomolecular engineering* 5, 2014, pp. 229–254
- [23] Keshavarz Panahi A., et al.: Optimization of the Powder Injection Molding Process Parameters Using the Sequential Simplex Algorithm and Sensitivity Analysis, *Journal of Manufacturing Science and Engineering* 135 (1), 2013, pp. 11006
- [24] Kim J.M., Lee S.G., Kim C.: Numerical simulations of particle migration in suspension flows: Frame-invariant formulation of curvature-induced migration, *Journal of Non-Newtonian Fluid Mechanics* 150 (2-3), 2008, pp. 162–176
- [25] Krauss V.A., et al.: Rheological properties of alumina injection feedstocks, *Materials Research* 8 (2), 2005, pp. 187–189
- [26] Krug S., Evans J.R.G., ter Maat J.H.H.: Jetting and weld lines in ceramic injection moulding, *British Ceramic Transactions* 98 (4), 1999, pp. 178–181
- [27] Kukla C., et al.: Rheology of PIM feedstocks, *Metal Powder Report* 72 (1), 2017, pp. 39–44
- [28] Lam Y.C., et al.: Wall slip of concentrated suspension melts in capillary flows, *Powder Technology* 177 (3), 2007, pp. 162–169
- [29] Moldex3D: Mathematical Models and Assumptions, [http://support.moldex3d.com/r16/en/solutionadd-ons\\_powderinjectionmolding\\_reference\\_mathematicalmodelsandassumptions.html](http://support.moldex3d.com/r16/en/solutionadd-ons_powderinjectionmolding_reference_mathematicalmodelsandassumptions.html) (Retrieved on: 31.03.2019)
- [30] Park D.Y., et al.: An experimental approach to powder-binder separation of feedstock, *Powder Technology* 306, 2017, pp. 34–44

- [31] Phillips R.J., et al.: A constitutive equation for concentrated suspensions that accounts for shear - induced particle migration, *Physics of Fluids A: Fluid Dynamics* 4 (1), 1992, pp. 30 – 40
- [32] Piccirillo N., Lee D.: Jetting phenomena in powder injection molding, *Int. J. Powder Metall.* 28, 1992
- [33] Piotter V., et al.: Powder injection moulding of metallic and ceramic micro parts, *Microsystem Technologies* 17 (2), 2011, pp. 251–263
- [34] PolyMIM GmbH: Data sheet - polyMIM® 17-4PH (80006), 2015
- [35] PolyMIM GmbH: Data sheet - polyPOM® FN0805 (80351), 2018
- [36] PolyMIM GmbH: Data sheet - polyPOM® 316L (80429), 2018
- [37] Rudolph N., Osswald T.: *Polymer rheology, Fundamentals and Applications*, Carl Hanser Verlag, München, 2015
- [38] Rueda M.M., et al.: Rheology and applications of highly filled polymers: A review of current understanding, *Progress in Polymer Science* 66, 2017, pp. 22–53
- [39] Samanta S.K., Chattopadhyay H., Godkhindi M.M.: Thermo-physical characterization of binder and feedstock for single and multiphase flow of PIM 316L feedstock, *Journal of Materials Processing Technology* 211 (12), 2011, pp. 2114–2122
- [40] Sardarian M., Mirzaee O., Habibolahzadeh A.: Numerical simulation and experimental investigation on jetting phenomenon in low pressure injection molding (LPIM) of alumina, *Journal of Materials Processing Technology* 243, 2017, pp. 374–380
- [41] Shivashankar T.S., et al.: The effects of material attributes on powder–binder separation phenomena in powder injection molding, *Powder Technology* 243, 2013, pp. 79–84
- [42] SIGMA Engineering GmbH: SIGMASOFT® 5.2.1 Help
- [43] Soltani F., Yilmazer Ü.: Slip velocity and slip layer thickness in flow of concentrated suspensions, *Journal of Applied Polymer Science* 70, 1998
- [44] Thornagel M.: Simulating flow can help avoid mould mistakes, 2010, <https://www.materialstoday.com/molding-and-pressing/features/simulating-flow-can-help-avoid-mould-mistakes/> (Retrieved on: 31.03.2019)
- [45] Thornagel M.: Injection moulding simulation: New developments offer rewards for the PIM industry, *powder injection moulding international* (Vol. 6 No. 1), 2012, 65-68
- [46] Vand V.: Viscosity of Solutions and Suspensions. I. Theory, *The Journal of Physical and Colloid Chemistry* 52 (2), 1948, pp. 277–299
- [47] Weber O., et al.: Micropowder injection molding: investigation of powder-binder separation using synchrotron-based microtomography and 3D image analysis, *Journal of Materials Science* 46 (10), 2011, pp. 3568–3573
- [48] Williams B.: WORLDPM2018 Congress: Global MIM markets show healthy growth, *powder injection moulding international* (Vol. 12 No. 4), 2018, pp. 67–75

## 6 References

- [49] Yang S., et al.: Analysis of Powder Binder Separation through Multiscale Computed Tomography, *Metals* 9 (3), 2019, pp. 329
- [50] Yang S., Zhang R., Qu X.: X-ray tomographic analysis of powder-binder separation in SiC green body, *Journal of the European Ceramic Society* 33 (15-16), 2013, pp. 2935–2941
- [51] Yang S., Zhang R., Qu X.: X-ray analysis of powder-binder separation during SiC injection process in L-shaped mould, *Journal of the European Ceramic Society* 35 (1), 2015, pp. 61–67
- [52] Yilmazer U., Kalyon D.M.: Slip Effects in Capillary and Parallel Disk Torsional Flows of Highly Filled Suspensions, *Journal of Rheology* 33 (8), 1989, pp. 1197–1212



## 7 List of tables and figures

### 7.1 Tables

TABLE 1:	TYPICAL COMPOSITION OF THE POWDERS AS SINTERED IN WT.% [34 - 36].....	15
TABLE 2:	SETTING FOR MANUFACTURING SPECIMENS FOR THERMAL CONDUCTIVITY MEASUREMENTS.	16
TABLE 3:	USED TEMPERATURES FOR THE THERMAL CONDUCTIVITY MEASUREMENTS. ....	16
TABLE 4:	CONSTANT INJECTION MOLDING MACHINE SETTINGS. ....	19
TABLE 5:	EXPERIMENTAL PLAN FOR FILLING STUDIES ON INJECTION MOLDING MACHINE.....	20
TABLE 6:	LIST OF THE GEOMETRY COMPONENTS WITH THE USED PROPERTIES AND THE MESH PARAMETERS. ....	21
TABLE 7:	MESH PARAMETERS FOR THE DIFFERENT MESH SETTINGS.....	22
TABLE 8:	GENERAL SETTINGS FOR THE SIMULATION IN SIGMASOFT V5.2. ....	23
TABLE 9:	COEFFICIENTS FOR THE CROSS-WLF VISCOSITY MODEL.....	24
TABLE 10:	COEFFICIENTS FOR THE TAIT PV <sub>T</sub> MODEL.....	24
TABLE 11:	RESULTS OF THE TGA ANALYSIS WITH VALUES FOR SIGMASOFT. ....	26
TABLE 12:	THERMAL CONDUCTIVITY VALUES FOR THE SIMULATION WITH SIGMASOFT. ....	27
TABLE 13:	USED $c_p$ VALUES FOR THE SIMULATION REDUCED BY SIGMASOFT. ....	63

### 7.2 Figures

FIGURE 1:	SCHEMATIC PRINCIPLE OF THE PIM PROCESS (ACCORDING TO [17]).....	2
FIGURE 2:	RELATIVE VISCOSITY $H_M/H_B$ IN DEPENDENCE OF THE SOLIDS LOADING (ACCORDING TO [17]). .....	4
FIGURE 3:	SCHEMATIC CORRELATION OF SHEAR RATE AND VISCOSITY OF UNFILLED THERMOPLASTICS (GREEN) AND FEEDSTOCKS (BLUE) (ACCORDING TO [12]). ....	6
FIGURE 4:	SCHEMATIC CORRELATION OF SHEAR RATE AND SHEAR STRESS OF UNFILLED THERMOPLASTICS (GREEN) AND FEEDSTOCKS (BLUE) (ACCORDING TO [37]). ....	6
FIGURE 5:	FLOW ALONG THE CAVITY WITH THE FORMATION OF A FROZEN LAYER ALONG THE WALL (ACCORDING TO [16]). ....	7
FIGURE 6:	COMPARISON OF THE DIFFERENT FLOW PROFILES OF (A) UNFILLED THERMOPLASTICS AND (B) FEEDSTOCKS (ACCORDING TO [45]). ....	7
FIGURE 7:	SCHEMATIC OF THE TWO PRINCIPAL MECHANISMS FOR SLIP, WHERE THE MACROMOLECULE (RED LINE) IN (A) DESORBS FROM THE WALL OR IN (B) DISENTANGLES FROM THE MACROMOLECULE IN THE BULK (ACCORDING TO [8]). ....	9
FIGURE 8:	SCHEMATIC REPRESENTATION OF THE APPARENT SLIP FLOW IN CAPILLARY (OR RECTANGULAR) DIES (ACCORDING TO [22]). ....	11
FIGURE 9:	SCHEMATIC VELOCITY PROFILE OF NEWTONIAN FLUIDS FOR SIMPLE SHEARING, WHERE THE BOTTOM PLANE IS FIXED AND THE UPPER PLANE IS MOVING. ....	11
FIGURE 10:	SCHEMATIC SKETCH OF THE TWO TYPES OF JETTING: A) CONVENTIONAL JETTING AND B) SOLID-PHASE JETTING. ....	12
FIGURE 11:	SCHEMATICALLY DRAWN JETTING PHENOMENON OBSERVED BY HUBMANN [20]. ....	13
FIGURE 12:	POWDER-BINDER SEPARATION DUE TO SHEAR RATE GRADIENTS AND TRANSPORT OF THE OCCURRING SEPARATION PATTERN [44]. ....	14

FIGURE 13: MEASURING POINTS FOR THE PRESSURE SENSOR CALIBRATION APPROXIMATED BY A QUADRATIC FUNCTION. ....	18
FIGURE 14: NUMBERED GEOMETRY COMPONENTS WITH BOUNDARIES FOR THE SIMULATION. ....	21
FIGURE 15: SPECIFIC HEAT OF THE THREE FEEDSTOCKS WITH A COOLING RATE OF 20 K/MIN. ....	26
FIGURE 16: FILLING STUDIES OF TENSILE SPECIMENS OF POLYPOM FN0805 (A-C) AND PP (D) FOR AN INJECTION RATE OF 5 CM <sup>3</sup> /S IN SIX STEPS WHERE (A): EXPERIMENTAL FOR T <sub>MOLD</sub> = 80 °C; (B) EXPERIMENTAL FOR T <sub>MOLD</sub> = 150 °C; (C) SIMULATION FOR T <sub>MOLD</sub> = 80 °C; (D) EXPERIMENTAL FOR T <sub>MOLD</sub> = 30 °C. ....	28
FIGURE 17: FILLING STUDIES OF DOG BONE SPECIMENS OF POLYPOM FN0805 (A-C) AND PP (D) FOR AN INJECTION RATE OF 5 CM <sup>3</sup> /S IN FIVE STEPS WHERE (A): EXPERIMENTAL FOR T <sub>MOLD</sub> = 80 °C; (B) EXPERIMENTAL FOR T <sub>MOLD</sub> = 150 °C; (C) SIMULATION FOR T <sub>MOLD</sub> = 80 °C; (D) EXPERIMENTAL FOR T <sub>MOLD</sub> = 30 °C. ....	29
FIGURE 18: STEP 2 OF THE FILLING STUDY OF POLYPOM FN0805 TENSILE SPECIMENS AT AN INJECTION RATE OF 5 CM <sup>3</sup> /S AT DIFFERENT MOLD TEMPERATURES. ....	30
FIGURE 19: STEP 3 OF THE FILLING STUDY OF POLYPOM FN0805 TENSILE SPECIMENS AT AN INJECTION RATE OF 5 CM <sup>3</sup> /S AT DIFFERENT MOLD TEMPERATURES. ....	31
FIGURE 20: TENSILE SPECIMENS OF STEP 3 OF THE FILLING STUDY AT 100 °C AND 150 °C MOLD TEMPERATURE OF POLYPOM FN0805 AT AN INJECTION RATE OF 5 CM <sup>3</sup> /S. ....	31
FIGURE 21: STEP 4 OF THE FILLING STUDY OF POLYPOM FN0805 TENSILE SPECIMENS AT AN INJECTION RATE OF 5 CM <sup>3</sup> /S AT DIFFERENT MOLD TEMPERATURES. ....	32
FIGURE 22: STEP 5 OF THE FILLING STUDY OF POLYPOM FN0805 TENSILE SPECIMENS AT AN INJECTION RATE OF 5 CM <sup>3</sup> /S AT DIFFERENT MOLD TEMPERATURES. ....	32
FIGURE 23: STEP 6 OF THE FILLING STUDY OF POLYPOM FN0805 TENSILE SPECIMENS AT AN INJECTION RATE OF 5 CM <sup>3</sup> /S AT DIFFERENT MOLD TEMPERATURES. ....	33
FIGURE 24: FILLING STUDY OF TENSILE SPECIMENS OF POLYPOM FN0805 AT T <sub>MOLD</sub> = 80 °C FOR AN INJECTION RATE OF (A) 5 CM <sup>3</sup> /S AND (B) 20 CM <sup>3</sup> /S. ....	34
FIGURE 25: SEPARATING OF A SURFACE LAYER IN THE FILLING PROCESS OF POLYPOM 316L DOG BONE SPECIMENS AT HIGHER MOLD TEMPERATURES (150 °C), WHERE (A) IS STEP 4 AND (B) IS STEP 5 OF THE FILLING STUDY FOR AN INJECTION RATE OF 20 CM <sup>3</sup> /S. ....	34
FIGURE 26: INJECTION PRESSURES OF THE TENSILE SPECIMENS FOR ALL THREE MATERIALS IN DEPENDENCE OF THE MOLD TEMPERATURE WITH LINEAR APPROXIMATIONS FOR ALL USED INJECTION VOLUMES (VOL) AND FOR AN INJECTION RATE OF 5 CM <sup>3</sup> /S. ....	36
FIGURE 27: INJECTION PRESSURES OF THE TENSILE SPECIMENS FOR ALL THREE MATERIALS IN DEPENDENCE OF THE MOLD TEMPERATURE WITH LINEAR APPROXIMATIONS FOR ALL USED INJECTION VOLUMES (VOL) AND FOR AN INJECTION RATE OF 20 CM <sup>3</sup> /S. ....	37
FIGURE 28: INJECTION PRESSURES OF THE POLYPOM FN0805 TENSILE SPECIMENS IN DEPENDENCE OF THE MOLD TEMPERATURE WITH LINEAR APPROXIMATIONS FOR ALL USED INJECTION VOLUMES (VOL) AND BOTH INJECTION RATES. ....	38
FIGURE 29: INJECTION PRESSURES OF THE TENSILE SPECIMENS FOR ALL THREE MATERIALS IN DEPENDENCE OF THE INJECTION RATE AT FILLING STEP 1. ....	39
FIGURE 30: INJECTION PRESSURES OF THE TENSILE SPECIMENS FOR ALL THREE MATERIALS IN DEPENDENCE OF THE INJECTION RATE AT FILLING STEP 5 (POLYPOM 316L) AND FILLING STEP 6 (POLYPOM FN0805 AND POLYMIM 17-4PH). ....	40
FIGURE 31: EXPERIMENTAL AND SIMULATION RESULTS OF THE INJECTION PRESSURE OVER TIME FOR POLYPOM FN0805 WITH V = 5 CM <sup>3</sup> /S AND T <sub>MOLD</sub> = 80 °C. ....	41

## 7 List of tables and figures

FIGURE 32: EXPERIMENTAL AND SIMULATION RESULTS OF THE INJECTION PRESSURE OVER TIME FOR POLYPOM FN0805 WITH $V = 5 \text{ cm}^3/\text{s}$ AND $T_{\text{MOLD}} = 150 \text{ }^\circ\text{C}$ .....	42
FIGURE 33: PRESSURE DIFFERENCE BETWEEN THE VALUES OF THE EXPERIMENT AND THE SIMULATION IN % REFERRED TO THE MEASURED PRESSURE FROM THE EXPERIMENT.....	43
FIGURE 34: INJECTION PRESSURE OF THE SIMULATION OF BOTH CAVITIES WITH POLYPOM FN0805 WITH THE HIGH SINGLE POINT VALUE FOR THE THERMAL CONDUCTIVITY (BLUE) AND THE FULL THERMAL CONDUCTIVITY PROFILE (RED) ( $T_{\text{MOLD}} = 80 \text{ }^\circ\text{C}$ , $V = 5 \text{ cm}^3/\text{s}$ ). ....	44
FIGURE 35: TEMPERATURE OF THE POLYPOM FN0805 FEEDSTOCK IN THE DOG BONE SIMULATION WITH THE HIGH SINGLE POINT VALUE FOR THE THERMAL CONDUCTIVITY (LEFT) AND THE FULL THERMAL CONDUCTIVITY PROFILE (RIGHT) AT 80 % DEGREE OF FILLING ( $T_{\text{MOLD}} = 80 \text{ }^\circ\text{C}$ , $V = 5 \text{ cm}^3/\text{s}$ ). ....	45
FIGURE 36: DRAWINGS WITH THE MOST IMPORTANT DIMENSIONS OF THE USED MOLD (A) AND THE TWO COOLING CHANNELS (B).....	59
FIGURE 37: DRAWING OF THE CAVITY OF THE MULTI-PURPOSE (OR TENSILE) SPECIMEN WITH ONE CAVITY SEALED. ....	60
FIGURE 38: DRAWING OF ONE CAVITY OF THE ROUND DOG BONE SPECIMEN WITHOUT RUNNER SYSTEM.	60
FIGURE 39: DRAWING OF THE NOZZLE UP TO THE PRESSURE SENSOR.....	61
FIGURE 40: APPROXIMATED CROSS-WLF CURVES WITH MEASURING POINTS FOR POLYPOM FN0805..	61
FIGURE 41: APPROXIMATED CROSS-WLF CURVES WITH MEASURING POINTS FOR POLYPOM 316L. ....	62
FIGURE 42: APPROXIMATED CROSS-WLF CURVES WITH MEASURING POINTS FOR POLYMIM 17-4PH...	62
FIGURE 43: AREA OF FRACTURE OF A POLYPOM FN0805 SPECIMEN WITH MAGNIFICATION OF 1000 TIMES UNDER AN SEM. ....	64
FIGURE 44: TGA REST OF A POLYPOM 316L SPECIMEN WITH MAGNIFICATION OF 1000 TIMES UNDER AN SEM. ....	64
FIGURE 45: TGA REST OF A POLYMIM 17-4PH SPECIMEN WITH MAGNIFICATION OF 1000 TIMES UNDER AN SEM. ....	65
FIGURE 46: MEASURED THERMAL CONDUCTIVITY VALUES USED FOR THE SIMULATION. ....	65
FIGURE 47: INJECTION PRESSURES OF THE DOG BONE SPECIMENS FOR ALL THREE MATERIALS IN DEPENDENCE OF THE MOLD TEMPERATURE WITH LINEAR APPROXIMATIONS FOR ALL USED INJECTION VOLUMES (VOL) AND FOR AN INJECTION RATE OF $5 \text{ cm}^3/\text{s}$ .....	66
FIGURE 48: INJECTION PRESSURES OF THE DOG BONE SPECIMENS FOR ALL THREE MATERIALS IN DEPENDENCE OF THE MOLD TEMPERATURE WITH LINEAR APPROXIMATIONS FOR ALL USED INJECTION VOLUMES (VOL) AND FOR AN INJECTION RATE OF $20 \text{ cm}^3/\text{s}$ . ....	67
FIGURE 49: STEP 2 OF THE FILLING STUDY OF POLYPOM FN0805 TENSILE SPECIMENS AT AN INJECTION RATE OF $20 \text{ cm}^3/\text{s}$ AT DIFFERENT MOLD TEMPERATURES.....	68
FIGURE 50: STEP 3 OF THE FILLING STUDY OF POLYPOM FN0805 TENSILE SPECIMENS AT AN INJECTION RATE OF $20 \text{ cm}^3/\text{s}$ AT DIFFERENT MOLD TEMPERATURES.....	68
FIGURE 51: STEP 4 OF THE FILLING STUDY OF POLYPOM FN0805 TENSILE SPECIMENS AT AN INJECTION RATE OF $20 \text{ cm}^3/\text{s}$ AT DIFFERENT MOLD TEMPERATURES.....	68
FIGURE 52: STEP 5 OF THE FILLING STUDY OF POLYPOM FN0805 TENSILE SPECIMENS AT AN INJECTION RATE OF $20 \text{ cm}^3/\text{s}$ AT DIFFERENT MOLD TEMPERATURES.....	69
FIGURE 53: STEP 6 OF THE FILLING STUDY OF POLYPOM FN0805 TENSILE SPECIMENS AT AN INJECTION RATE OF $20 \text{ cm}^3/\text{s}$ AT DIFFERENT MOLD TEMPERATURES.....	69
FIGURE 54: STEP 1 OF THE FILLING STUDY OF POLYPOM FN0805 DOG BONE SPECIMENS AT AN INJECTION RATE OF $5 \text{ cm}^3/\text{s}$ AT DIFFERENT MOLD TEMPERATURES. ....	70

## 7 List of tables and figures

FIGURE 55: STEP 2 OF THE FILLING STUDY OF POLYPOM FN0805 DOG BONE SPECIMENS AT AN INJECTION RATE OF 5 CM <sup>3</sup> /S AT DIFFERENT MOLD TEMPERATURES. ....	70
FIGURE 56: STEP 3 OF THE FILLING STUDY OF POLYPOM FN0805 DOG BONE SPECIMENS AT AN INJECTION RATE OF 5 CM <sup>3</sup> /S AT DIFFERENT MOLD TEMPERATURES. ....	70
FIGURE 57: STEP 4 OF THE FILLING STUDY OF POLYPOM FN0805 DOG BONE SPECIMENS AT AN INJECTION RATE OF 5 CM <sup>3</sup> /S AT DIFFERENT MOLD TEMPERATURES. ....	71
FIGURE 58: STEP 5 OF THE FILLING STUDY OF POLYPOM FN0805 DOG BONE SPECIMENS AT AN INJECTION RATE OF 5 CM <sup>3</sup> /S AT DIFFERENT MOLD TEMPERATURES. ....	71
FIGURE 59: STEP 1 OF THE FILLING STUDY OF POLYPOM FN0805 DOG BONE SPECIMENS AT AN INJECTION RATE OF 20 CM <sup>3</sup> /S AT DIFFERENT MOLD TEMPERATURES.....	72
FIGURE 60: STEP 2 OF THE FILLING STUDY OF POLYPOM FN0805 DOG BONE SPECIMENS AT AN INJECTION RATE OF 20 CM <sup>3</sup> /S AT DIFFERENT MOLD TEMPERATURES.....	72
FIGURE 61: STEP 3 OF THE FILLING STUDY OF POLYPOM FN0805 DOG BONE SPECIMENS AT AN INJECTION RATE OF 20 CM <sup>3</sup> /S AT DIFFERENT MOLD TEMPERATURES.....	72
FIGURE 62: STEP 4 OF THE FILLING STUDY OF POLYPOM FN0805 DOG BONE SPECIMENS AT AN INJECTION RATE OF 20 CM <sup>3</sup> /S AT DIFFERENT MOLD TEMPERATURES.....	73
FIGURE 63: STEP 5 OF THE FILLING STUDY OF POLYPOM FN0805 DOG BONE SPECIMENS AT AN INJECTION RATE OF 20 CM <sup>3</sup> /S AT DIFFERENT MOLD TEMPERATURES.....	73
FIGURE 64: STEP 2 OF THE FILLING STUDY OF POLYPOM 316L TENSILE SPECIMENS AT AN INJECTION RATE OF 5 CM <sup>3</sup> /S AT DIFFERENT MOLD TEMPERATURES. ....	74
FIGURE 65: STEP 3 OF THE FILLING STUDY OF POLYPOM 316L TENSILE SPECIMENS AT AN INJECTION RATE OF 5 CM <sup>3</sup> /S AT DIFFERENT MOLD TEMPERATURES. ....	74
FIGURE 66: STEP 4 OF THE FILLING STUDY OF POLYPOM 316L TENSILE SPECIMENS AT AN INJECTION RATE OF 5 CM <sup>3</sup> /S AT DIFFERENT MOLD TEMPERATURES. ....	75
FIGURE 67: STEP 5 OF THE FILLING STUDY OF POLYPOM 316L TENSILE SPECIMENS AT AN INJECTION RATE OF 5 CM <sup>3</sup> /S AT DIFFERENT MOLD TEMPERATURES. ....	75
FIGURE 68: STEP 6 OF THE FILLING STUDY OF POLYPOM 316L TENSILE SPECIMENS AT AN INJECTION RATE OF 5 CM <sup>3</sup> /S AT DIFFERENT MOLD TEMPERATURES. ....	76
FIGURE 69: STEP 2 OF THE FILLING STUDY OF POLYPOM 316L TENSILE SPECIMENS AT AN INJECTION RATE OF 20 CM <sup>3</sup> /S AT DIFFERENT MOLD TEMPERATURES.....	76
FIGURE 70: STEP 3 OF THE FILLING STUDY OF POLYPOM 316L TENSILE SPECIMENS AT AN INJECTION RATE OF 20 CM <sup>3</sup> /S AT DIFFERENT MOLD TEMPERATURES.....	77
FIGURE 71: STEP 4 OF THE FILLING STUDY OF POLYPOM 316L TENSILE SPECIMENS AT AN INJECTION RATE OF 20 CM <sup>3</sup> /S AT DIFFERENT MOLD TEMPERATURES.....	77
FIGURE 72: STEP 5 OF THE FILLING STUDY OF POLYPOM 316L TENSILE SPECIMENS AT AN INJECTION RATE OF 20 CM <sup>3</sup> /S AT DIFFERENT MOLD TEMPERATURES.....	78
FIGURE 73: STEP 1 OF THE FILLING STUDY OF POLYPOM 316L DOG BONE SPECIMENS AT AN INJECTION RATE OF 5 CM <sup>3</sup> /S AT DIFFERENT MOLD TEMPERATURES. ....	78
FIGURE 74: STEP 2 OF THE FILLING STUDY OF POLYPOM 316L DOG BONE SPECIMENS AT AN INJECTION RATE OF 5 CM <sup>3</sup> /S AT DIFFERENT MOLD TEMPERATURES. ....	79
FIGURE 75: STEP 3 OF THE FILLING STUDY OF POLYPOM 316L DOG BONE SPECIMENS AT AN INJECTION RATE OF 5 CM <sup>3</sup> /S AT DIFFERENT MOLD TEMPERATURES. ....	79
FIGURE 76: STEP 4 OF THE FILLING STUDY OF POLYPOM 316L DOG BONE SPECIMENS AT AN INJECTION RATE OF 5 CM <sup>3</sup> /S AT DIFFERENT MOLD TEMPERATURES. ....	79

## 7 List of tables and figures

FIGURE 77: STEP 5 OF THE FILLING STUDY OF POLYPOM 316L DOG BONE SPECIMENS AT AN INJECTION RATE OF 5 CM <sup>3</sup> /S AT DIFFERENT MOLD TEMPERATURES. ....	80
FIGURE 78: STEP 1 OF THE FILLING STUDY OF POLYPOM 316L DOG BONE SPECIMENS AT AN INJECTION RATE OF 20 CM <sup>3</sup> /S AT DIFFERENT MOLD TEMPERATURES.....	80
FIGURE 79: STEP 2 OF THE FILLING STUDY OF POLYPOM 316L DOG BONE SPECIMENS AT AN INJECTION RATE OF 20 CM <sup>3</sup> /S AT DIFFERENT MOLD TEMPERATURES.....	80
FIGURE 80: STEP 3 OF THE FILLING STUDY OF POLYPOM 316L DOG BONE SPECIMENS AT AN INJECTION RATE OF 20 CM <sup>3</sup> /S AT DIFFERENT MOLD TEMPERATURES.....	81
FIGURE 81: STEP 4 OF THE FILLING STUDY OF POLYPOM 316L DOG BONE SPECIMENS AT AN INJECTION RATE OF 20 CM <sup>3</sup> /S AT DIFFERENT MOLD TEMPERATURES.....	81
FIGURE 82: STEP 5 OF THE FILLING STUDY OF POLYPOM 316L DOG BONE SPECIMENS AT AN INJECTION RATE OF 20 CM <sup>3</sup> /S AT DIFFERENT MOLD TEMPERATURES.....	81
FIGURE 83: STEP 2 OF THE FILLING STUDY OF POLYMIM 17-4PH TENSILE SPECIMENS AT AN INJECTION RATE OF 5 CM <sup>3</sup> /S AT DIFFERENT MOLD TEMPERATURES. ....	82
FIGURE 84: STEP 3 OF THE FILLING STUDY OF POLYMIM 17-4PH TENSILE SPECIMENS AT AN INJECTION RATE OF 5 CM <sup>3</sup> /S AT DIFFERENT MOLD TEMPERATURES. ....	82
FIGURE 85: STEP 4 OF THE FILLING STUDY OF POLYMIM 17-4PH TENSILE SPECIMENS AT AN INJECTION RATE OF 5 CM <sup>3</sup> /S AT DIFFERENT MOLD TEMPERATURES. ....	83
FIGURE 86: STEP 5 OF THE FILLING STUDY OF POLYMIM 17-4PH TENSILE SPECIMENS AT AN INJECTION RATE OF 5 CM <sup>3</sup> /S AT DIFFERENT MOLD TEMPERATURES. ....	83
FIGURE 87: STEP 6 OF THE FILLING STUDY OF POLYMIM 17-4PH TENSILE SPECIMENS AT AN INJECTION RATE OF 5 CM <sup>3</sup> /S AT DIFFERENT MOLD TEMPERATURES. ....	84
FIGURE 88: STEP 2 OF THE FILLING STUDY OF POLYMIM 17-4PH TENSILE SPECIMENS AT AN INJECTION RATE OF 20 CM <sup>3</sup> /S AT DIFFERENT MOLD TEMPERATURES.....	84
FIGURE 89: STEP 3 OF THE FILLING STUDY OF POLYMIM 17-4PH TENSILE SPECIMENS AT AN INJECTION RATE OF 20 CM <sup>3</sup> /S AT DIFFERENT MOLD TEMPERATURES.....	85
FIGURE 90: STEP 4 OF THE FILLING STUDY OF POLYMIM 17-4PH TENSILE SPECIMENS AT AN INJECTION RATE OF 20 CM <sup>3</sup> /S AT DIFFERENT MOLD TEMPERATURES.....	85
FIGURE 91: STEP 5 OF THE FILLING STUDY OF POLYMIM 17-4PH TENSILE SPECIMENS AT AN INJECTION RATE OF 20 CM <sup>3</sup> /S AT DIFFERENT MOLD TEMPERATURES.....	86
FIGURE 92: STEP 6 OF THE FILLING STUDY OF POLYMIM 17-4PH TENSILE SPECIMENS AT AN INJECTION RATE OF 20 CM <sup>3</sup> /S AT DIFFERENT MOLD TEMPERATURES.....	86
FIGURE 93: STEP 1 OF THE FILLING STUDY OF POLYMIM 17-4PH DOG BONE SPECIMENS AT AN INJECTION RATE OF 5 CM <sup>3</sup> /S AT DIFFERENT MOLD TEMPERATURES. ....	87
FIGURE 94: STEP 2 OF THE FILLING STUDY OF POLYMIM 17-4PH DOG BONE SPECIMENS AT AN INJECTION RATE OF 5 CM <sup>3</sup> /S AT DIFFERENT MOLD TEMPERATURES. ....	87
FIGURE 95: STEP 3 OF THE FILLING STUDY OF POLYMIM 17-4PH DOG BONE SPECIMENS AT AN INJECTION RATE OF 5 CM <sup>3</sup> /S AT DIFFERENT MOLD TEMPERATURES. ....	87
FIGURE 96: STEP 4 OF THE FILLING STUDY OF POLYMIM 17-4PH DOG BONE SPECIMENS AT AN INJECTION RATE OF 5 CM <sup>3</sup> /S AT DIFFERENT MOLD TEMPERATURES. ....	88
FIGURE 97: STEP 5 OF THE FILLING STUDY OF POLYMIM 17-4PH DOG BONE SPECIMENS AT AN INJECTION RATE OF 5 CM <sup>3</sup> /S AT DIFFERENT MOLD TEMPERATURES. ....	88
FIGURE 98: STEP 1 OF THE FILLING STUDY OF POLYMIM 17-4PH DOG BONE SPECIMENS AT AN INJECTION RATE OF 20 CM <sup>3</sup> /S AT DIFFERENT MOLD TEMPERATURES.....	88

FIGURE 99: STEP 2 OF THE FILLING STUDY OF POLYMIM 17-4PH DOG BONE SPECIMENS AT AN INJECTION RATE OF 20 CM<sup>3</sup>/S AT DIFFERENT MOLD TEMPERATURES..... 89

FIGURE 100: STEP 3 OF THE FILLING STUDY OF POLYMIM 17-4PH DOG BONE SPECIMENS AT AN INJECTION RATE OF 20 CM<sup>3</sup>/S AT DIFFERENT MOLD TEMPERATURES..... 89

FIGURE 101: STEP 4 OF THE FILLING STUDY OF POLYMIM 17-4PH DOG BONE SPECIMENS AT AN INJECTION RATE OF 20 CM<sup>3</sup>/S AT DIFFERENT MOLD TEMPERATURES..... 89

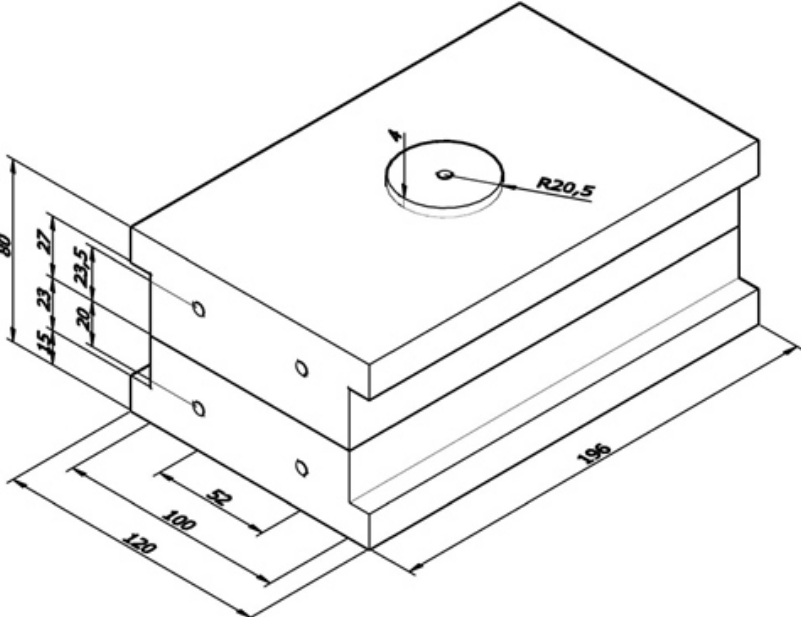
FIGURE 102: STEP 5 OF THE FILLING STUDY OF POLYMIM 17-4PH DOG BONE SPECIMENS AT AN INJECTION RATE OF 20 CM<sup>3</sup>/S AT DIFFERENT MOLD TEMPERATURES..... 90

## 8 Abbreviations

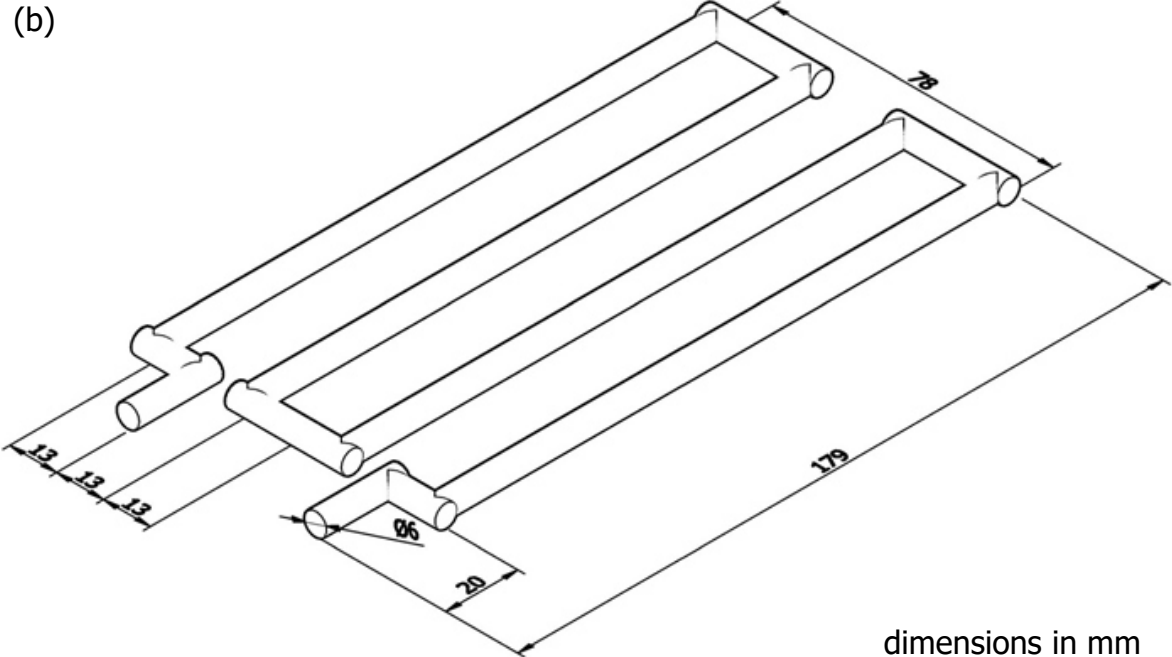
AISI	American Iron and Steel Institute
AMI	Autodesk Moldflow Insight
CAD	computer aided design
CIM	ceramic injection molding
CT	computed tomography
DSC	differential scanning calorimetry
EVA	ethylene vinyl acetate
LPIM	low pressure injection molding
MIM	metal injection molding
PD	pycnometer density
PE	polyethylene
PEG	polyethylene glycol
PIM	powder injection molding
PMMA	polymethyl methacrylate
POM	polyoxymethylene
PP	polypropylene
PS	polystyrene
SBM	suspension balance model
SEM	scanning electron microscope
S- $\mu$ CT	synchrotron-based microtomography
TC	temperature controlled
TGA	thermogravimetric analysis
Vol	volume
vol.%	volume percent
WLF	Williams–Landel–Ferry
wt.%	weight percent

# 9 Appendix

(a)



(b)



dimensions in mm

Figure 36: Drawings with the most important dimensions of the used mold (a) and the two cooling channels (b).



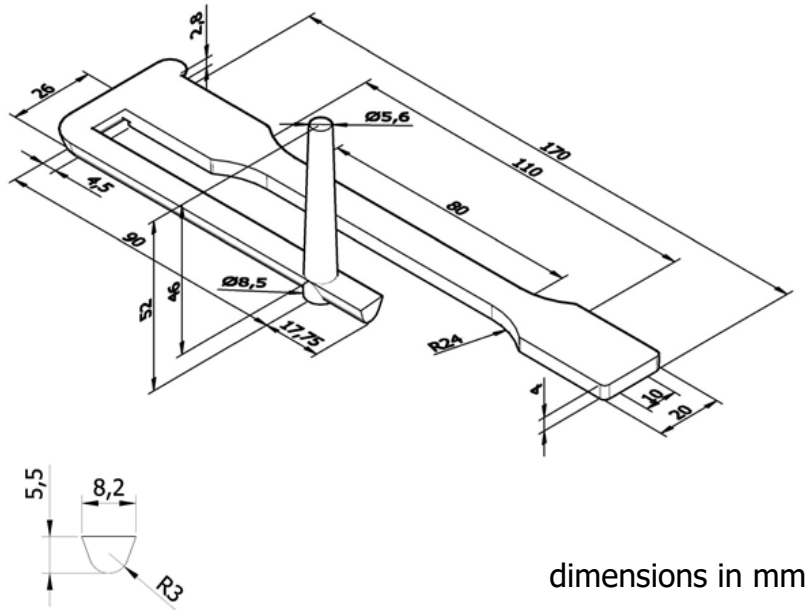


Figure 37: Drawing of the cavity of the multi-purpose (or tensile) specimen with one cavity sealed.

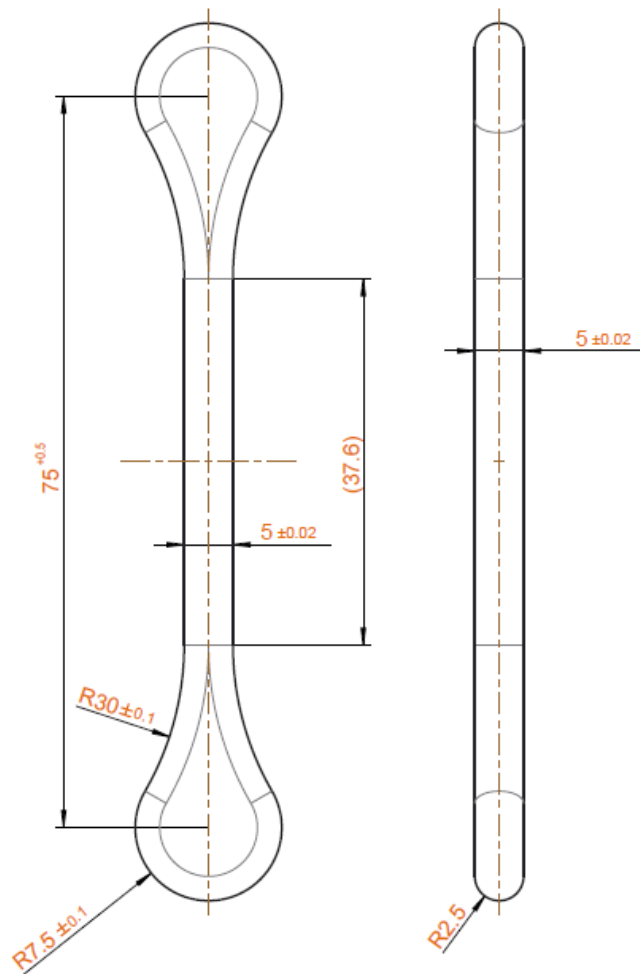


Figure 38: Drawing of one cavity of the round dog bone specimen without runner system.

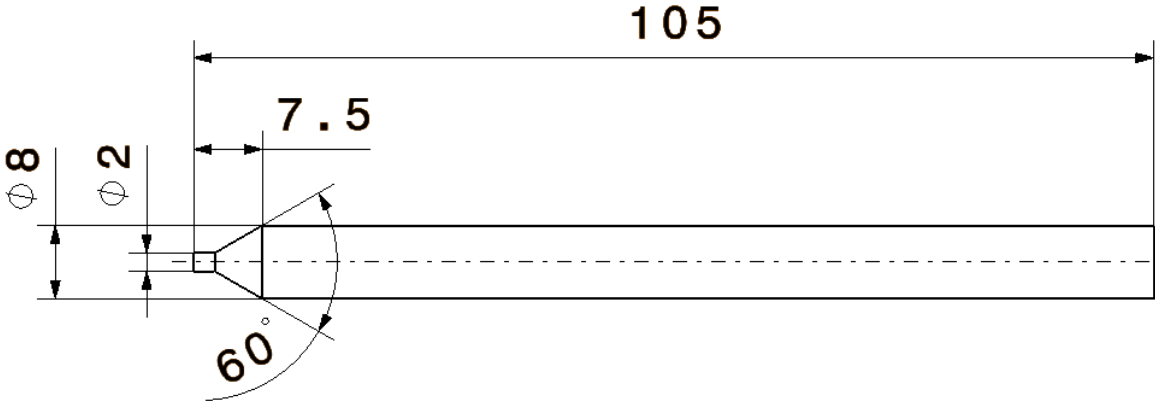


Figure 39: Drawing of the nozzle up to the pressure sensor.

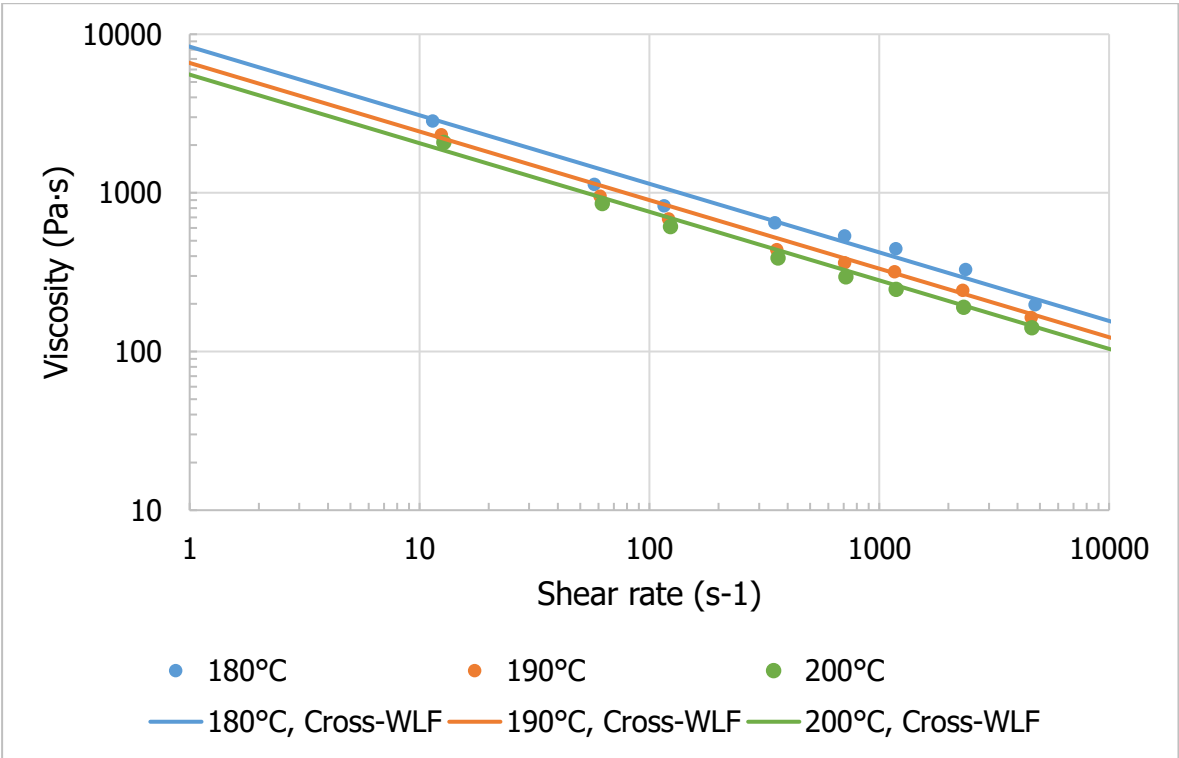


Figure 40: Approximated Cross-WLF curves with measuring points for PolyPOM FN0805.

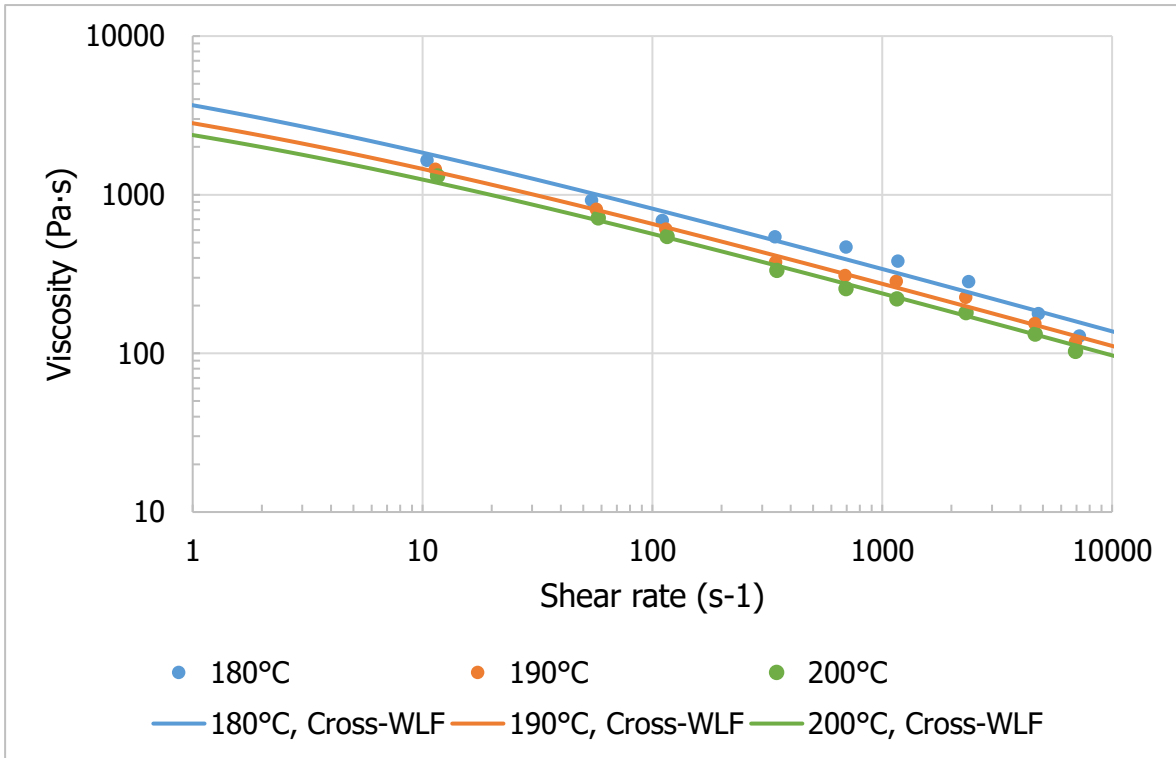


Figure 41: Approximated Cross-WLF curves with measuring points for PolyPOM 316L.

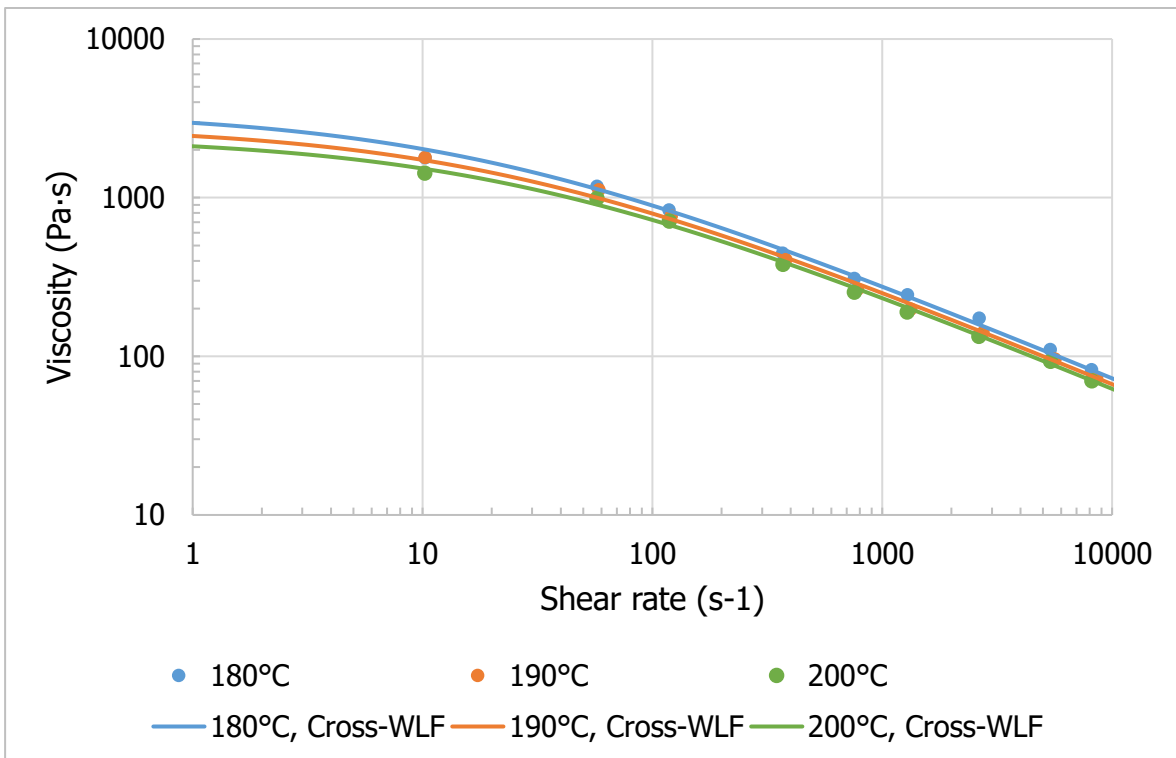


Figure 42: Approximated Cross-WLF curves with measuring points for PolyMIM 17-4PH.

Table 13: Used  $c_p$  values for the simulation reduced by Sigmasoft.

PolyPOM FN0805		PolyPOM 316L		PolyMIM 17-4PH D	
T (°C)	$c_p$ (J/kg·K)	T (°C)	$c_p$ (J/kg·K)	T (°C)	$c_p$ (J/kg·K)
0.9	517	0.9	532	0.8	538
56.4	588	67.1	605	20.2	560
79.8	647	83.8	647	23.5	572
95.8	659	99.8	656	26.9	606
107.9	712	109.9	707	28.2	634
121.9	732	118.5	691	30.3	709
125.9	792	125.2	715	31.6	788
129.4	931	129.3	764	35.1	1036
131.4	1120	132.6	884	35.8	1069
135.2	1589	134.7	1059	36.5	1091
136.8	1718	138.4	1507	37.9	1102
138.5	1764	139.2	1570	38.6	1095
139.3	1755	140.9	1631	40.5	1035
141.1	1644	142.5	1615	41.7	963
142.1	1508	144.3	1510	45.6	668
143.4	1208	145.2	1384	46.9	614
145.2	904	146.6	1096	48.9	590
146.6	762	147.9	899	69.0	618
148.6	679	149.2	752	83.6	605
200.0	705	149.9	707	95.7	621
		151.2	668	99.7	643
		179.3	679	106.4	707
		196.6	788	108.4	735
		200.1	829	113.1	823
				114.5	818
				117.8	771
				119.7	723
				123.0	623
				124.4	607
				128.4	592
				139.7	622
				143.7	615
				157.8	622
				200.1	645

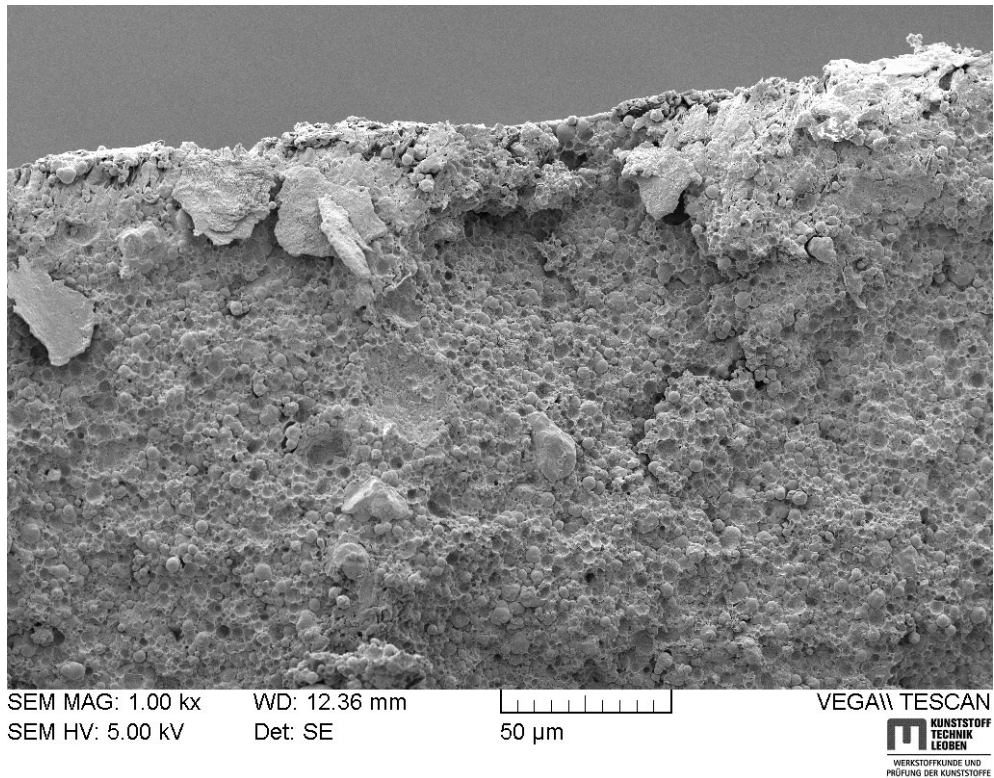


Figure 43: Area of fracture of a PolyPOM FN0805 specimen with magnification of 1000 times under an SEM.

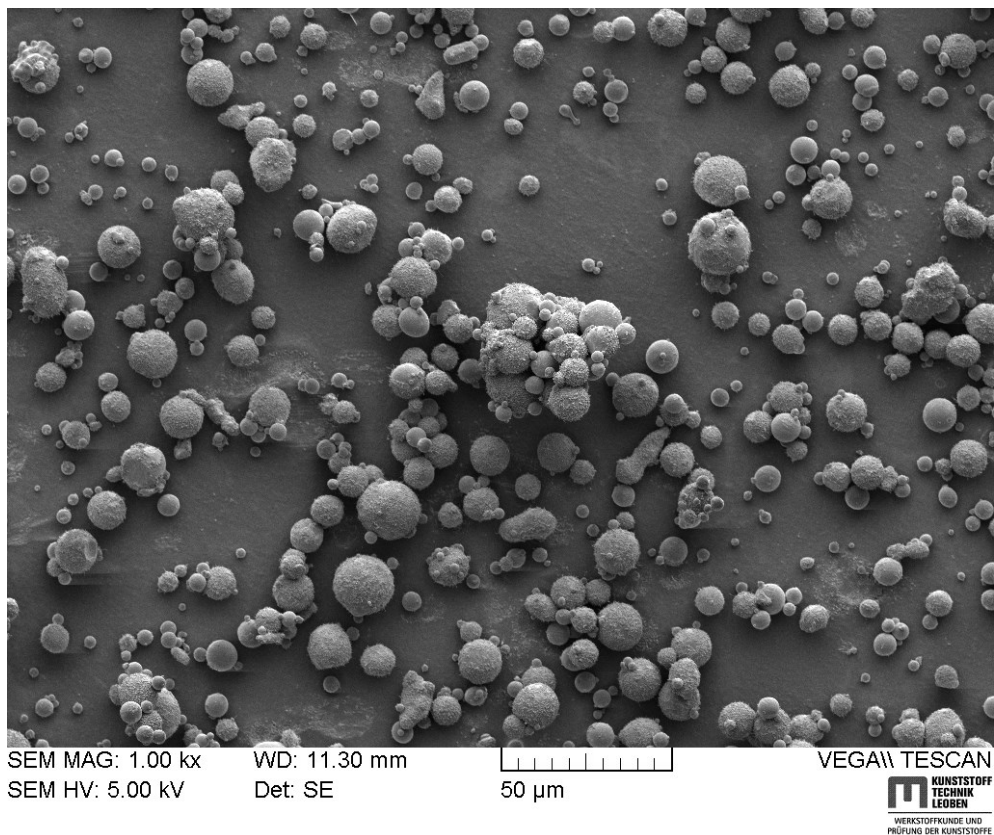


Figure 44: TGA rest of a PolyPOM 316L specimen with magnification of 1000 times under an SEM.

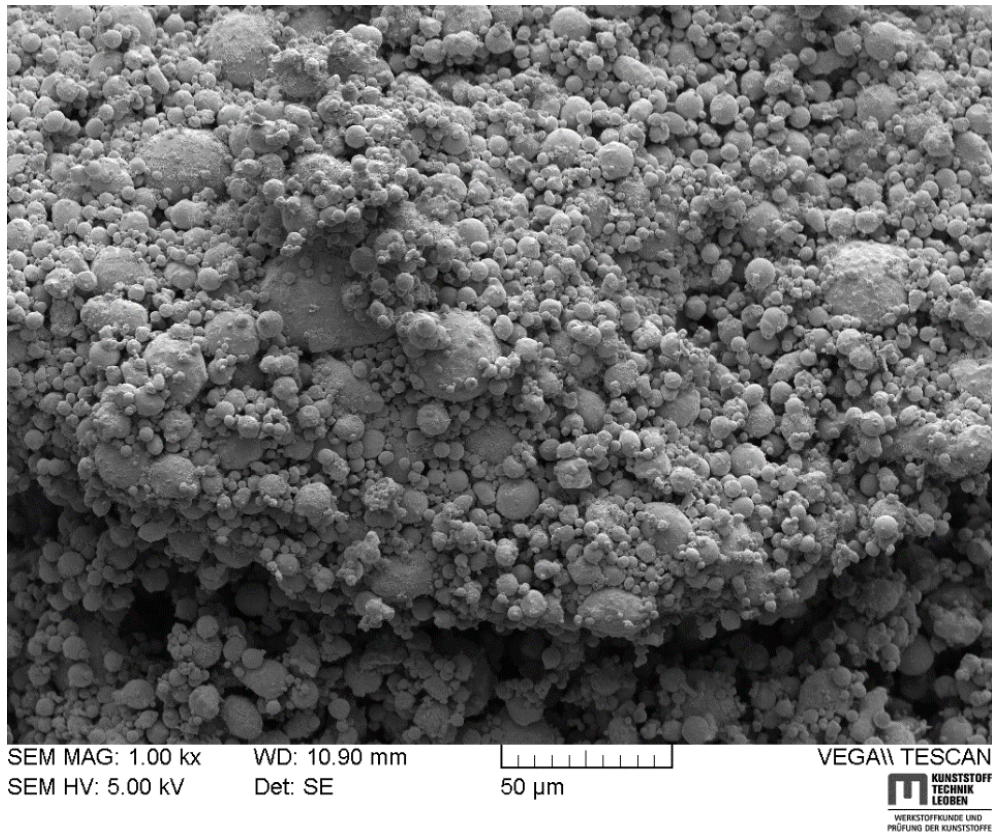


Figure 45: TGA rest of a PolyMIM 17-4PH specimen with magnification of 1000 times under an SEM.

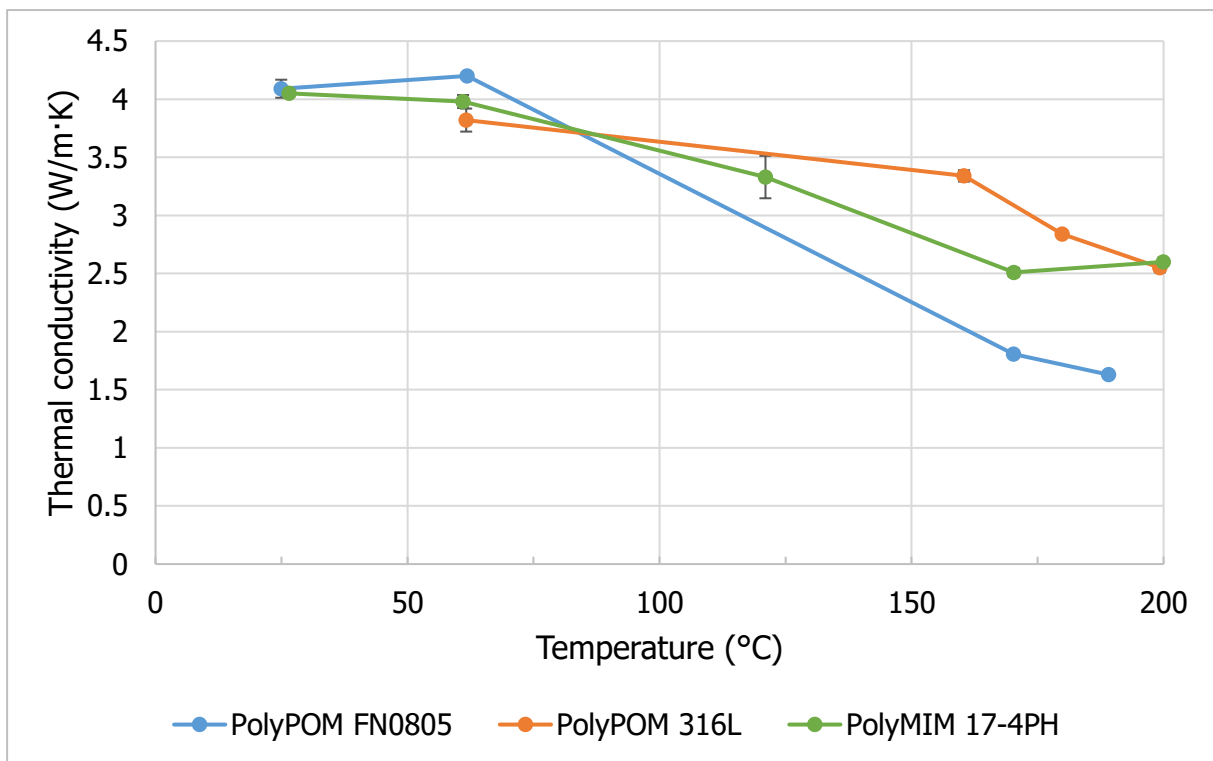


Figure 46: Measured thermal conductivity values used for the simulation.

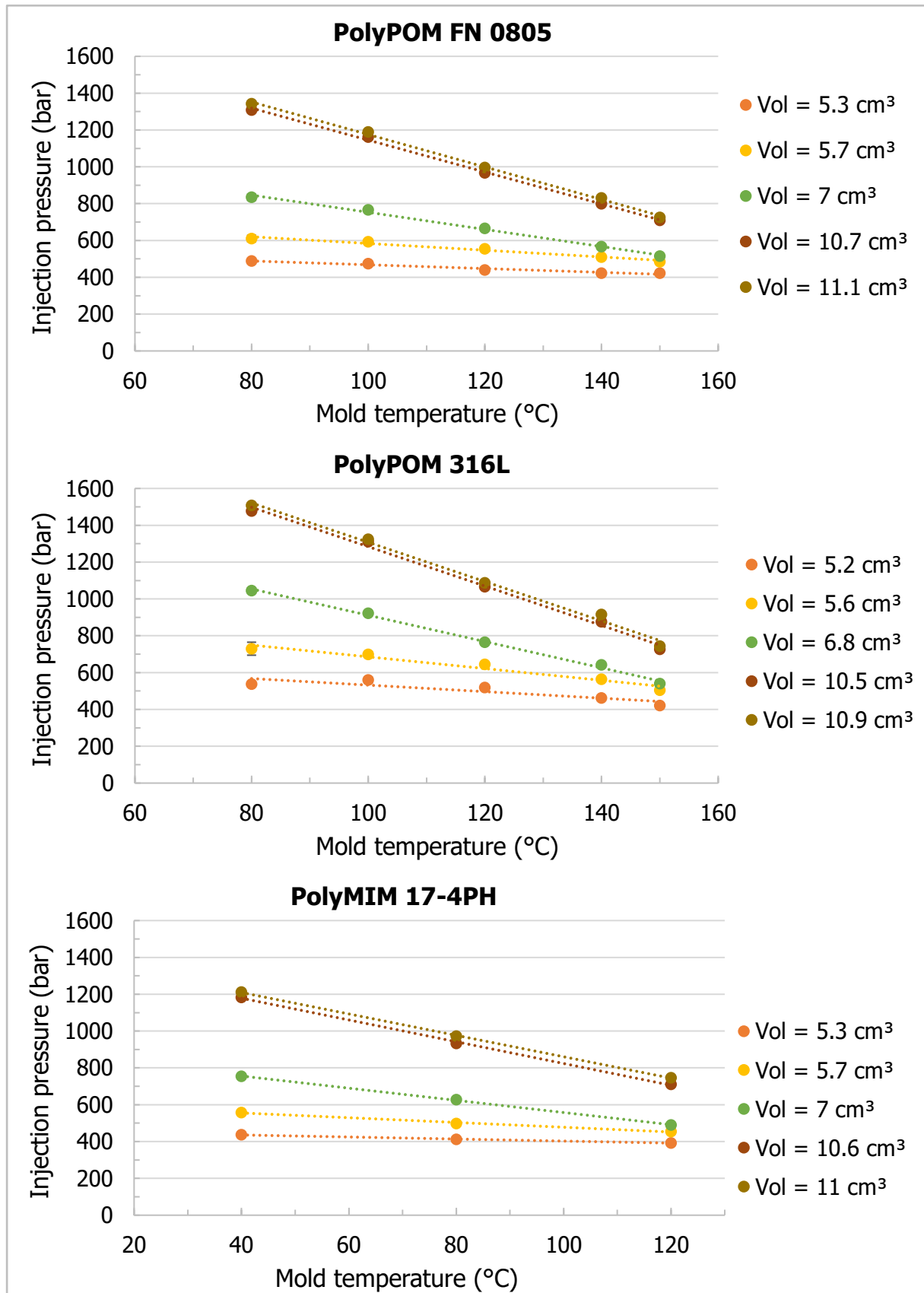


Figure 47: Injection pressures of the dog bone specimens for all three materials in dependence of the mold temperature with linear approximations for all used injection volumes (Vol) and for an injection rate of 5 cm<sup>3</sup>/s.

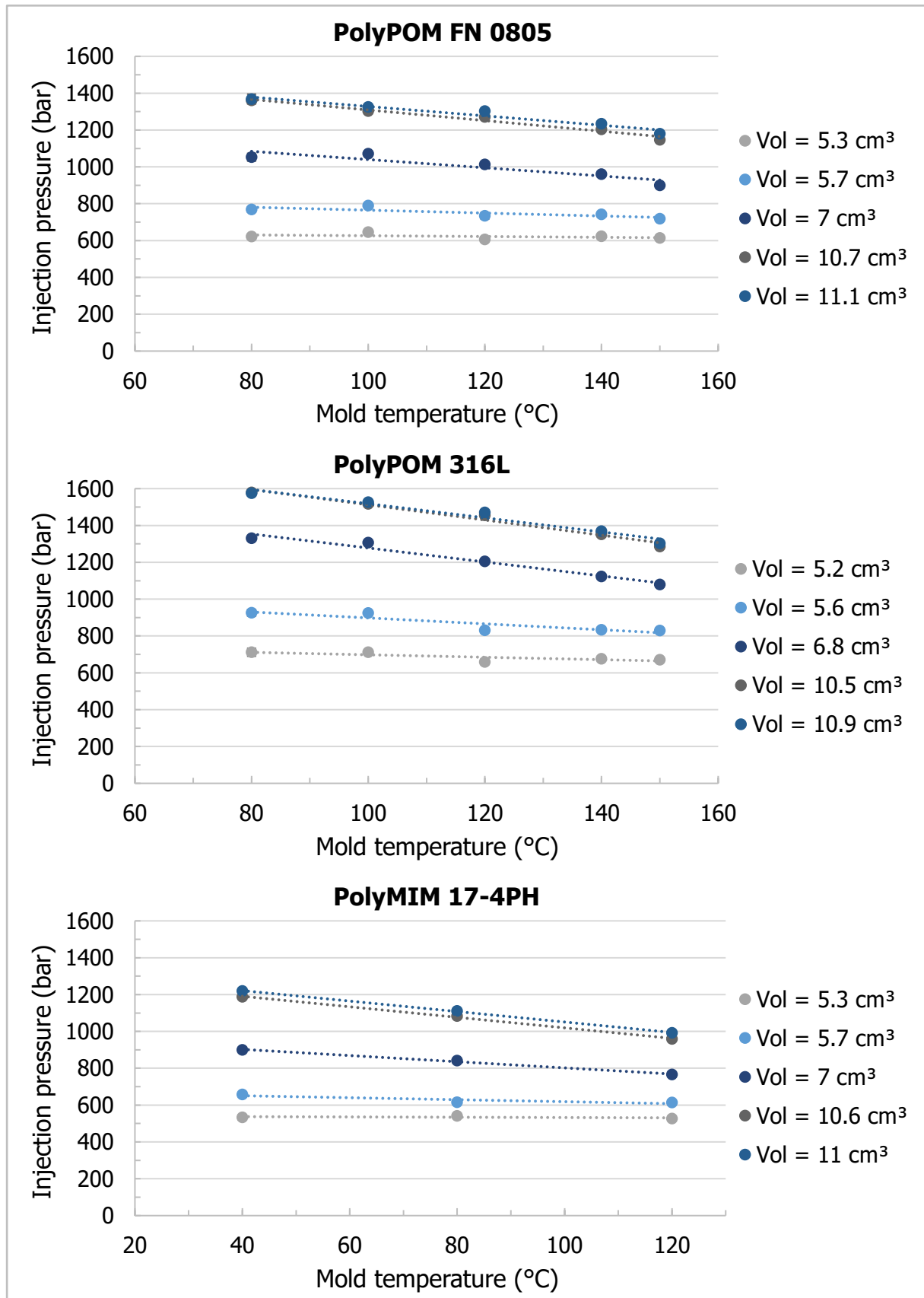


Figure 48: Injection pressures of the dog bone specimens for all three materials in dependence of the mold temperature with linear approximations for all used injection volumes (Vol) and for an injection rate of 20 cm<sup>3</sup>/s.



**Filling study of PolyPOM FN0805 – Tensile specimens,  $\dot{V} = 20 \text{ cm}^3/\text{s}$ :**

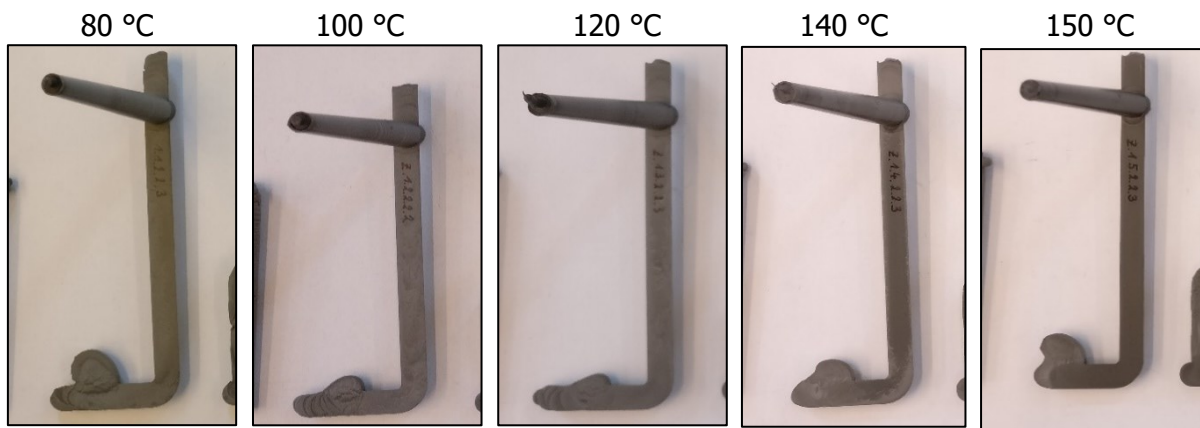


Figure 49: Step 2 of the filling study of PolyPOM FN0805 tensile specimens at an injection rate of  $20 \text{ cm}^3/\text{s}$  at different mold temperatures.

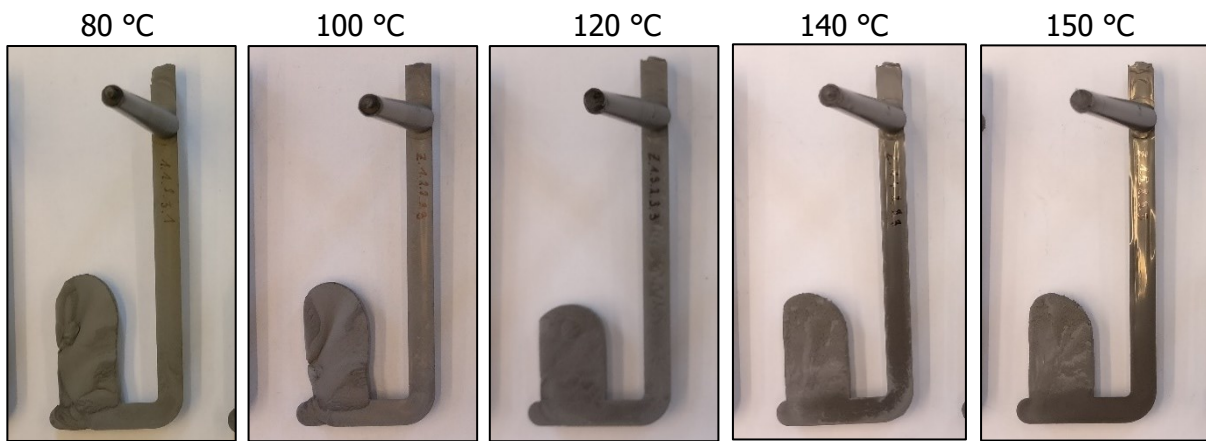


Figure 50: Step 3 of the filling study of PolyPOM FN0805 tensile specimens at an injection rate of  $20 \text{ cm}^3/\text{s}$  at different mold temperatures.

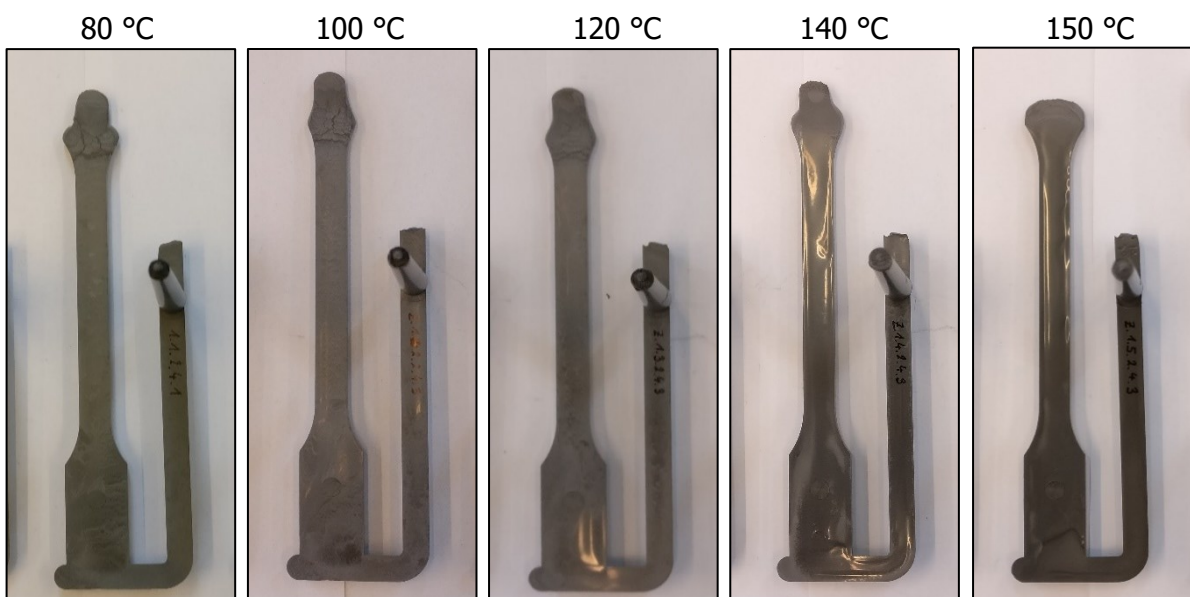


Figure 51: Step 4 of the filling study of PolyPOM FN0805 tensile specimens at an injection rate of  $20 \text{ cm}^3/\text{s}$  at different mold temperatures.

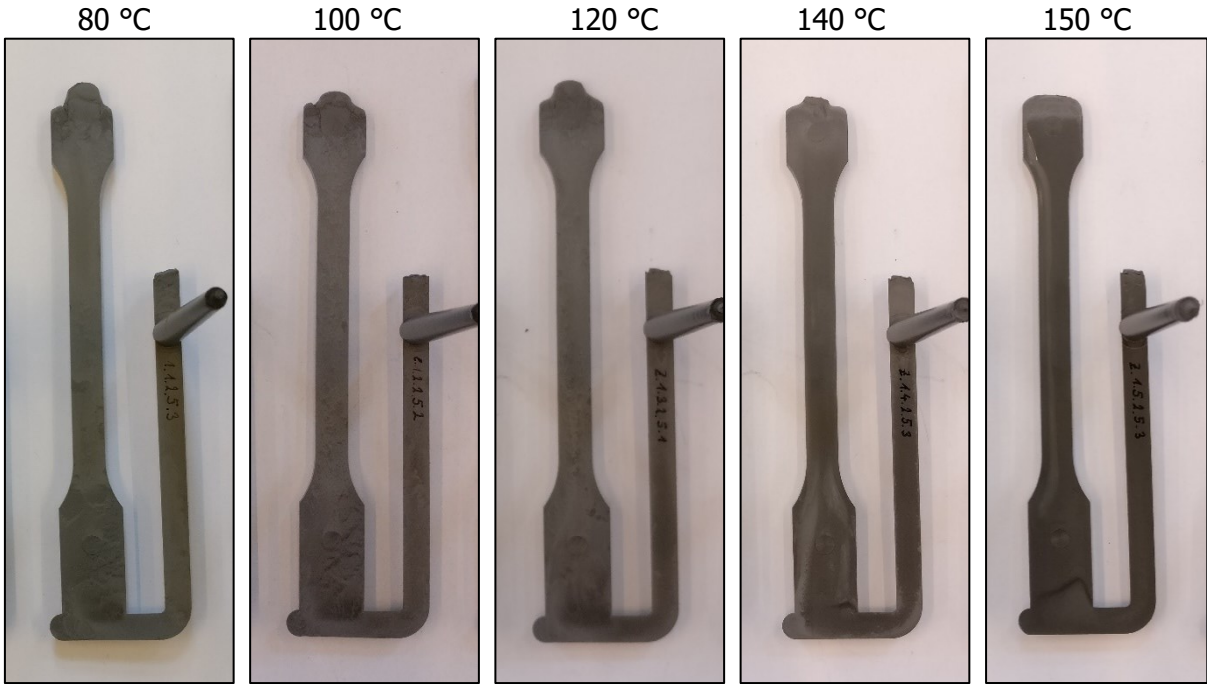


Figure 52: Step 5 of the filling study of PolyPOM FN0805 tensile specimens at an injection rate of 20 cm<sup>3</sup>/s at different mold temperatures.

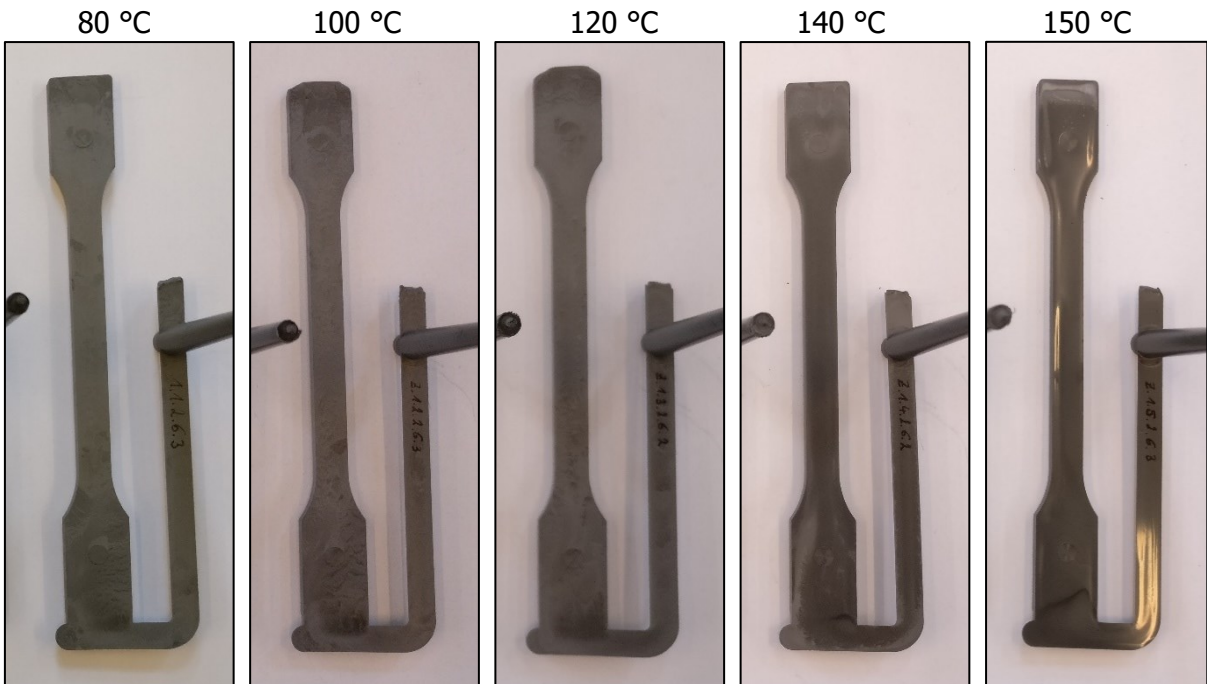


Figure 53: Step 6 of the filling study of PolyPOM FN0805 tensile specimens at an injection rate of 20 cm<sup>3</sup>/s at different mold temperatures.

**Filling study of PolyPOM FN0805 – Dog bone specimens,  $\dot{V} = 5 \text{ cm}^3/\text{s}$ :**

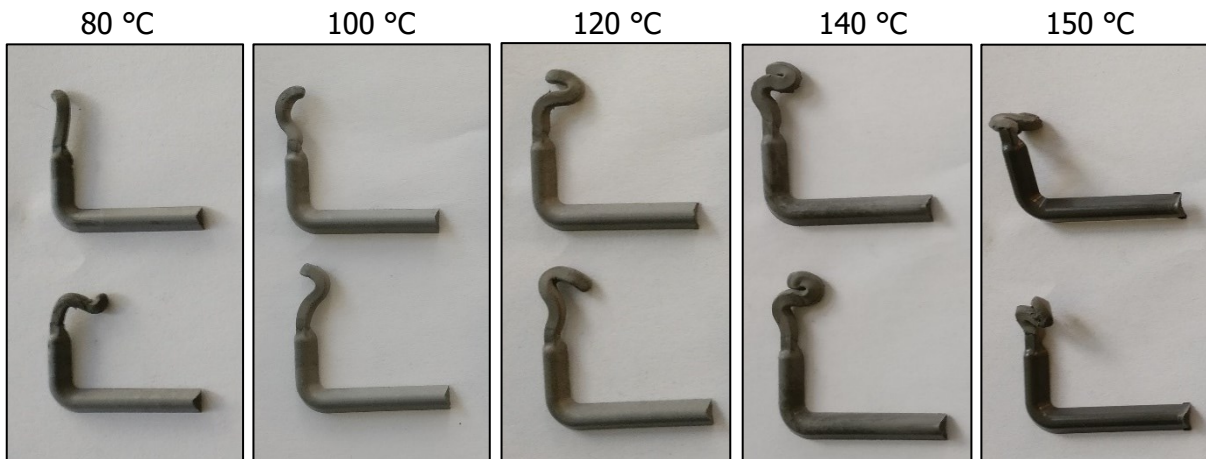


Figure 54: Step 1 of the filling study of PolyPOM FN0805 dog bone specimens at an injection rate of  $5 \text{ cm}^3/\text{s}$  at different mold temperatures.

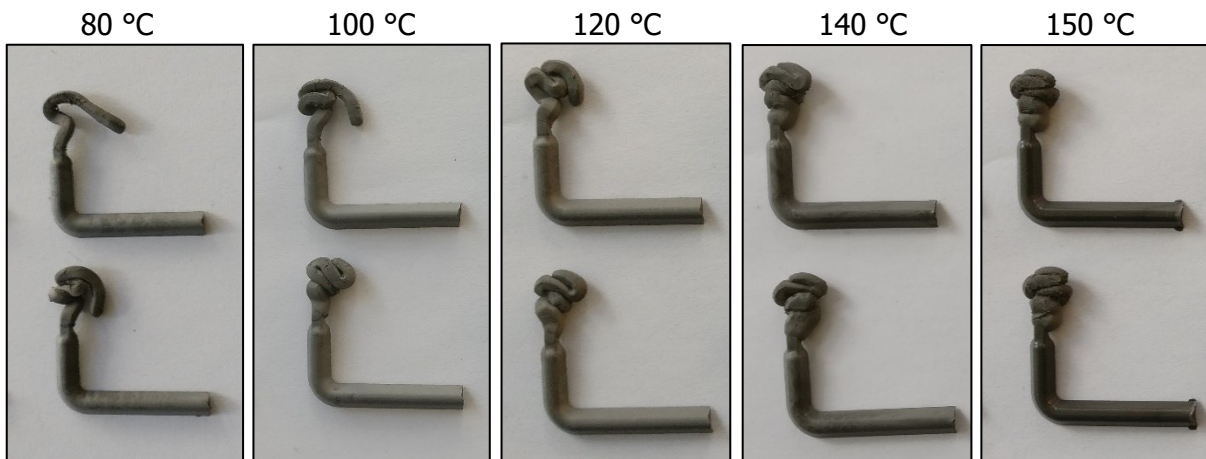


Figure 55: Step 2 of the filling study of PolyPOM FN0805 dog bone specimens at an injection rate of  $5 \text{ cm}^3/\text{s}$  at different mold temperatures.

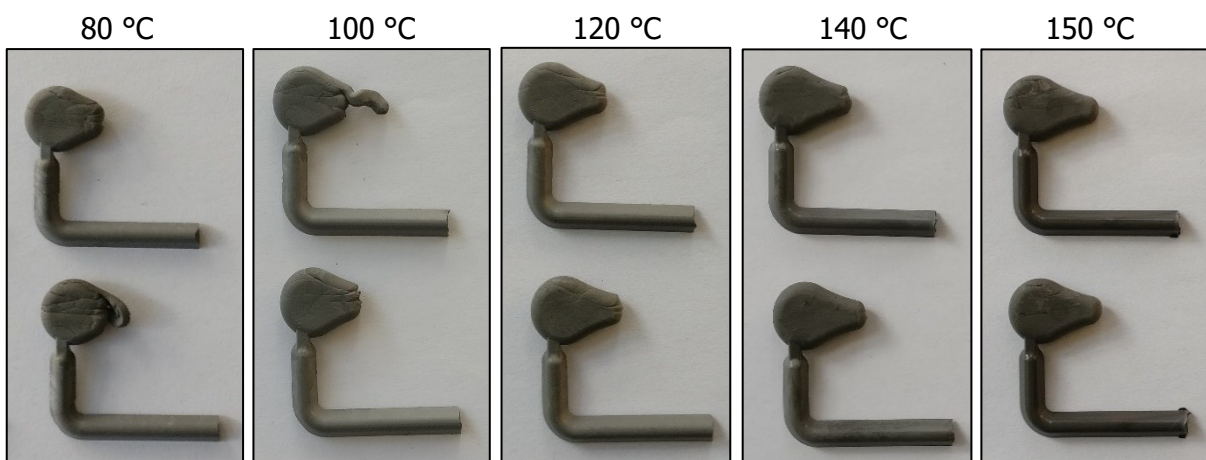


Figure 56: Step 3 of the filling study of PolyPOM FN0805 dog bone specimens at an injection rate of  $5 \text{ cm}^3/\text{s}$  at different mold temperatures.

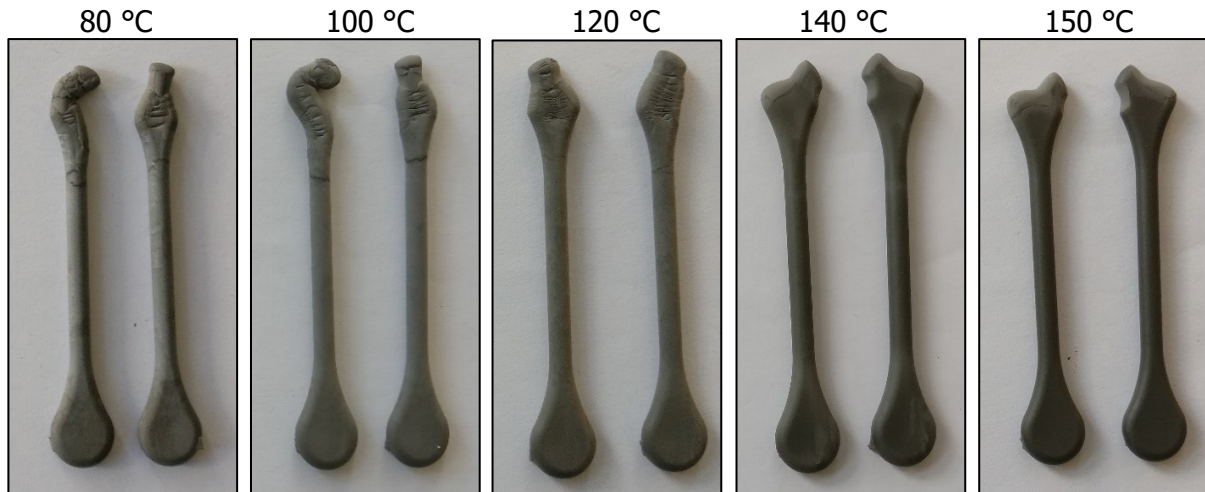


Figure 57: Step 4 of the filling study of PolyPOM FN0805 dog bone specimens at an injection rate of 5 cm<sup>3</sup>/s at different mold temperatures.

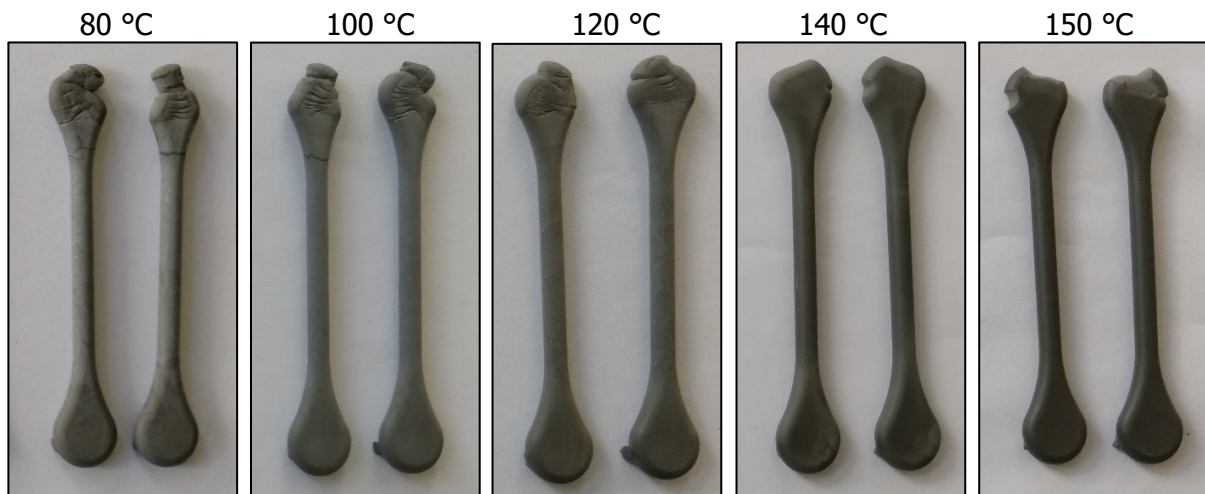


Figure 58: Step 5 of the filling study of PolyPOM FN0805 dog bone specimens at an injection rate of 5 cm<sup>3</sup>/s at different mold temperatures.

**Filling study of PolyPOM FN0805 – Dog bone specimens,  $\dot{V} = 20 \text{ cm}^3/\text{s}$ :**

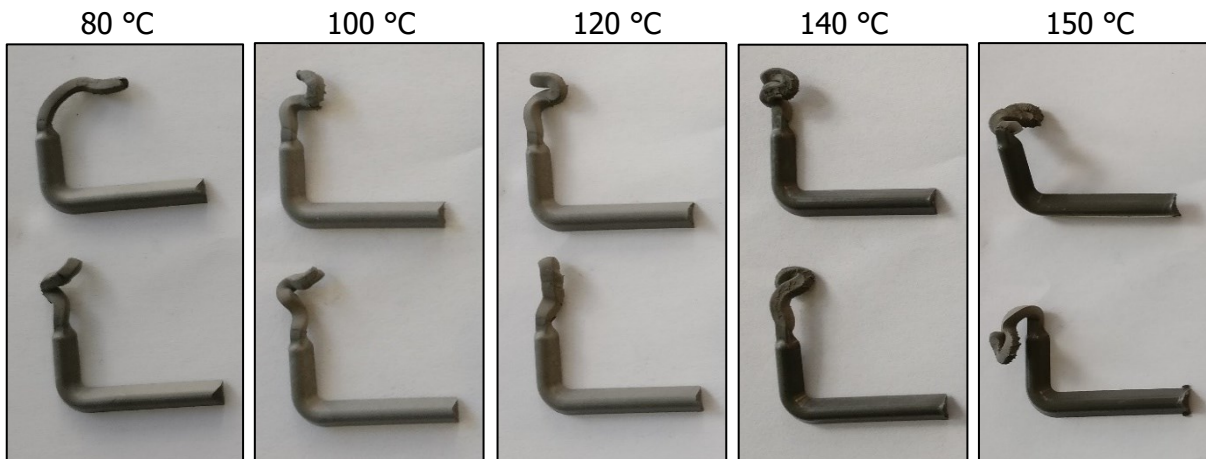


Figure 59: Step 1 of the filling study of PolyPOM FN0805 dog bone specimens at an injection rate of  $20 \text{ cm}^3/\text{s}$  at different mold temperatures.

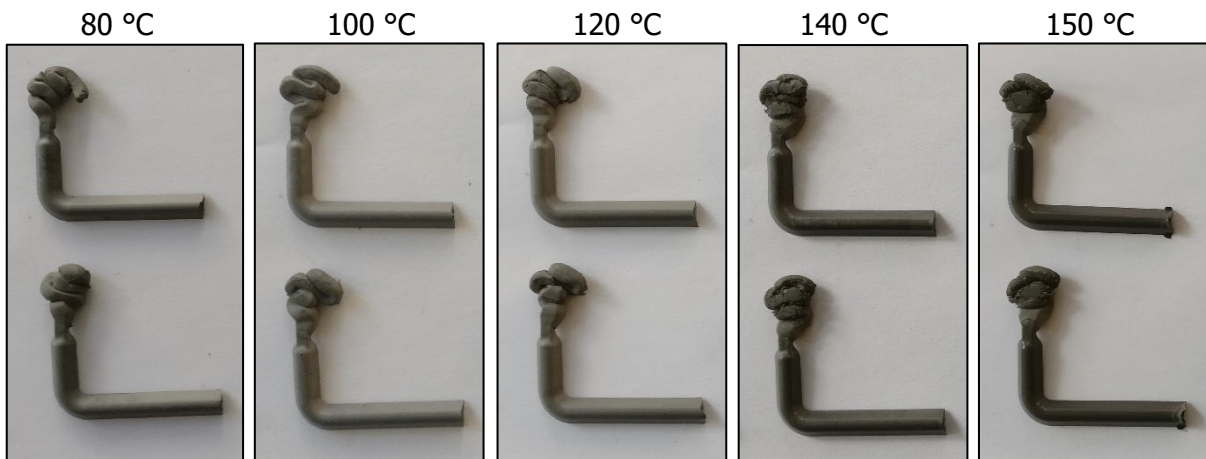


Figure 60: Step 2 of the filling study of PolyPOM FN0805 dog bone specimens at an injection rate of  $20 \text{ cm}^3/\text{s}$  at different mold temperatures.

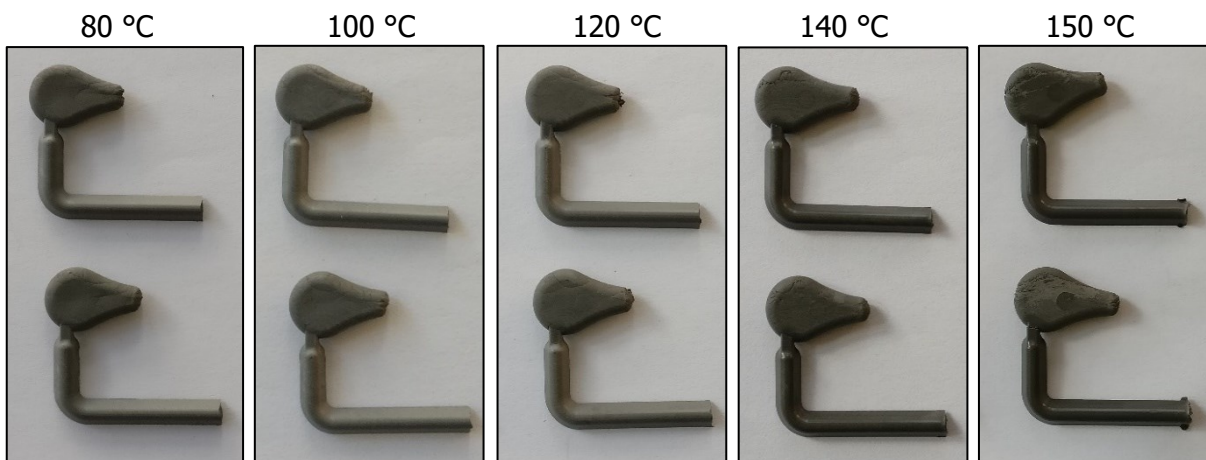


Figure 61: Step 3 of the filling study of PolyPOM FN0805 dog bone specimens at an injection rate of  $20 \text{ cm}^3/\text{s}$  at different mold temperatures.

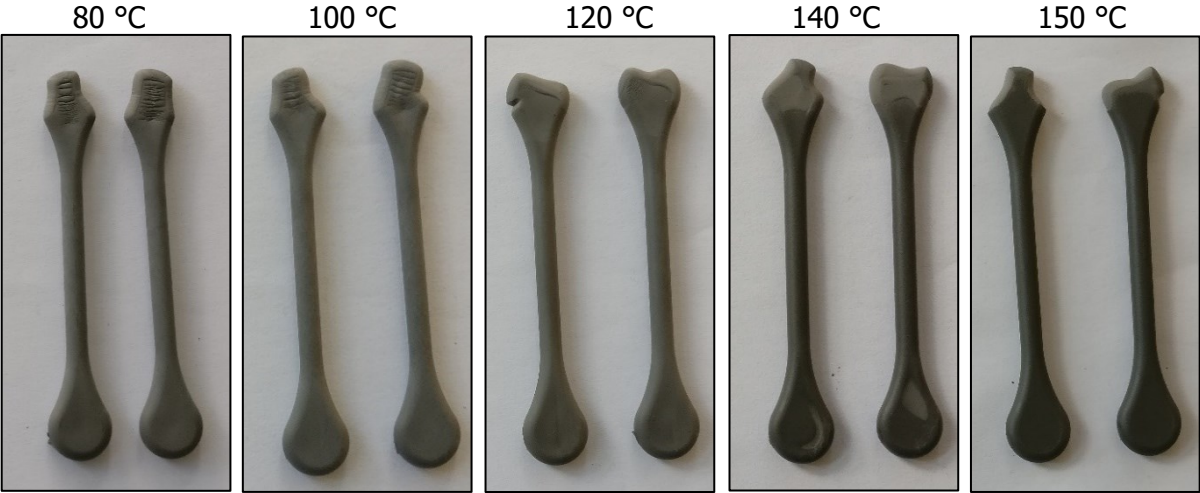


Figure 62: Step 4 of the filling study of PolyPOM FN0805 dog bone specimens at an injection rate of 20 cm<sup>3</sup>/s at different mold temperatures.

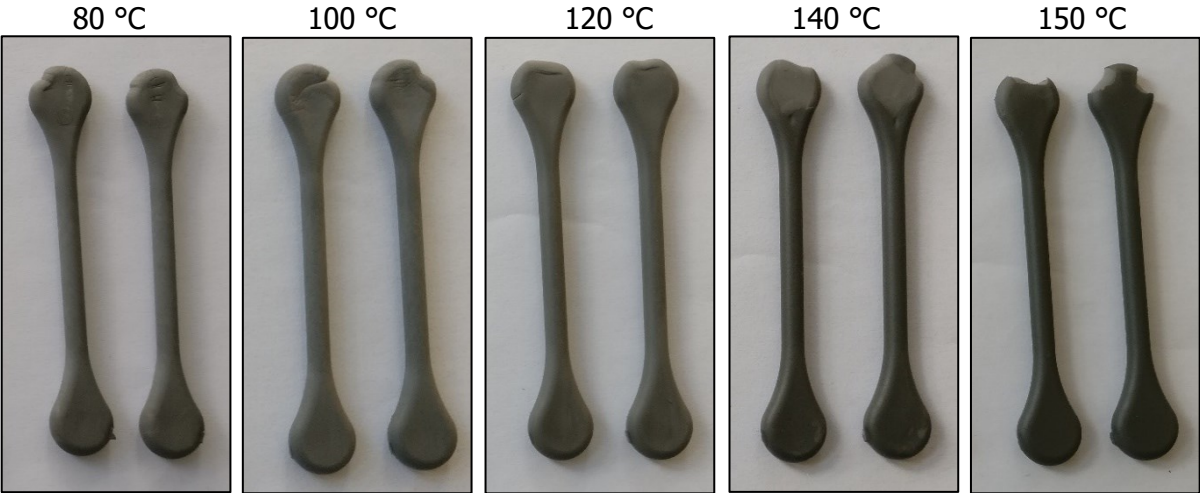


Figure 63: Step 5 of the filling study of PolyPOM FN0805 dog bone specimens at an injection rate of 20 cm<sup>3</sup>/s at different mold temperatures.

**Filling study of PolyPOM 316L – Tensile specimens,  $\dot{V} = 5 \text{ cm}^3/\text{s}$ :**

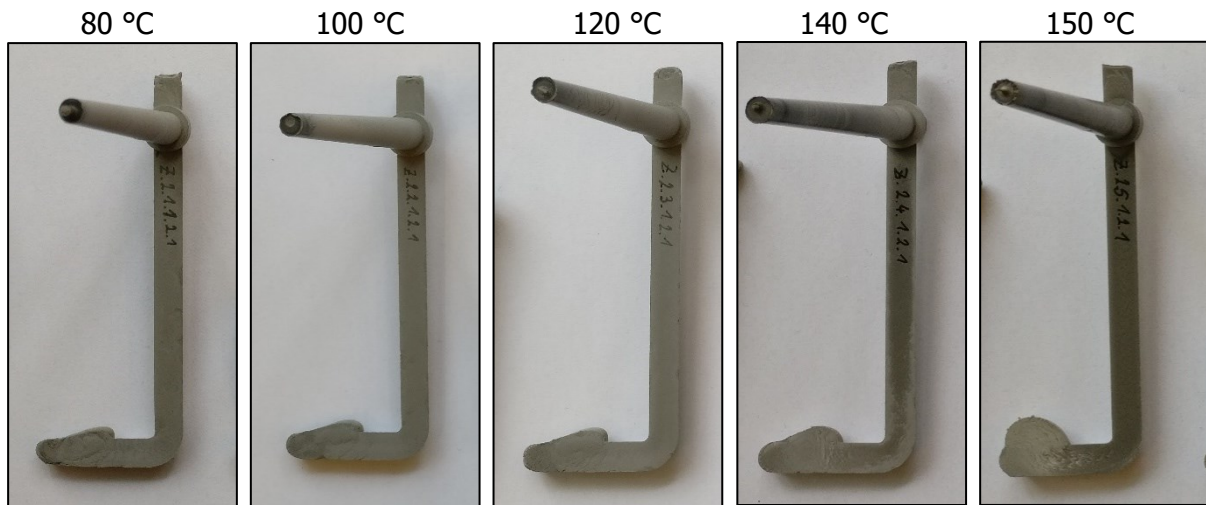


Figure 64: Step 2 of the filling study of PolyPOM 316L tensile specimens at an injection rate of  $5 \text{ cm}^3/\text{s}$  at different mold temperatures.

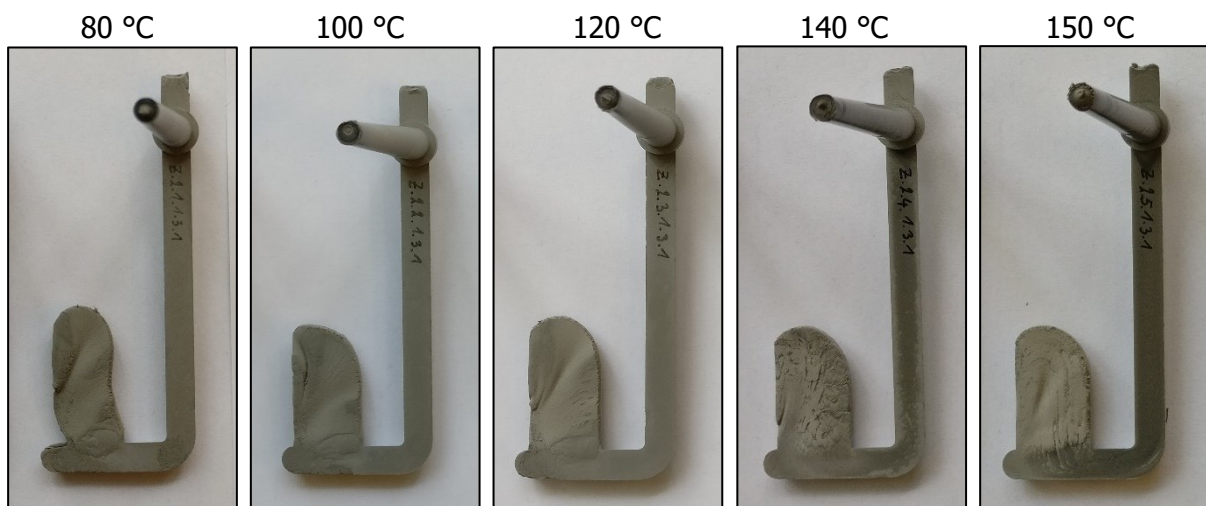


Figure 65: Step 3 of the filling study of PolyPOM 316L tensile specimens at an injection rate of  $5 \text{ cm}^3/\text{s}$  at different mold temperatures.

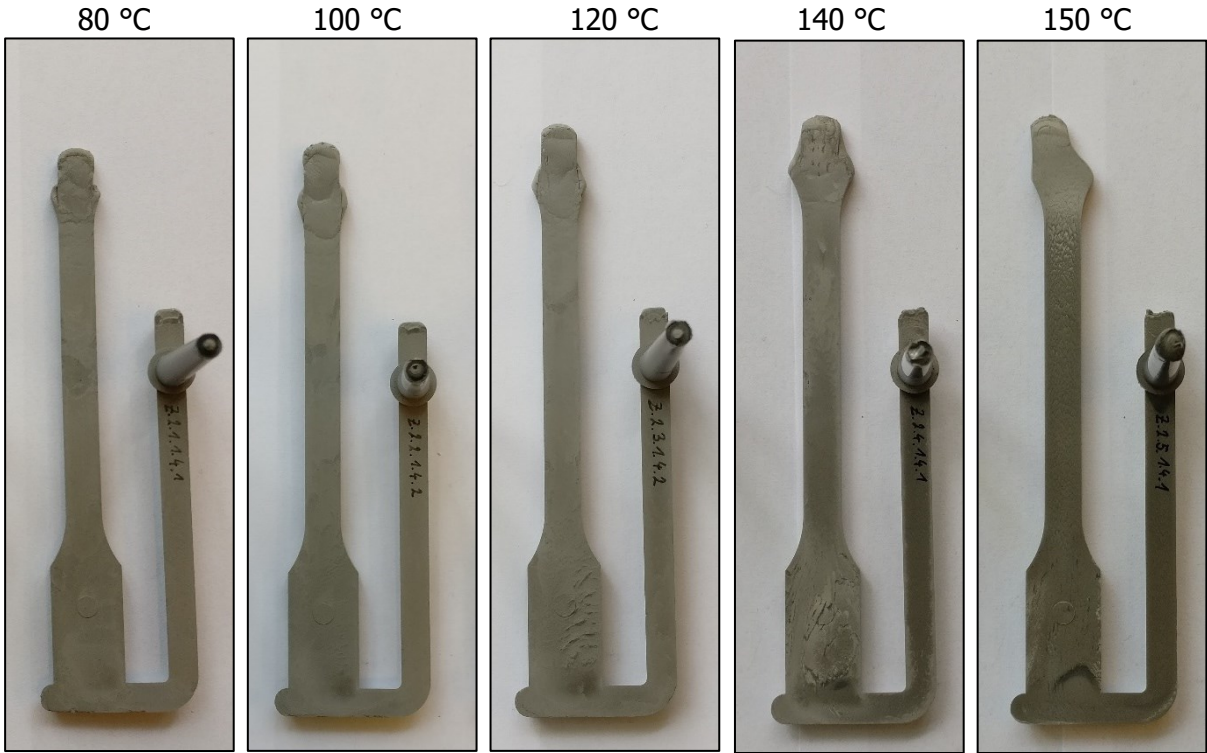


Figure 66: Step 4 of the filling study of PolyPOM 316L tensile specimens at an injection rate of 5 cm<sup>3</sup>/s at different mold temperatures.

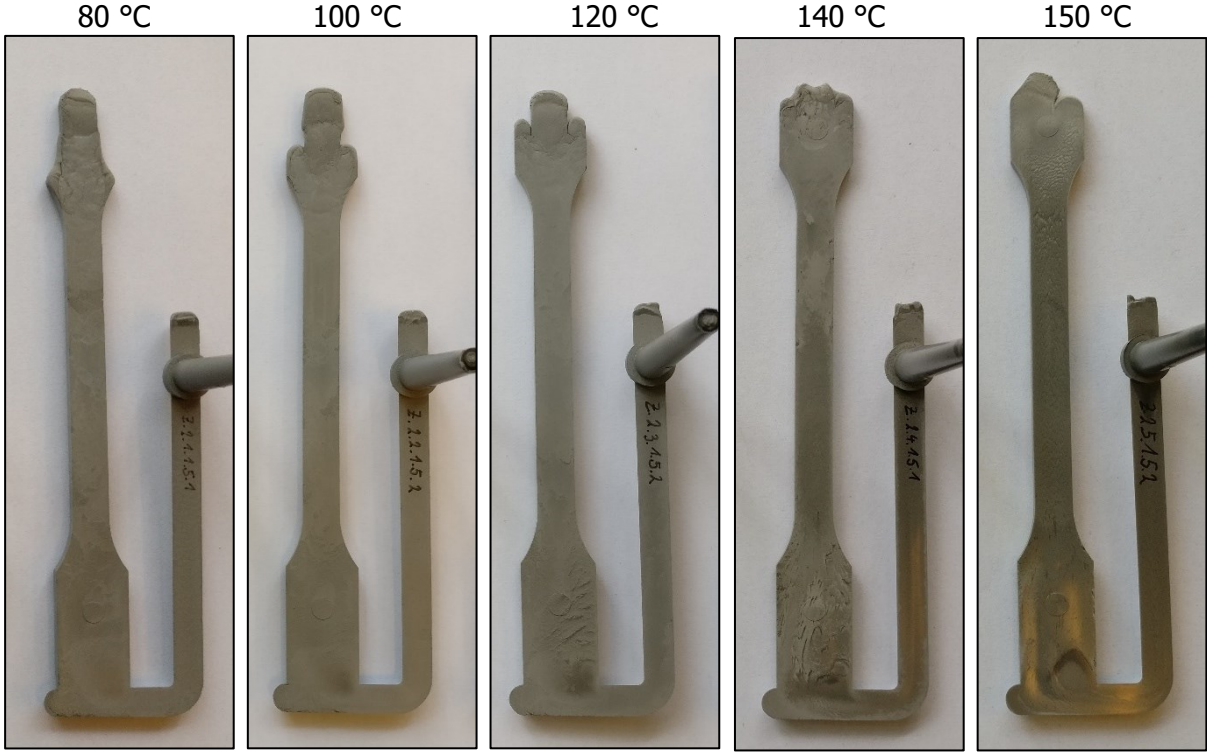


Figure 67: Step 5 of the filling study of PolyPOM 316L tensile specimens at an injection rate of 5 cm<sup>3</sup>/s at different mold temperatures.



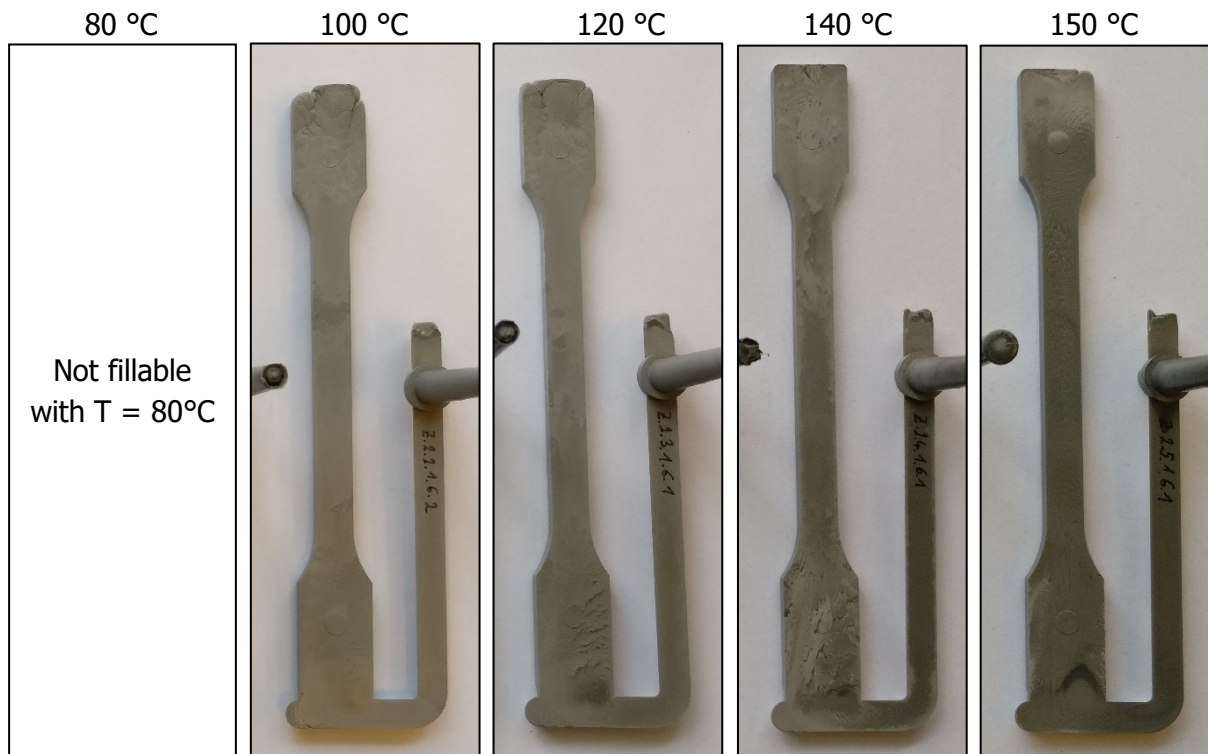


Figure 68: Step 6 of the filling study of PolyPOM 316L tensile specimens at an injection rate of  $5 \text{ cm}^3/\text{s}$  at different mold temperatures.

**Filling study of PolyPOM 316L – Tensile specimens,  $\dot{V} = 20 \text{ cm}^3/\text{s}$ :**

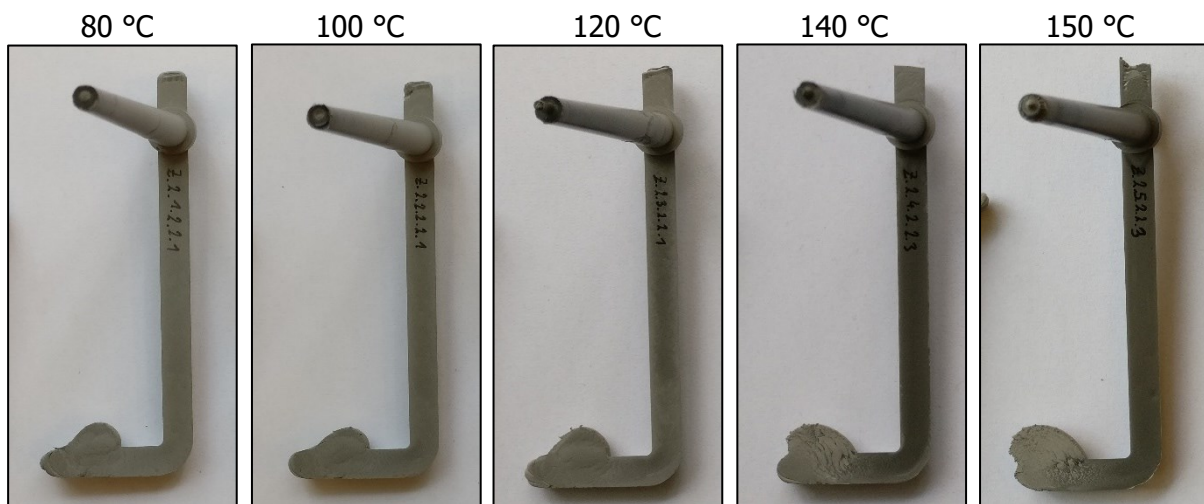


Figure 69: Step 2 of the filling study of PolyPOM 316L tensile specimens at an injection rate of  $20 \text{ cm}^3/\text{s}$  at different mold temperatures.

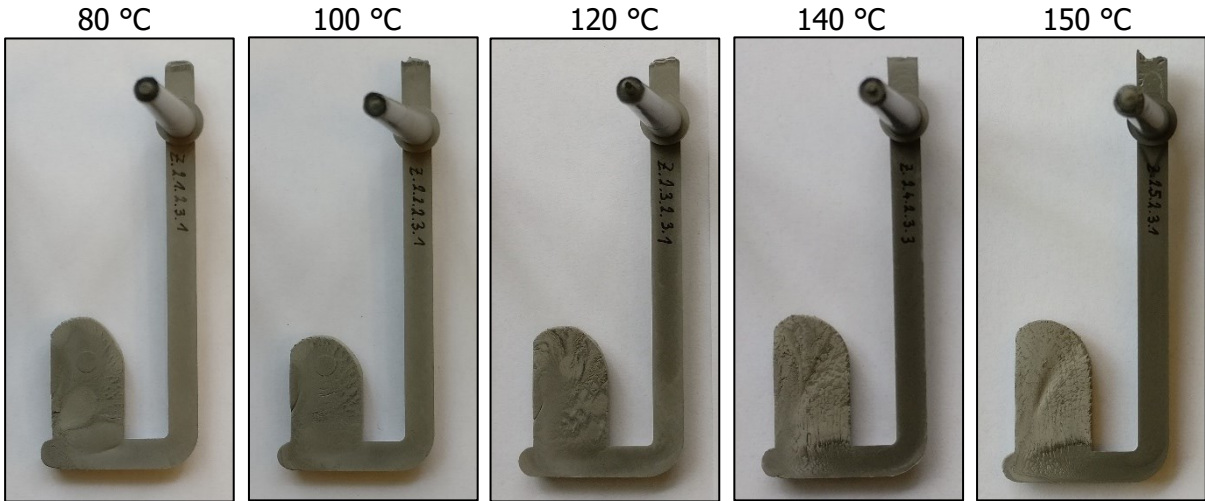


Figure 70: Step 3 of the filling study of PolyPOM 316L tensile specimens at an injection rate of 20 cm<sup>3</sup>/s at different mold temperatures.

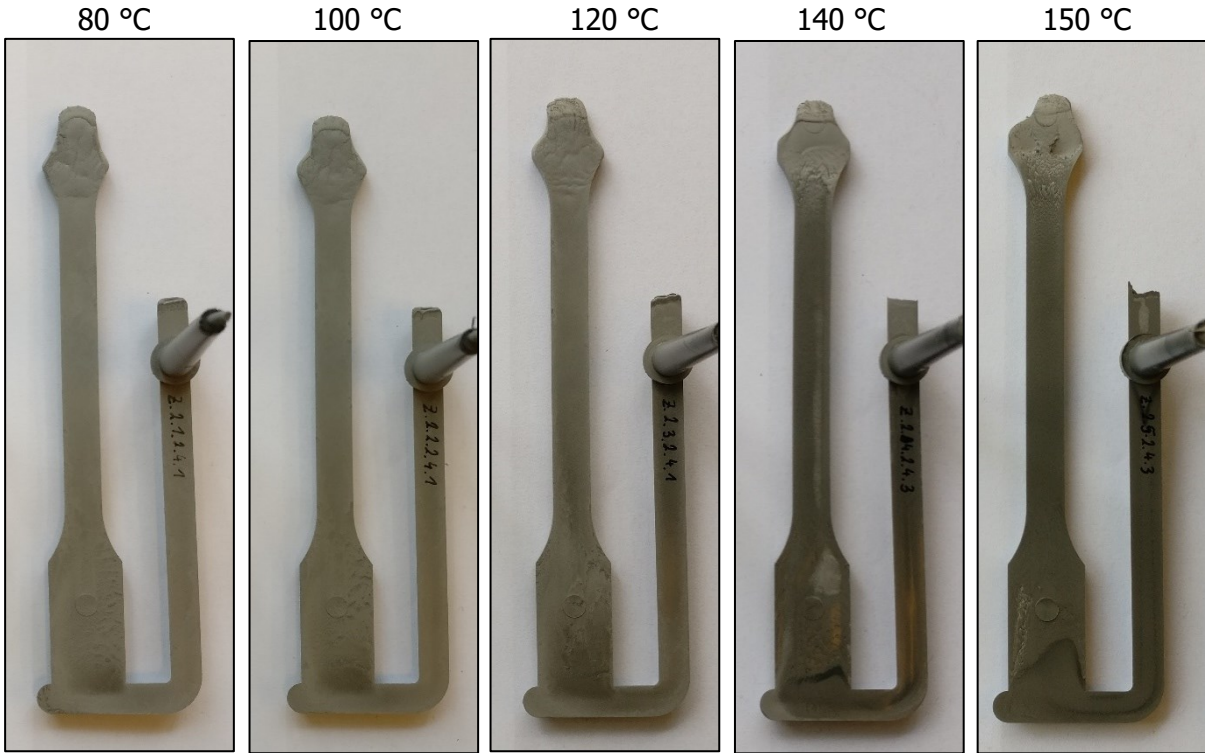


Figure 71: Step 4 of the filling study of PolyPOM 316L tensile specimens at an injection rate of 20 cm<sup>3</sup>/s at different mold temperatures.

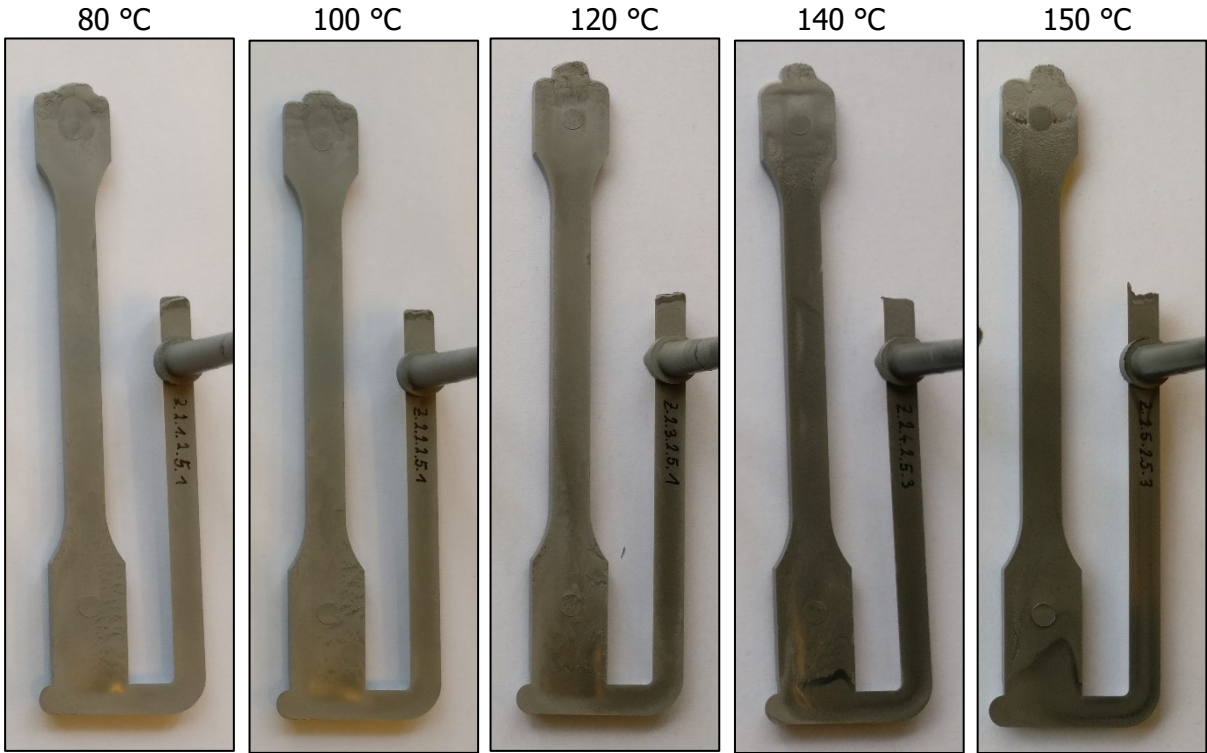


Figure 72: Step 5 of the filling study of PolyPOM 316L tensile specimens at an injection rate of 20 cm<sup>3</sup>/s at different mold temperatures.

**Filling study of PolyPOM 316L – Dog bone specimens,  $\dot{V} = 5 \text{ cm}^3/\text{s}$ :**

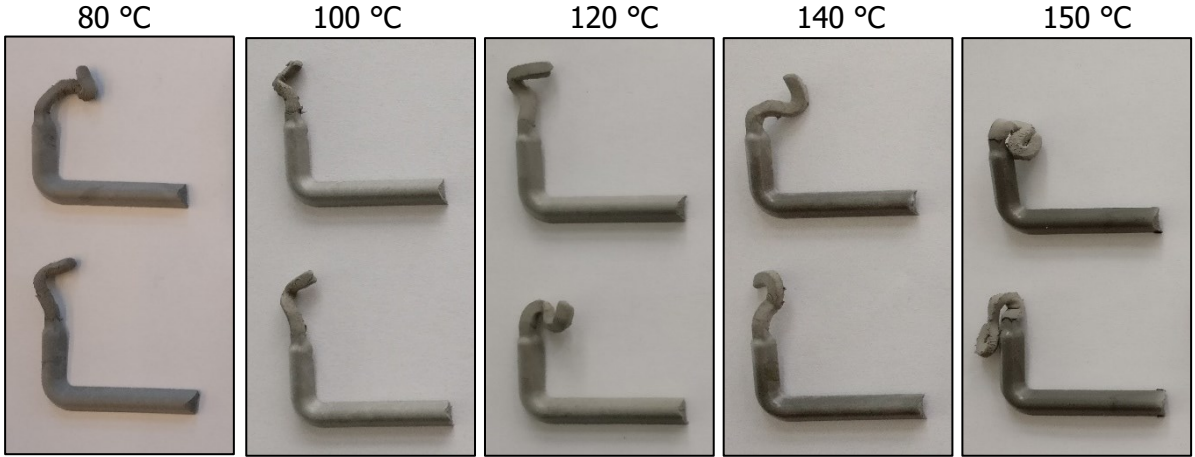


Figure 73: Step 1 of the filling study of PolyPOM 316L dog bone specimens at an injection rate of 5 cm<sup>3</sup>/s at different mold temperatures.

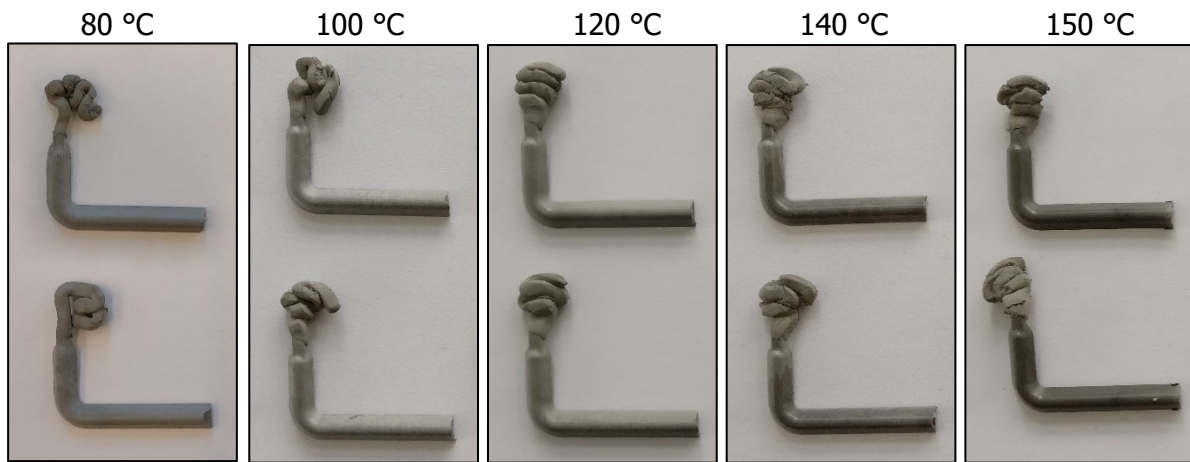


Figure 74: Step 2 of the filling study of PolyPOM 316L dog bone specimens at an injection rate of 5 cm<sup>3</sup>/s at different mold temperatures.

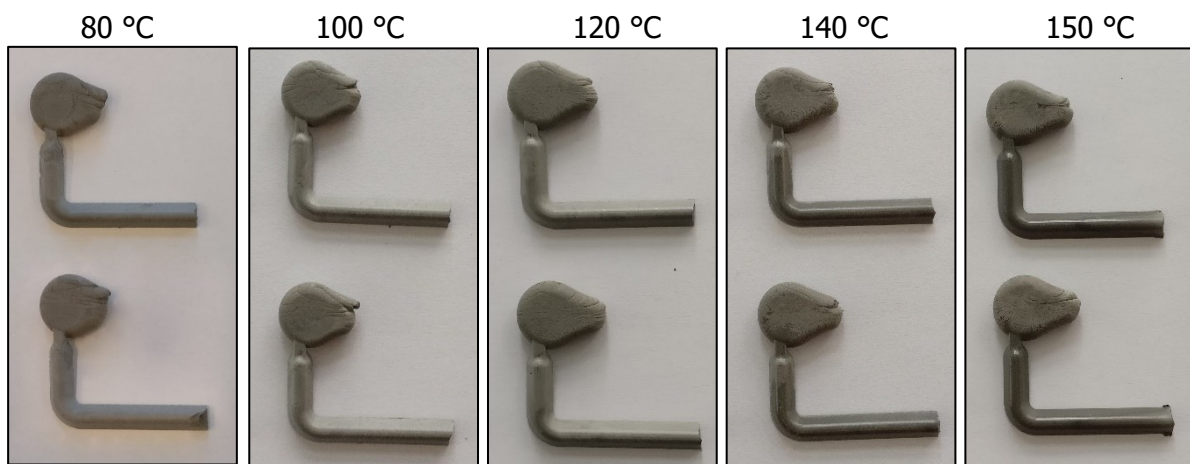


Figure 75: Step 3 of the filling study of PolyPOM 316L dog bone specimens at an injection rate of 5 cm<sup>3</sup>/s at different mold temperatures.

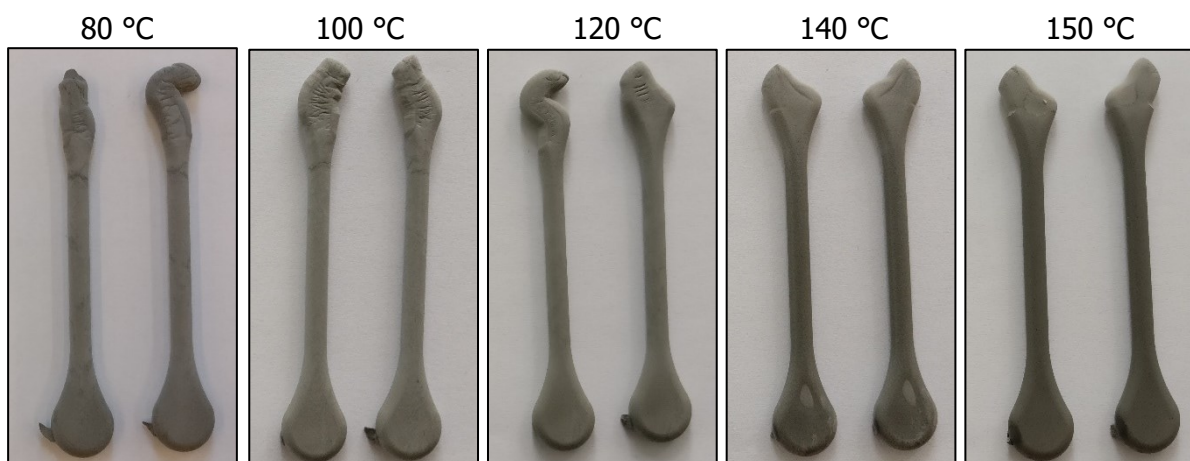


Figure 76: Step 4 of the filling study of PolyPOM 316L dog bone specimens at an injection rate of 5 cm<sup>3</sup>/s at different mold temperatures.

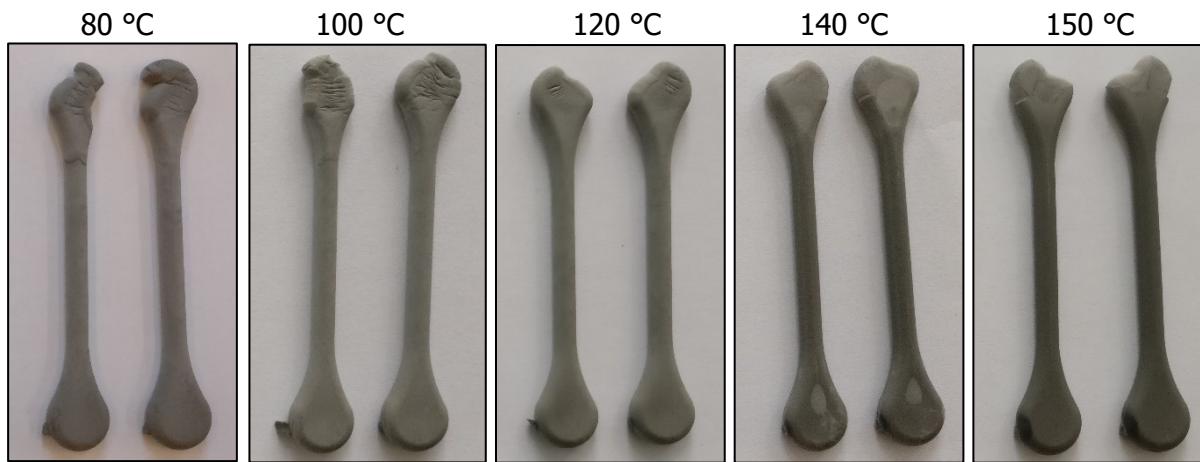


Figure 77: Step 5 of the filling study of PolyPOM 316L dog bone specimens at an injection rate of 5 cm<sup>3</sup>/s at different mold temperatures.

**Filling study of PolyPOM 316L – Dog bone specimens,  $\dot{V} = 20 \text{ cm}^3/\text{s}$ :**

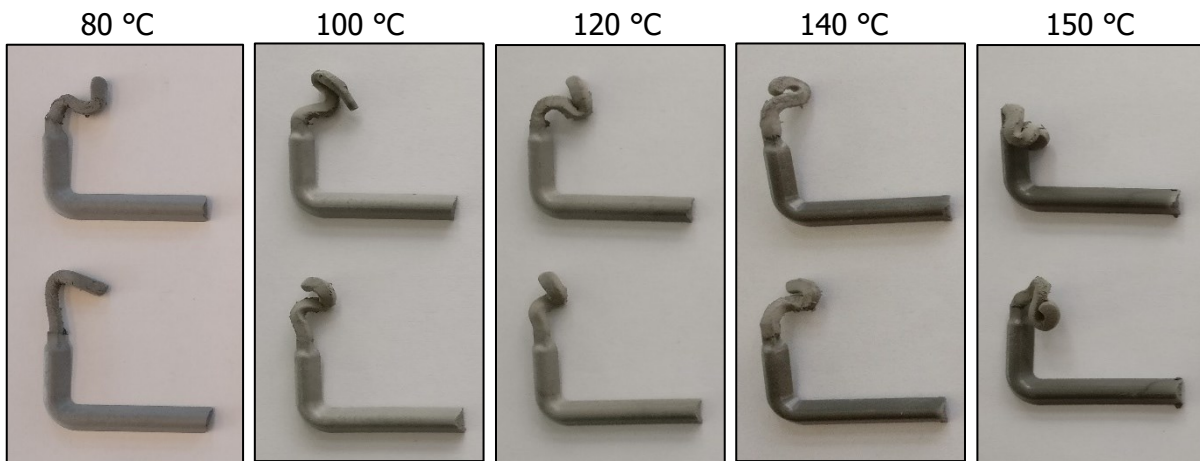


Figure 78: Step 1 of the filling study of PolyPOM 316L dog bone specimens at an injection rate of 20 cm<sup>3</sup>/s at different mold temperatures.

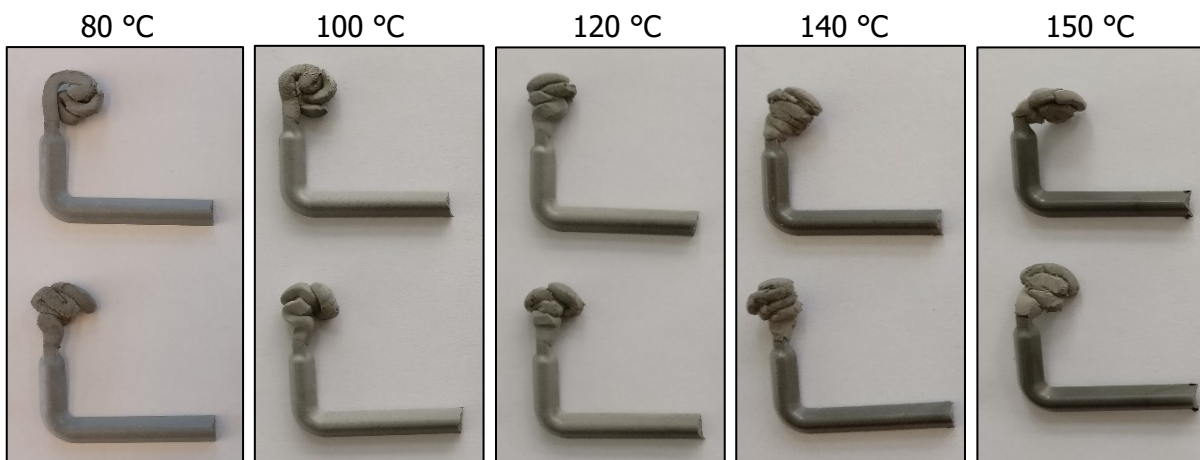


Figure 79: Step 2 of the filling study of PolyPOM 316L dog bone specimens at an injection rate of 20 cm<sup>3</sup>/s at different mold temperatures.

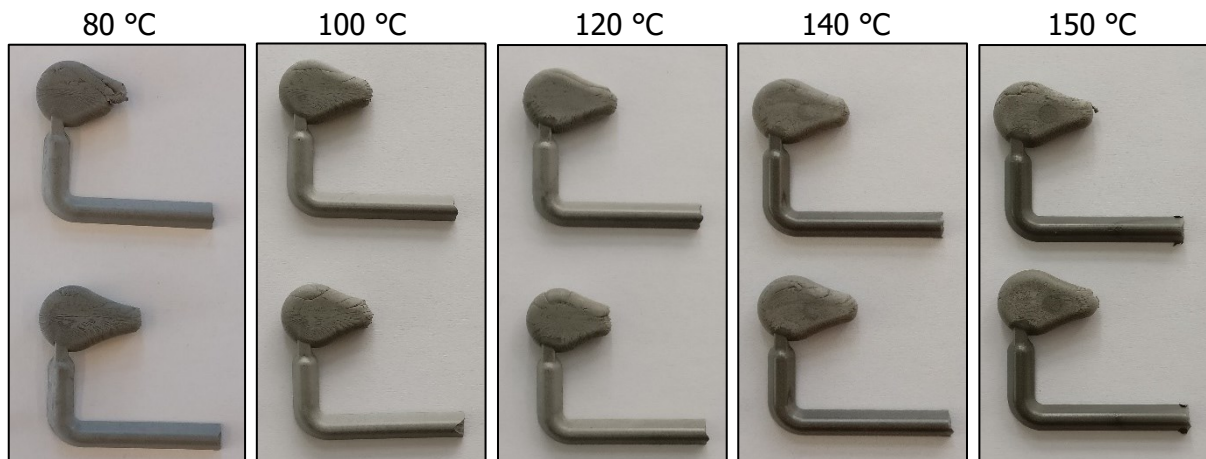


Figure 80: Step 3 of the filling study of PolyPOM 316L dog bone specimens at an injection rate of  $20 \text{ cm}^3/\text{s}$  at different mold temperatures.

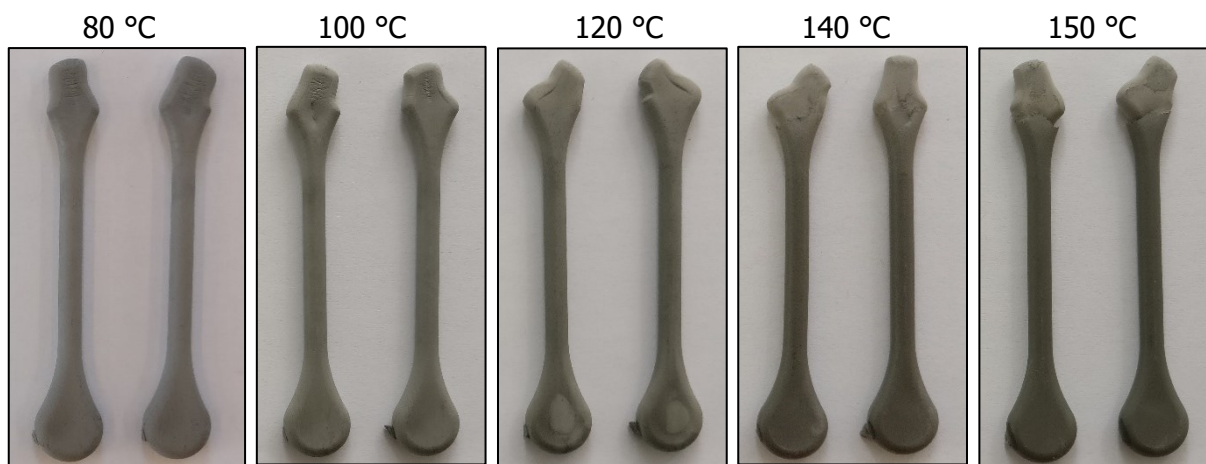


Figure 81: Step 4 of the filling study of PolyPOM 316L dog bone specimens at an injection rate of  $20 \text{ cm}^3/\text{s}$  at different mold temperatures.

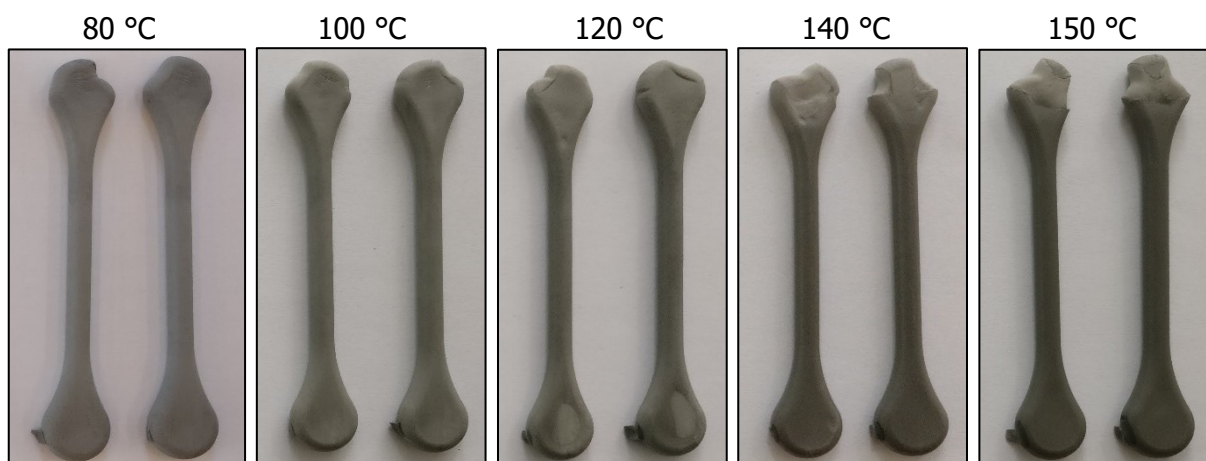


Figure 82: Step 5 of the filling study of PolyPOM 316L dog bone specimens at an injection rate of  $20 \text{ cm}^3/\text{s}$  at different mold temperatures.

**Filling study of PolyMIM 17-4PH – Tensile specimens,  $\dot{V} = 5 \text{ cm}^3/\text{s}$ :**

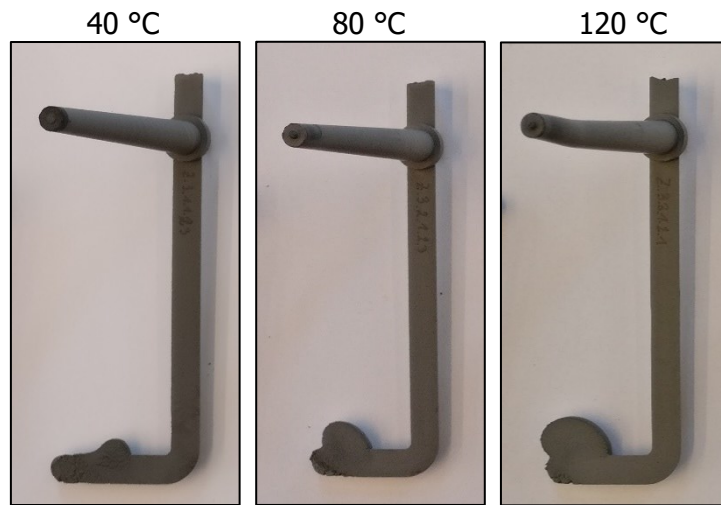


Figure 83: Step 2 of the filling study of PolyMIM 17-4PH tensile specimens at an injection rate of  $5 \text{ cm}^3/\text{s}$  at different mold temperatures.

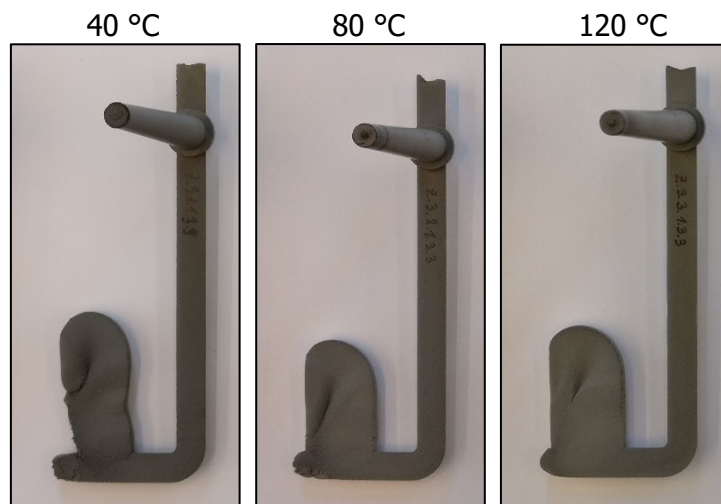


Figure 84: Step 3 of the filling study of PolyMIM 17-4PH tensile specimens at an injection rate of  $5 \text{ cm}^3/\text{s}$  at different mold temperatures.

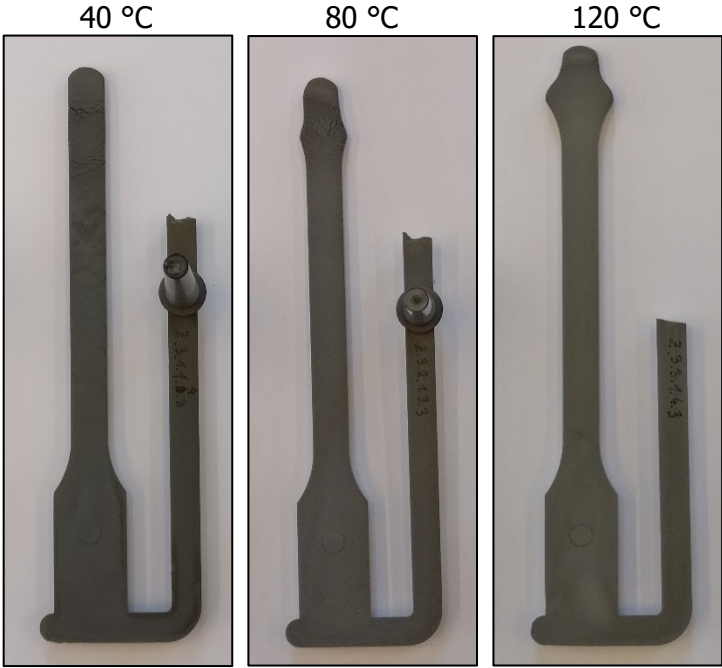


Figure 85: Step 4 of the filling study of PolyMIM 17-4PH tensile specimens at an injection rate of 5 cm<sup>3</sup>/s at different mold temperatures.

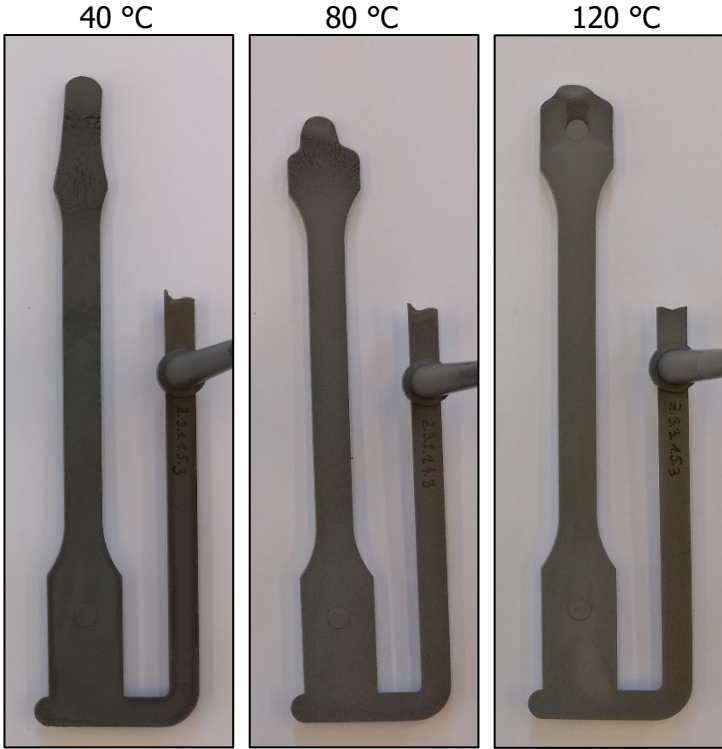


Figure 86: Step 5 of the filling study of PolyMIM 17-4PH tensile specimens at an injection rate of 5 cm<sup>3</sup>/s at different mold temperatures.



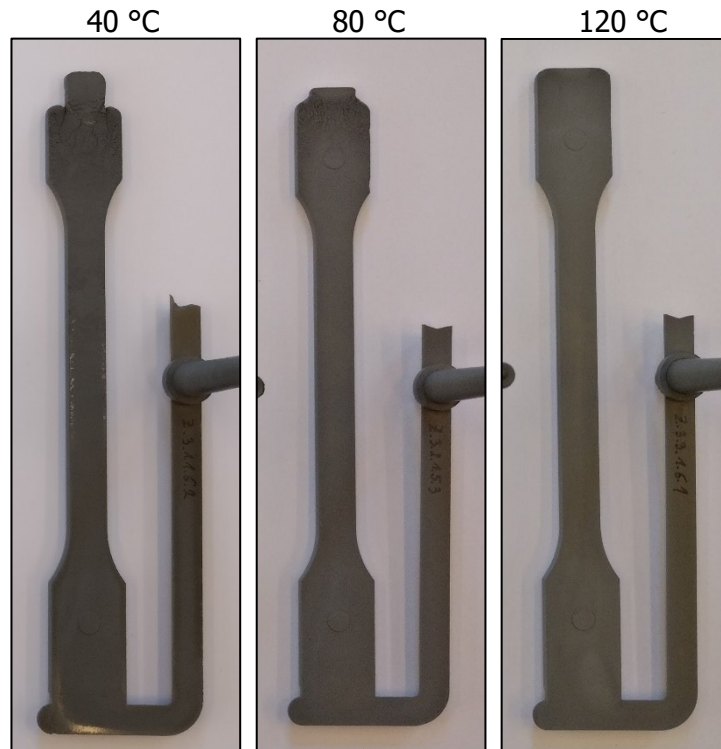


Figure 87: Step 6 of the filling study of PolyMIM 17-4PH tensile specimens at an injection rate of  $5 \text{ cm}^3/\text{s}$  at different mold temperatures.

**Filling study of PolyMIM 17-4PH – Tensile specimens,  $\dot{V} = 20 \text{ cm}^3/\text{s}$ :**

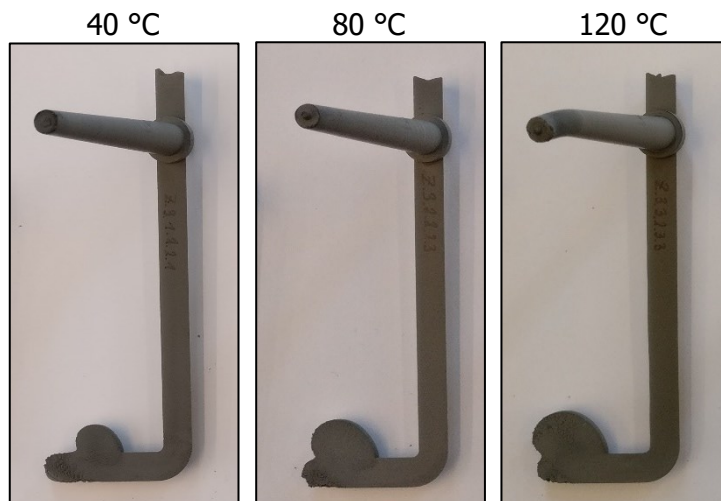


Figure 88: Step 2 of the filling study of PolyMIM 17-4PH tensile specimens at an injection rate of  $20 \text{ cm}^3/\text{s}$  at different mold temperatures.

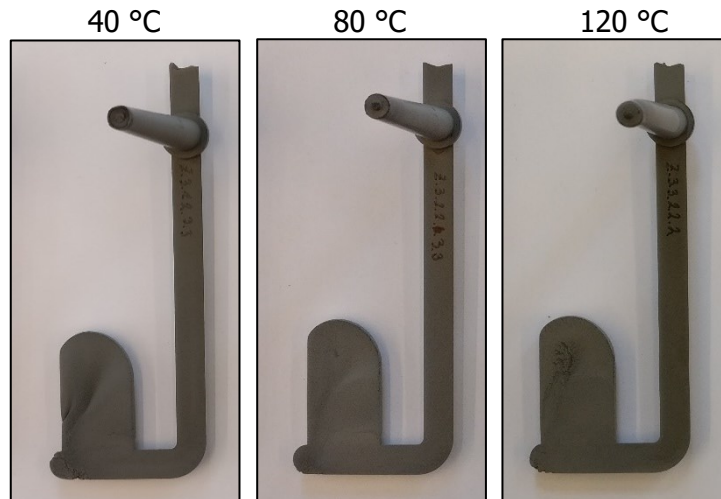


Figure 89: Step 3 of the filling study of PolyMIM 17-4PH tensile specimens at an injection rate of 20 cm<sup>3</sup>/s at different mold temperatures.

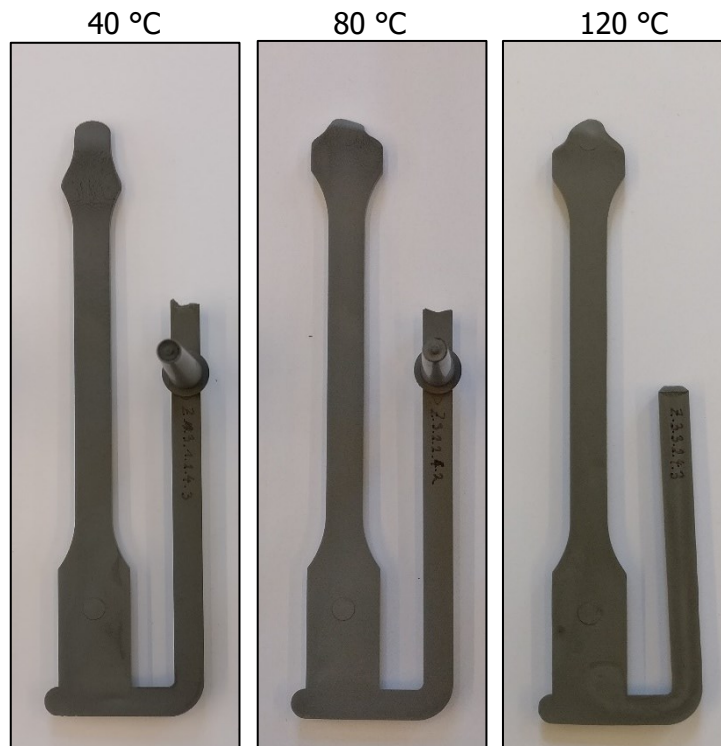


Figure 90: Step 4 of the filling study of PolyMIM 17-4PH tensile specimens at an injection rate of 20 cm<sup>3</sup>/s at different mold temperatures.

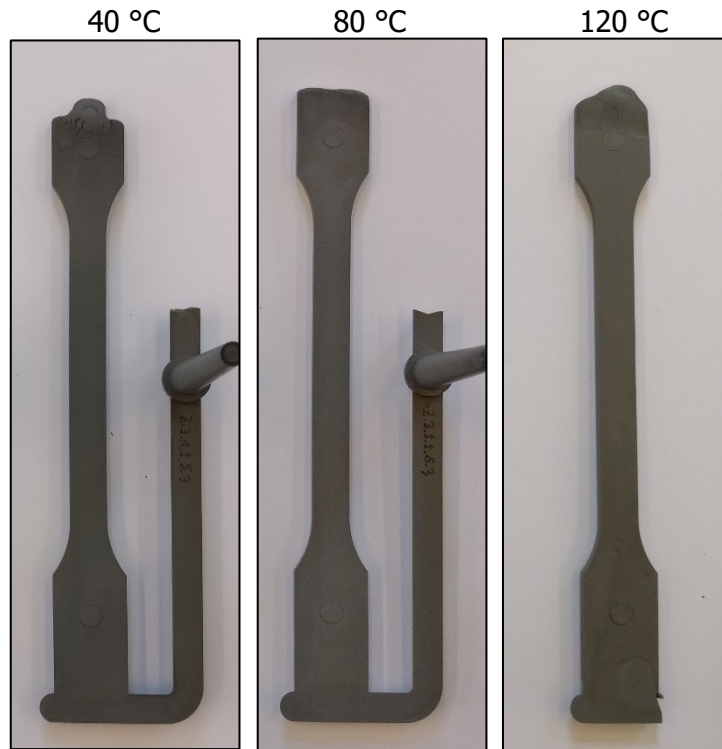


Figure 91: Step 5 of the filling study of PolyMIM 17-4PH tensile specimens at an injection rate of 20 cm<sup>3</sup>/s at different mold temperatures.

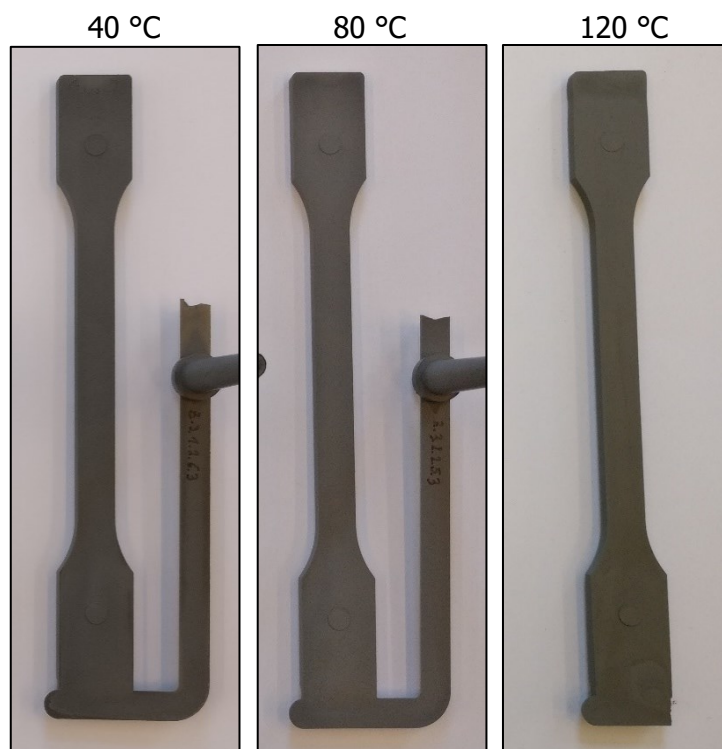


Figure 92: Step 6 of the filling study of PolyMIM 17-4PH tensile specimens at an injection rate of 20 cm<sup>3</sup>/s at different mold temperatures.

**Filling study of PolyMIM 17-4PH – Dog bone specimens,  $\dot{V} = 5 \text{ cm}^3/\text{s}$ :**

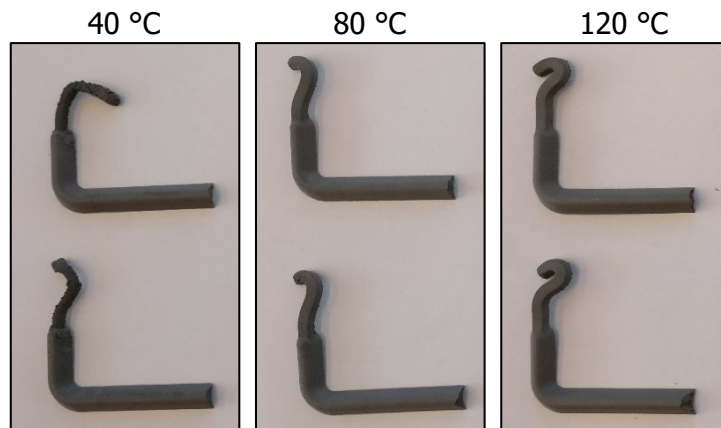


Figure 93: Step 1 of the filling study of PolyMIM 17-4PH dog bone specimens at an injection rate of  $5 \text{ cm}^3/\text{s}$  at different mold temperatures.

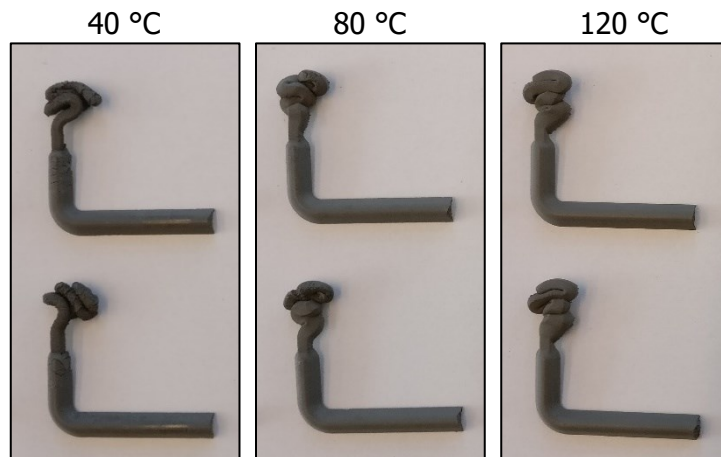


Figure 94: Step 2 of the filling study of PolyMIM 17-4PH dog bone specimens at an injection rate of  $5 \text{ cm}^3/\text{s}$  at different mold temperatures.

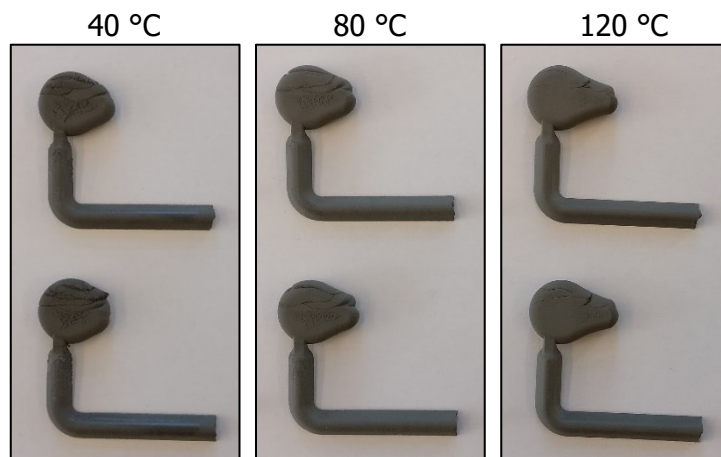


Figure 95: Step 3 of the filling study of PolyMIM 17-4PH dog bone specimens at an injection rate of  $5 \text{ cm}^3/\text{s}$  at different mold temperatures.

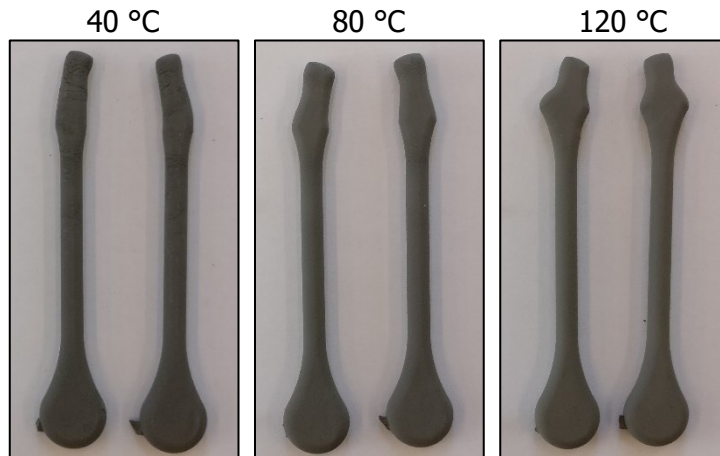


Figure 96: Step 4 of the filling study of PolyMIM 17-4PH dog bone specimens at an injection rate of 5 cm<sup>3</sup>/s at different mold temperatures.

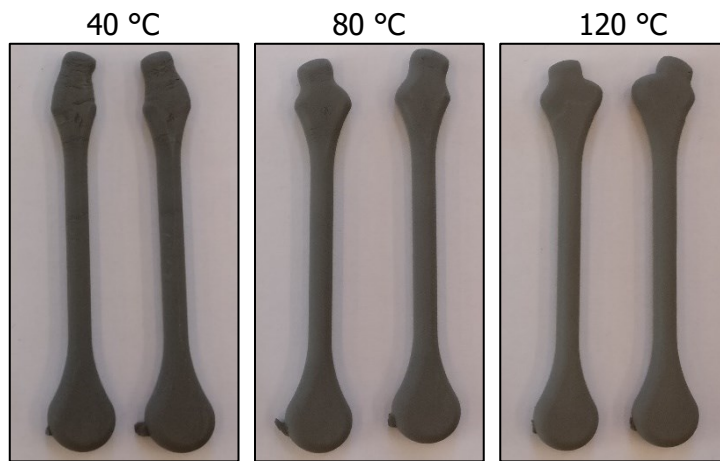


Figure 97: Step 5 of the filling study of PolyMIM 17-4PH dog bone specimens at an injection rate of 5 cm<sup>3</sup>/s at different mold temperatures.

**Filling study of PolyMIM 17-4PH – Dog bone specimens,  $\dot{V} = 20 \text{ cm}^3/\text{s}$ :**

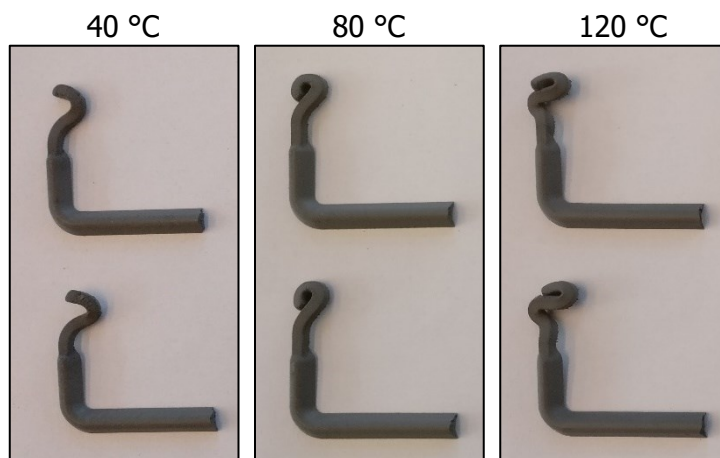


Figure 98: Step 1 of the filling study of PolyMIM 17-4PH dog bone specimens at an injection rate of 20 cm<sup>3</sup>/s at different mold temperatures.

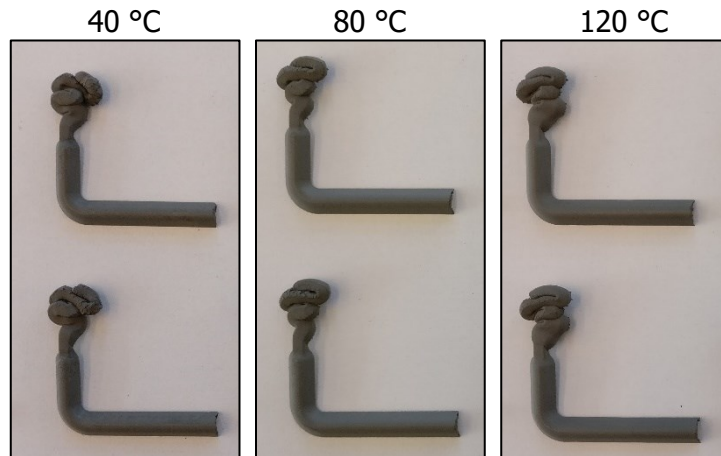


Figure 99: Step 2 of the filling study of PolyMIM 17-4PH dog bone specimens at an injection rate of 20 cm<sup>3</sup>/s at different mold temperatures.

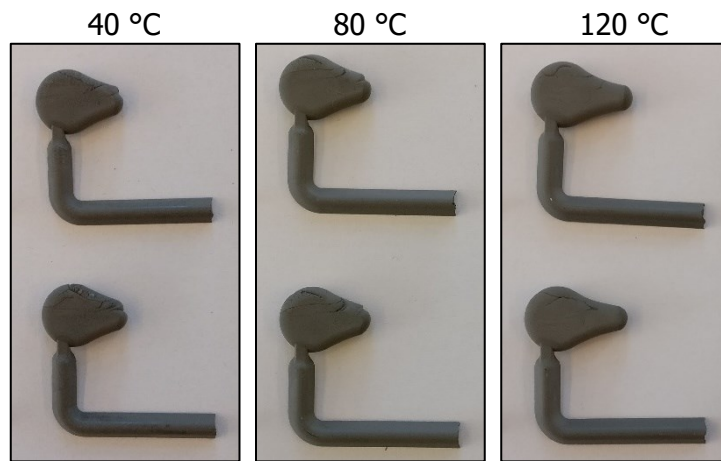


Figure 100: Step 3 of the filling study of PolyMIM 17-4PH dog bone specimens at an injection rate of 20 cm<sup>3</sup>/s at different mold temperatures.

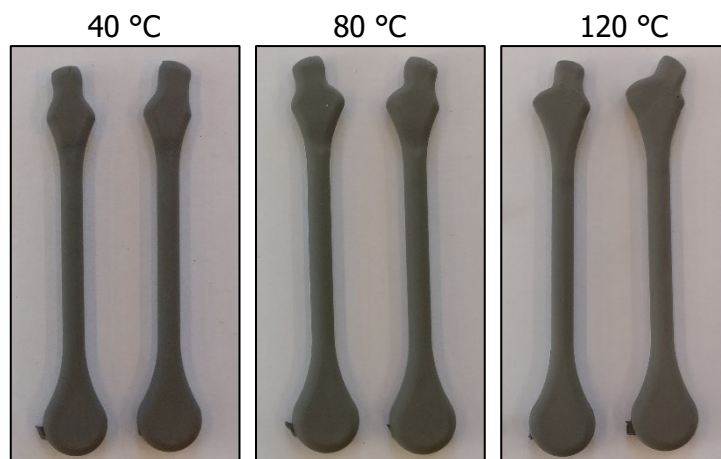


Figure 101: Step 4 of the filling study of PolyMIM 17-4PH dog bone specimens at an injection rate of 20 cm<sup>3</sup>/s at different mold temperatures.

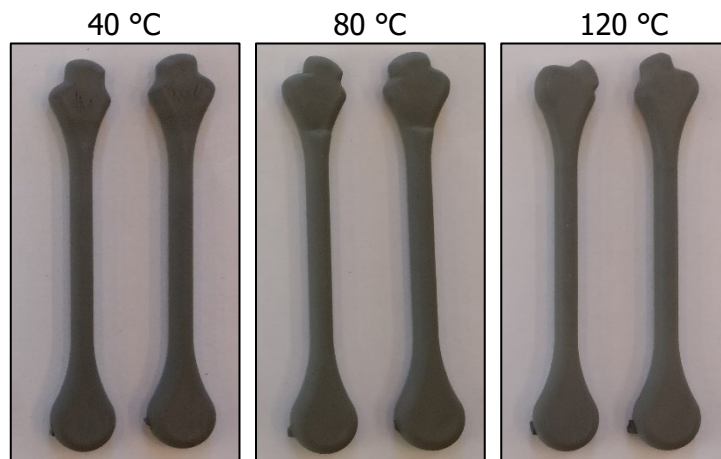


Figure 102: Step 5 of the filling study of PolyMIM 17-4PH dog bone specimens at an injection rate of 20 cm<sup>3</sup>/s at different mold temperatures.